EFFECT OF GROWTH PROCESSES ON CHARACTERISTICS OF SOME TECHNOLOGICALLY IMPORTANT OXIDE AND HALIDE CRYSTALS

By

Shiv Govind Singh

(PHYS01200804010)

Bhabha Atomic Research Centre, Mumbai

A thesis submitted to the

Board of Studies in Physical Sciences

In partial fulfillment of requirements

For the Degree of

DOCTOR OF PHILOSOPHY

of

HOMI BHABHA NATIONAL INSTITUTE

October, 2014

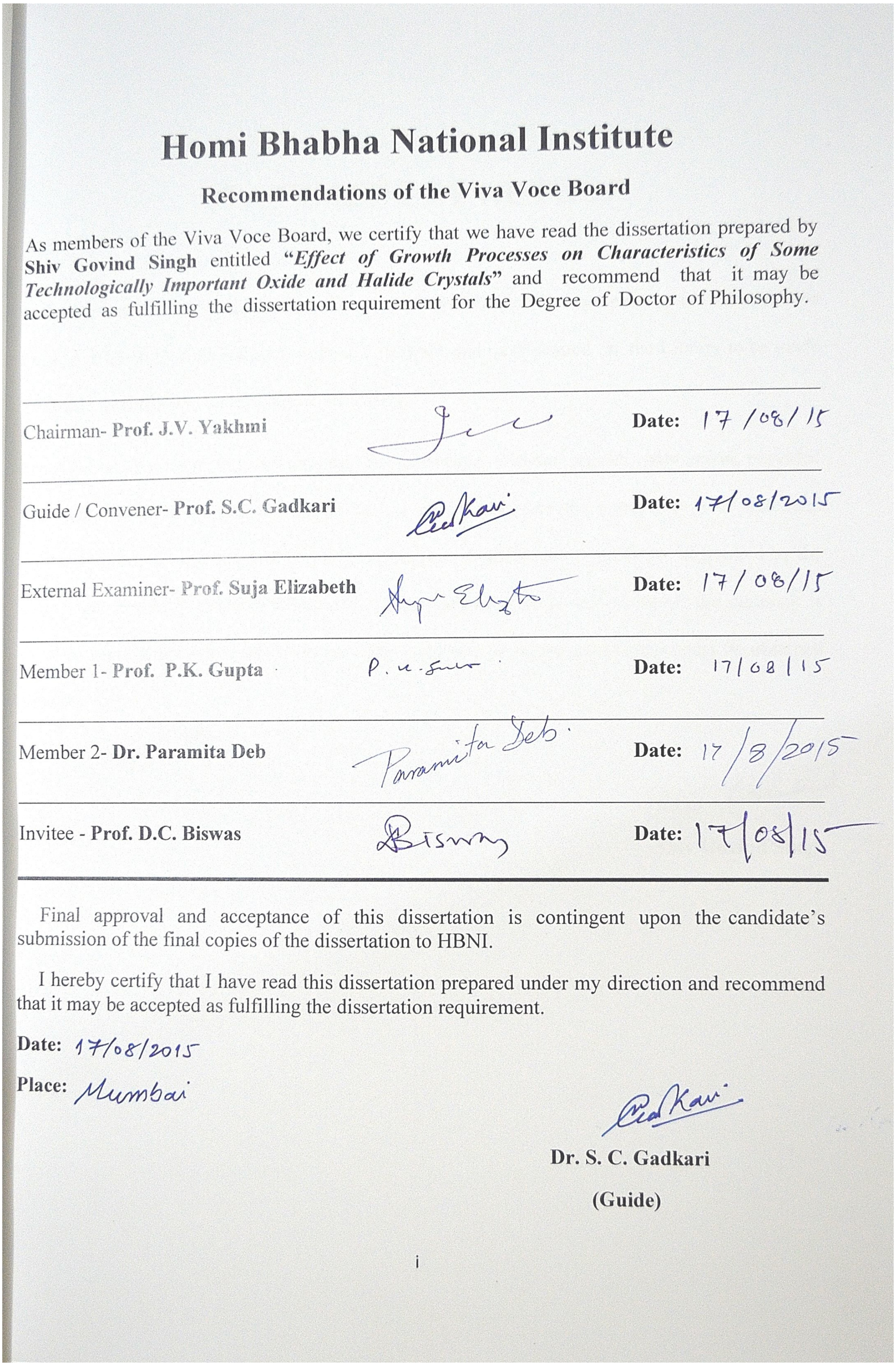

Homi Bhabha National Institute

Recommendations of the Viva Voce Board

As members of the Viva Voce Board, we certify that we have read the dissertation prepared by **Shiv Govind Singh** entitled ***"Effect of Growth Processes on Characteristics of Some Technologically Important Oxide and Halide Crystals"*** and recommend that it may be accepted as fulfilling the dissertation requirement for the Degree of Doctor of Philosophy.

Chairman- **Prof. J.V. Yakhmi** **Date:** 17/08/15

Guide / Convener- **Prof. S.C. Gadkari** Gadkari **Date:** 17/08/2015

External Examiner- **Prof. Suja Elizabeth** Suja Elizabeth **Date:** 17/08/15

Member 1- **Prof. P.K. Gupta** P.K. Gupta **Date:** 17/08/15

Member 2- **Dr. Paramita Deb** Paramita Deb. **Date:** 17/8/2015

Invitee - **Prof. D.C. Biswas** Biswas **Date:** 17/08/15

Final approval and acceptance of this dissertation is contingent upon the candidate's submission of the final copies of the dissertation to HBNI.

I hereby certify that I have read this dissertation prepared under my direction and recommend that it may be accepted as fulfilling the dissertation requirement.

Date: 17/08/2015

Place: Mumbai

Gadkari

Dr. S. C. Gadkari

(Guide)

STATEMENT BY AUTHOR

This dissertation has been submitted in partial fulfillment of requirements for an advanced degree at Homi Bhabha National Institute (HBNI) and is deposited in the Library to be made available to borrowers under rules of the HBNI.

Brief quotations from this dissertation are allowable without special permission, provided that accurate acknowledgement of source is made. Requests for permission for extended quotation from or reproduction of this manuscript in whole or in part may be granted by the Competent Authority of HBNI when in his or her judgment the proposed use of the material is in the interests of scholarship. In all other instances, however, permission must be obtained from the author.

Shiv Govind Singh

DECLARATION

I, hereby declare that the investigation presented in the thesis has been carried out by me. The work is original and has not been submitted earlier as a whole or in part for a degree / diploma at this or any other Institution / University.

Shiv Govind Singh

List of Publications arising from the thesis

Journals

1. "Growth of CsI:Tl Crystals in Carbon Coated Silica Crucibles by Gradient Freeze Technique", **S.G. Singh**, D.G. Desai, A.K. Singh, M. Tyagi, Shashwati Sen, A.K. Sinha, S.C. Gadkari and S.K. Gupta, *J. of Crystal Growth*, **351** (2012) 88–92.

2. "Photoluminescence and photoconductivity studies on $NaBi(WO_4)_2$ single crystals: A promising Cherenkov radiator", Mohit Tyagi, **S.G. Singh**, Shashwati Sen, A.K. Singh, S.C. Gadkari, *J. of Luminescence*, **132** (2011) 41-45.

3. "Fabrication, properties and thermo-luminescent dosimetric application of CaF_2:Mn transparent ceramic", **S.G. Singh**, Shashwati Sen, G.D. Patra, S. Bhattacharya, A.K. Singh, Seema Shinde, S.C. Gadkari, *Nuclear Instruments and Methods in Physics Research B* **287** (2012) 51–55.

4. "Luminescence properties of CaF_2:Mn transparent ceramic", **S. G. Singh,** Shashwati Sen, G. D. Patra, S. C. Gadkari, *J. of Luminescence*, **166** (2015) 222-226.

Conferences

1. "Single crystal growth of Yb doped $NaGd(WO_4)_2$ and structural and spectroscopic studies", S. G. Singh, A. K. Singh, D. G. Desai, B. Tiwari and M. Tyagi, *American Institute of Physics Conf. Proc.* **1591** (2014) 1262-1264.

2. "Scintillation yield uniformity studies on single crystals of Tl doped CsI", D. G. Desai , **S. G. Singh** , A. K. Singh , Shashwati Sen , Seema Shinde and S. C. Gadkari, *American Institute of Physics Conf. Proc.* **1512** (2012) 864-866.

3. "Performance of Indigenously Developed CsI(Tl)-Photodiode Detector for Gamma-ray Spectroscopy", **S.G. Singh**, Arvind Singh, Anita Topkar and S.C. Gadkari, *American Institute of Physics Conf. Proc.* **1349** (2011) 481-482.

4. "Photoluminescence studies on $NaBi(WO_4)_2$ single crystals at low temperatures", M. Tyagi, **S. G. Singh**, A. K. Chauhan, S. C. Gadkari and V. K. Handu, *American Institute of Physics Conf. Proc.* **1349** (2011) 477-478.

5. "Synthesis of optically transparent ceramic of CaF_2 doped with Mn and Ce for thermoluminescent dosimetry", Shashwati Sen, **S. G. Singh**, G. D. Patra, S. Shinde, S. Bhattacharya, S. C. Gadkari, *American Institute of Physics Conf. Proc.* **1447** (2011)11279.

6. “Development of technologically lmportant crystals and devices”, **S.G. Singh**, M. Tyagi, D.G. Desai, A.K. Singh, Babita Tiwari, Shashwati Sen, A.K. Chauhan and S.C. Gadkari, *BARC News Letter*, Issue No. **318** (2011) 16-27.

7. “Influence of after-growth thermal treatments on crystal defects revealed by daylight induced coloration and afterglow in CsI: Tl scintillators”, **S.G. Singh**, M. Tyagi, D.G. Desai, A.K. Chauhan and S.C. Gadkari, *American Institute of Physics Conf. Proc.* **1313** (2010) 337-339.

8. “Synthesis And Luminescence Studies Of Mn doped CaF_2”, **S.G. Singh**, A.K. Singh, Shashwati Sen and S.C. Gadkari, *American Institute of Physics Conf. Proc.* **1313** (2010) 340-342.

9. “Growth, structural and optical properties of $NaGd(WO_4)_2$:Yb crystals”; **S.G. Singh**, M. Tyagi, D.G. Desai, A.K. Singh and S.C. Gadkari; *XIV National Symposium on Crystal Growth*, March 10-12, 2010.

10. “Synthesis of Mn Doped CaF_2 Nanoparticles”, **S.G. Singh**, Shashwati Sen, S.C. Gadkari, *International Symposium on Materials Chemistry*, BARC, (2010).

11. “Photoluminescence and Photoconductivity Studies of $NaBi(WO_4)_2$ Single Crystals: A promising Cherenkov radiator”, M. Tyagi, **S. G. Singh**, A. K. Singh, D. G. Desai, A. K. Chauhan, S. C. Gadkari, *Proceedings of the DAE Symposium on Nuclear Physics, BITS, Pilani*, (2010).

12. “Growth of detector-grade CsI:Tl scintillator crystals by gradient freeze technique”, D.G. Desai, **S.G. Singh**, A.K. Singh, Shashwati Sen, M. Tyagi, A.K Chauhan and S.C. Gadkari, *Proceedings of the DAE Symposium on Nuclear Physics*, BITS, Pilani, (2010).

13. “Growth of detector-grade CsI(Tl) crystals in graphite crucibles’; D.G. Desai, **S.G. Singh**, M. Tyagi, S.C. Gadkari; *Proceedings of the National Symposium on Growth of Device-Grade Single Crystals*-2009,79-80.

DEDICATIONS

This thesis is dedicated to my family and friends.

ACKNOWLEDGEMENTS

First and foremost, I would like to express my deep and sincere gratitude to my thesis supervisor, Dr. S.C. Gadkari for his invaluable guidance, constant encouragement, inspiration, keen interest and good wishes. His wide knowledge and his logical way of thinking on critical scientific problems have been of great value for me. I am also grateful to him for being patient while critically reviewing this thesis.

This thesis would not have been possible without the guidance, help, support, critical analysis and valuable suggestions from my colleagues Dr. S. Sen, Shri. D.G. Desai, Dr. Babita Tiwari, Dr. Mohit tyagi, Shri. A.K. Singh. I am extremely grateful for their support. I would like to extend my sincere thanks Shri. Giridhari Patra, Ms. Seema Shinde, Shri. K. Apparao, Smt Chaya More for their valuable help in carrying out various experiment included in this thesis. I would also like to thank Dr. Anita Topkar, Dr. Jitendra Bahadur, Dr. Narendra Rawat, Dr. Shobit Bhatacharya, Shri Arvind Singh for their valuable supports in carrying out various experiments during the course of this work. It gives me immense pleasure to thank the members of the doctoral committee Prof. J.V. Yakhmi (Chairman), Prof. P. K. Gupta (Member), Dr. Paramita Deb (Member) and Prof. D.C. Biswas (Invitee) for their critical review and suggestions during the progress reviews.

Finally, I owe my heartfelt gratitude to my family who have always encouraged me to follow my heart and inspired my inquisitive mind throughout my childhood and study career. Above all, I would like to thank my wife for her personal support and great patience at all times. I express my sincere thanks to all my friends for their numerous help, support and enjoyable company for making the life pleasant.

CONTENTS

SYNOPSIS

Single crystals have since long created a nice niche among advancement of technology that spans from the electronics and related development to generation of high power tuneable solid state laser and the radiation detection [1-6]. There have been continuous efforts in developing single crystals of new materials with better quality compared to existing one, to improve the quality of single crystals of the existing materials, making their growth easy by improving the growth conditions, or modifying the existing growth techniques for a better yield. In some cases where it is difficult or impossible to grow single crystals with desired properties like homogeneity in dopant concentration, researchers are trying to find a replacement of single crystals in the form of optically transparent ceramics (OTC) that show, in some cases, better properties than the single crystals for specific applications.

The research work of my thesis entitled “Effect of Growth Processes on Characteristics of Some Technologically Important Oxide and Halide Crystals” dwells on the growth of single crystals of a few materials that find applications as scintillator detectors and radiation dosimeters. The effect of growth parameters on their characteristics has been investigated mainly to improve their properties for the intended applications.

A large number of different scintillation crystals exist that are used for the detection and spectroscopy of wide assortment of radiations. A good scintillator should posses certain properties like high density and high Z-effective (stopping power for ionizing radiation), large range of linearity in response (Photon/MeV), transparency to its own emission, faster decay (high rate of pulse counting), suitable emission wavelength to match the photo-detector read out, etc. [7]. Similarly, the requisite properties for a good thermal dosimeter material (another kind of radiation detector) are: single glow curve (single type of trap centres) in the temperature range of 150-250°C, high sensitivity, repeatability, good light output, homogeneity in the trap centre distribution, easy preparation, inert to ambient, etc. However, no material simultaneously meets all these criteria, and the choice of a particular scintillator/dosimeter is therefore always a compromise among these and other factors for a given application. Most of the present scintillators and phosphors for dosimeters can be broadly classified in two categories consisting of halides and oxides compounds. The growth parameters and preparation procedures greatly affect, in terms of defect formation and dopant distribution, the scintillation process and other properties of the materials like radiation hardness, optical properties etc., in a favourable or adverse manner depending on the nature of defects and luminescence centre.

In the present research work I intended to study the effect of preparation procedure and growth parameters on the properties of a few oxide and halide materials including CsI:Tl and $NaBi(WO_4)_2$ and $NaGd(WO_4)_2$ based scintillator and Mn doped CaF_2 as a material for the thermally stimulated luminescent dosimeter. The aim of the study is to make single crystal growth procedure easy and simple and second, to develop a better substitute for Mn doped CaF_2 single crystals for applications in radiation dosimetry.

In the following sections, the research work carried out on these materials and plan of presentation of results in the thesis have been briefly outlined.

Chapter- 1: Introduction

The first chapter of the thesis deals with a brief introduction to single crystals and their applications in various fields with an emphasis on their use as scintillators and phosphor materials in radiation detection and measurement. The scintillation process has been described in a general form and few important steps involved in the process along with some theoretical aspect have been described. The properties of an ideal scintillator are listed with their importance to the intended application has been explained. A brief history of inorganic scintillators along with their properties and preparation methods has also been given. A brief introduction to materials that are studied in the present work i.e. CsI, $NaBi(WO_4)_2$, $NaGd(WO_4)_2$ and CaF_2 along with their brief history is given.

Chapter-2: Experimental techniques

Among the three types of materials considered in the thesis, CsI, $NaBi(WO_4)_2$ and $NaGd(WO_4)_2$ are prepared in the form of single crystals. The crystals of CsI have been grown by a modified Bridgman technique while NRW single crystals have been grown using the Czochralski technique. The third material, Mn doped CaF_2, is developed in the form of optically transparent ceramic (OTC).

In this Chapter, techniques to grow single crystals have been described in general and Bridgman and Czochralski techniques in particular. Other experimental techniques like X-ray diffraction, Laue back reflection, spectroscopy, gamma-ray spectroscopy, etc employed to characterize the starting materials and grown crystals during the present research are described. In addition, results of theoretical electronic band structure calculations for CsI, CaF_2, $NaBi(WO_4)_2$ and $NaGd(WO_4)_2$ are also briefly given in Chapter-2.

Chapter-3: Growth of single crystal of Tl doped CsI by a modified Bridgman crystal growth technique

In this chapter two different approaches that yielded, with considerable ease, good quality device grade single crystals of Tl doped CsI have been described.

I. Growth of CsI:Tl crystals in carbon coated silica crucibles:

In this part, the growth of single crystal of Tl doped CsI in carbon coated fused silica crucibles by a gradient freeze technique has been described. Effects of the axial temperature gradient inside the melt, cooling rate and post-growth annealing on the crystal growth and luminescence properties have been studied and discussed. By analysing the results of a systematic study carried out on the effects of growth process on radiation hardness, day-light coloration and related afterglow of CsI:Tl, optimum conditions for the growth of crystals have been determined. The grown crystals exhibited good radiation hardness and excellent scintillation properties. Gamma-ray detectors were fabricated and characterized to study the effect of growth conditions on the scintillation properties of grown crystals.

II. Growth of CsI:Tl crystals using a modified Bridgman method:

In a different approach a modified Bridgman technique has been designed and developed to grow the CsI single crystal of 50 mm diameter and 60 mm length, in a simple and effective manner. In this part of Chapter-3, design and construction of the modified Bridgeman system employed for the crystal growth of Tl doped CsI are elaborated. A specially designed crucible along with the modified furnace was used to grow single crystal of CsI:Tl of 50 mm diameter and 60 mm length. By employing this technique the thermal and mechanical shocks to the crystal were minimized that reduced the day light coloration and enhanced the radiation hardness of grown crystals.

Scintillation properties of the CsI:Tl have been described in this chapter. Gamma-ray detectors employing CsI:Tl and P-I-N photodiode combination were fabricated and characterized. These detectors showed excellent resolution (<8%) at 662 keV suitable for use in the γ-ray spectroscopy application to identify radio-active nuclides.

Chapter-4: Growth of single crystal of $NaBi(WO_4)_2$ and $NaGd(WO_4)_2$ and study of the effect of oxygen stoiciometry on their scintillation properties

Single crystals of $NaBi(WO_4)_2$ and $NaGd(WO_4)_2$ having high density and radiation hardness are the promising new materials that may find applications as radiation detectors for both luminosity and calorimetric measurements. These materials are intrinsic scintillators wherein WO_4^{2-} group is responsible for the luminescence [8,9]. In this chapter the growth of single crystals of $NaBi(WO_4)_2$ and $NaGd(WO_4)_2$ has been discussed along with the effect of oxygen environment around W on the scintillation and optical properties of these crystals.

(i) $NaBi(WO_4)_2$:

In this section of Chapter-4, the growth of un-doped $NaBi(WO_4)_2$ (NBW) crystals using the Czochralski technique has been described and its luminescence and optical properties as a function of oxygen defects have been analysed. Optical transmission and reflection spectra of as-grown, oxygen annealed and vacuum annealed samples were recorded over the wavelength range from 200 nm to 800 nm. Photo-luminescence (PL) studies were performed over a wavelength range from 300 nm to 800 nm and in a temperature range of 77–300 K. The spectral dependence of photoconductivity was measured at an applied field of 500 V/cm on the same samples.

Photo-luminescence spectra of as-grown crystals consist of emission band at 495 nm and two excitation bands at 322 nm with a shoulder at 280 nm. A large stoke shift of 10,854 cm^{-1} for the emission band was found to be similar to other molybdate and tungstate crystals [10]. The effect of annealing on the luminescence process has been studied and discussed. The annealing induced changes in the energy structure of regular WO_4 complex has been analyzed using the reflectivity and PL spectra and photoconductivity measurements carried out on the as-grown and annealed samples. The temperature dependence of emission was also studied. The thermal activation energy for the quenching was calculated from a Mott–Seitz dependence of photoluminescence and found to be consistent with the PL quenching. Thermal quenching profile was also found to be changed for samples annealed in different ambient.

The electronic band structure of NBW was calculated and analysed. The presence of Bi states in valance band (VB) and conduction band (CB) suggest that the excitons may be created at Bi ions and then trapped at the $(WO_4)^{2-}$ complex. The role of these excitons and localization of charge carriers were understood by comparing the spectral dependence of excitation, photoconductivity (PC), transmission and reflectivity of the as-grown NBW crystal.

(ii) $NaGd(WO_4)_2$:

In this part of Chapter-4 the growth of un-doped and Yb^{3+} doped $NaGd(WO_4)_2$ [NGW] single crystals by the Czochralski technique under various ambient (pure Ar and air) has been described and the optical properties of the grown crystal as a function of growth ambient were studied.

The crystals grown in air ambient were slightly greenish in appearance due to oxygen related defects. The crystal grown in pure Ar ambient was black in colour, though it was crack-free and diameter was well controlled. This crystal (grown in Ar) when annealed at 800°C in air for 10 h turned transparent without any trace of blackness indicating a very high diffusivity of oxygen in the crystal. All the reflection in the powder X-ray diffraction of the grown crystal were in accordance to the crystal symmetry; space group I41/a (though few authors have reported I-4 non Centro-symmetric structure [11]). The Laue pattern was used to confirm the c-orientation of the crystal and its quality. The UV-VIS-NIR spectroscopy of the crystal revealed that the UV band edge of the crystal grown in argon ambient and annealed in air shifted towards lower wavelengths compared to crystals grown in air ambient. Further, the crystals grown in air show a broad absorption band which affects the crystal quality badly.

The intrinsic emission from the single crystals grown in air and Ar were compared. It was found that the intrinsic emission of the crystal grown in Ar ambient and annealed in air has different temperature dependence than that for the crystal grown in air and annealed. These findings suggest that the oxygen related defects play a significant role in optical and fluorescence properties of the material. Thus it was established that by controlling the oxygen content in the growth ambient one can tune the optical and luminescence properties of NGW crystals.

Chapter-5: Optically transparent ceramic of Mn doped CaF_2; a better material to substitute CaF_2:Mn single crystal for applications as radiation dosimeters

The CaF_2:Mn is an important phosphor material for use as the thermo-luminescence (TL) dosimeter. The difficulty in growing doped single crystals of this material arises from high vapour pressure and different crystal structure of MnF_2 that prohibit its incorporation in the CaF_2 crystal lattice during the growth under vacuum conditions and leads to variations in the Mn concentration throughout the crystal. The difficulty in doping single crystals with Mn can be surmounted by preparing optically transparent ceramics (OTC) of this compound. In this Chapter the synthesis and characterization of CaF_2 transparent ceramics doped with Mn (2.5 at.%) are reported.

The OTC of CaF_2:Mn was prepared by hot pressing of nano-powders. The nano-powders were synthesized by a co-precipitation method. The nano powder and prepared OTC were characterized for the phase identification using an X-ray diffractometer. The microstructure of nano-powder and fractured OTC was studied using the SEM. The transmission in the UV–Vis range (200–1100 nm range) was recorded using a spectrophotometer. The photo-luminescence was recorded using a fluorescence spectrometer in the range from 200 nm to 800 nm. Further the valance states of Mn in the OTC were determined using an X-ray photo-electron spectrometer (XPS) and the concentration was determined using a secondary ion mass spectrometer (SIMS). The dosimetric properties were investigated by irradiating the samples with a ^{60}Co gamma source. Thermally stimulated luminescence (TSL) glow curves were recorded for different doses using an indigenously developed thermo-luminescent dosimetry set-up.

The excitation and emission spectra of the Mn doped CaF_2 OTC show the presence of excitation levels corresponding to $^6A_1g(6S)$ – $^4T_2g(4G)$ transitions of Mn^{2+} [14]. The glow-curve from the OTC (10 mg) recorded after a gamma dose of 100 mGy shows a single glow-peak at 260°C. The minimum dose that could be measured was about 3 mGy. The wavelength of the emission spectrum recorded during photoluminescence and TSL was found to be the same (495 nm). This indicates the observed excitation bands in both the cases are due to internal transitions of Mn^{2+}. This fact indicates a possible formation of hole-traps. The dose linearity of the OTC was measured by irradiating the OTC to different doses and measuring the area under the glow-peak. The sample is found to be linear up to the highest dose of over 100 mGy used in the present work.

Chapter-6: Summary and Conclusions

The findings of the research work have been summarized in Chapter-6 of the thesis. Three types of materials were taken for the study; two in the form of single crystal and third in the form of OTC. It has been shown that the growth procedure significantly affects the properties of crystals mainly due to the formation of various types of defects during the material preparation and crystal growth.

A modified Bridgman technique has been developed for the growth of the CsI:Tl crystal and the optimum growth parameters for the best scintillation properties were determined. The effect of oxygen stoichiometry on the luminescence and optical properties of double tungstates were studied and it was established that the luminescence properties of the material can be tailored by appropriately choosing the oxygen environment during the growth or post-growth thermal treatment of crystals.

An alternative of CaF_2:Mn single crystal in the form of optically transparent ceramic has been developed employing hot pressing of nano-crystalline CaF_2:Mn synthesized using a wet chemical processing method. The problem of inhomogeneous distribution of the dopant (Mn) in CaF_2 matrix was solved and it was shown that the CaF_2:Mn (OTC) would be a better material than the conventionally used opaque pellets in TL dosimetry applications.

References:

1. Mitsuru Ishii, Masaaki Kobayashi, Prog. Crystal Growth and Charact. **23** (1992) 245-311.
2. *C W E van Eijk,* Phys. Med. Biol., **47** (2002) R85–R106.
3. Hans J. Scheel, J. Crystal Growth, **211** (2000) 1-12.
4. “Modern Aspects of Bulk Crystal and Thin Film Preparation; ISBN 978-953-307-610-2”, Edited by Dr. Nikolai Kolesnikov, In Tech.
5. Guojian Wanga, YongchenSun , GangYang, Wenchang Xiang , YutongGuan, Dongming Mei , Christina Keller, Yuen-DatChan, J. Crystal Growth, **352** (2012) 27–30.
6. Martin Nikl, Meas. Sci. Technol., **17** (2006) R37–R54.

7. “Radiation detection and measurement; ISBN:978-81-265-2260-6 ”, G. F. Knoll, John Wiely & Sons.
8. Glorieux Benoît, Jubera Véronique, Apheceixborde Arnaud, Garcia Alain, Solid State Sciences, **13**(2) (2011) 460-467.
9. A.B. Campos, A.Z. Simoes, E. Longo, J.A. Varela, V.M. Longo, A.T. Figuerido, F.S. De Vicente, A.C. Hernandes, Appl. Phys. Lett., **91** (2007) 051923-051926.
10. P. Lecoq, I. Dafinei, E. Auffray, M. Schneegans, M.V. Korzhik, O.V. Missevitch, V.B. Pavlenko, A.A. Fedorov, A.N. Annenkov, V.L. Kostylev, V.D. Ligun, Nucl. Instr. Meth. Phys. Res. A, **365** (1995) 291-298.
11. C. Cascales, M. D. Serrano, F. Esteban-Betegón, C. Zaldo, R. Peters, K. Petermann, G. Huber, L. Ackermann, D. Rytz, C. Dupré, M. Rico, J. Liu, U. Griebner, and V. Petrov , Phys. Rev. B, **74** (2006)174114-174129.
12. V. Emir Kafadar, A. Necmeddin Yazici, R. Güler Yildirim, Nucl. Instr. Meth. B, **267** (2009) 3337–3346.
13. A.K. Bakshi, B. Dhabekar, N.S. Rawat, S.G. Singh, V.J. Joshi, V. Kumar, Nucl. Instr. Meth. B, **267** (2009) 548–553.
14. S.W.S. McKeever, B. Jassemenejad, J.F. Landreth, J. Appl. Phys., **60** (1986) 1124-1130.

LIST OF FIGURES

LIST OF TABLES

CHAPTER 1

INTRODUCTION

Single crystals have since long created a nice niche among advancement of technology that spans from the electronics and related development to generation of high power tuneable solid state laser and the radiation detection [1-6]. There have been continuous efforts in developing single crystals of new materials with better quality compared to existing one, to improve the quality of single crystals of the existing materials, making their growth easy by improving the growth conditions, or modifying the existing growth techniques for a better yield. In some cases where it is difficult or impossible to grow single crystals with desired properties like homogeneity in dopant concentration, researchers are trying to find a replacement of single crystals in the form of optically transparent ceramics (OTC) that show, in some cases, better properties than the single crystals for specific applications.

The research work of the present thesis entitled “Effect of Growth Processes on Characteristics of Some Technologically Important Oxide and Halide Crystals” dwells on the growth of single crystals of a few materials that find applications as scintillator detectors and radiation dosimeters. The effect of growth parameters on their characteristics has been investigated mainly to improve their properties for the intended applications.

A large number of different scintillation crystals exist that are used for the detection and spectroscopy of wide assortment of radiations. A good scintillator should posses certain properties like high density and high Z-effective (stopping power for ionizing radiation), large range of linearity in response (Photon/MeV), transparency to its own emission, faster decay (high rate of pulse counting), suitable emission wavelength to match the photo-detector read out, etc. [7]. Similarly, the requisite properties for a good thermal dosimeter material (another kind of radiation detector) are: single glow curve (single type of trap centres) in the temperature range of 150-250°C, high sensitivity, repeatability, good light output, homogeneity in the trap centre distribution, easy preparation, inert to ambient, etc. However, no material simultaneously meets all these criteria, and the choice of a particular scintillator/dosimeter is therefore always a compromise among these and other factors for a given application. Most of the present scintillators and phosphors for dosimeters can be broadly classified in two categories consisting of halides and oxides compounds. The growth parameters and preparation procedures greatly affect, in terms of defect formation and dopant distribution, the scintillation process and other properties of the materials like radiation hardness, optical properties etc., in a favourable or adverse manner depending on the nature of defects and luminescence centre.

In the present research work the effect of preparation procedure and growth parameters on the properties of a few oxide and halide materials has been investigated. These materials include CsI:Tl and $NaBi(WO_4)_2$ and $NaGd(WO_4)_2$ based scintillator crystals and Mn doped CaF_2 as a material for the thermally stimulated luminescent dosimeter. The aim of the study is to make single crystal growth procedure easy and simple and second, to develop a better substitute for Mn doped CaF_2 single crystals for applications in radiation dosimetry.

The first chapter deals with a brief introduction to single crystals and their applications in various fields with an emphasis on their use as scintillators and phosphor materials in radiation detection and measurement. The scintillation process has been described in a general form and few important steps involved in the process along with some theoretical aspect have been described. The properties of an ideal scintillator are listed with their importance to the intended application has been explained. A brief history of inorganic scintillators along with their properties and preparation methods has also been given. A brief introduction to materials investigated in the present work, namely, CsI, $NaBi(WO_4)_2$, $NaGd(WO_4)_2$ and CaF_2 along with their brief history is given. The motivation behind the work of the thesis has also been described in this chapter.

1.1 Material science and technology

Materials science and technology are closely related to each other. Materials technology is a comprehensive discipline that begins with the production of goods from raw materials to processing of materials into the shapes and forms needed for specific applications. Materials technology is a constantly evolving discipline, and new materials and processes with additional benefits over their predecessors lead to new applications. For example, the technology of poly-crystalline silicon ingots has clear advantage over mono-crystalline silicon in terms of cost with small loss of efficiency. Materials Science is a multidisciplinary field that connects material properties to the material's chemical composition, micro-structure and crystal structure and is closely related to materials technology.

In modern age technologically important materials are used in the different forms like single crystals, nano-materials, alloys, glass etc. Among these forms of materials, single crystals or like materials are must in several applications like semiconductor industries, nuclear radiation detection, medical imaging, solid state lasers etc. Though the materials studied in this thesis are mostly used or can be used in nuclear industry, most of them are multifunctional and can be used in various other applications like solid state lasers, beam splitter, optical window etc. In this thesis, these materials are taken, for study, in two forms (I) Single crystals and (II) Optically transparent ceramic (OTC); keeping in mind their application and thus choosing the most suitable form.

1.2 Single crystals and their applications

Materials having atomic arrays that are periodic in three dimensions, with repeated distances are called crystalline materials. A single crystal or mono-crystalline solid is a material in which the crystal lattice of the entire sample is continuous, unbroken with no grain boundaries. The difference in mono-crystalline, polycrystalline and amorphous material is shown schematically in Fig. 1.1.

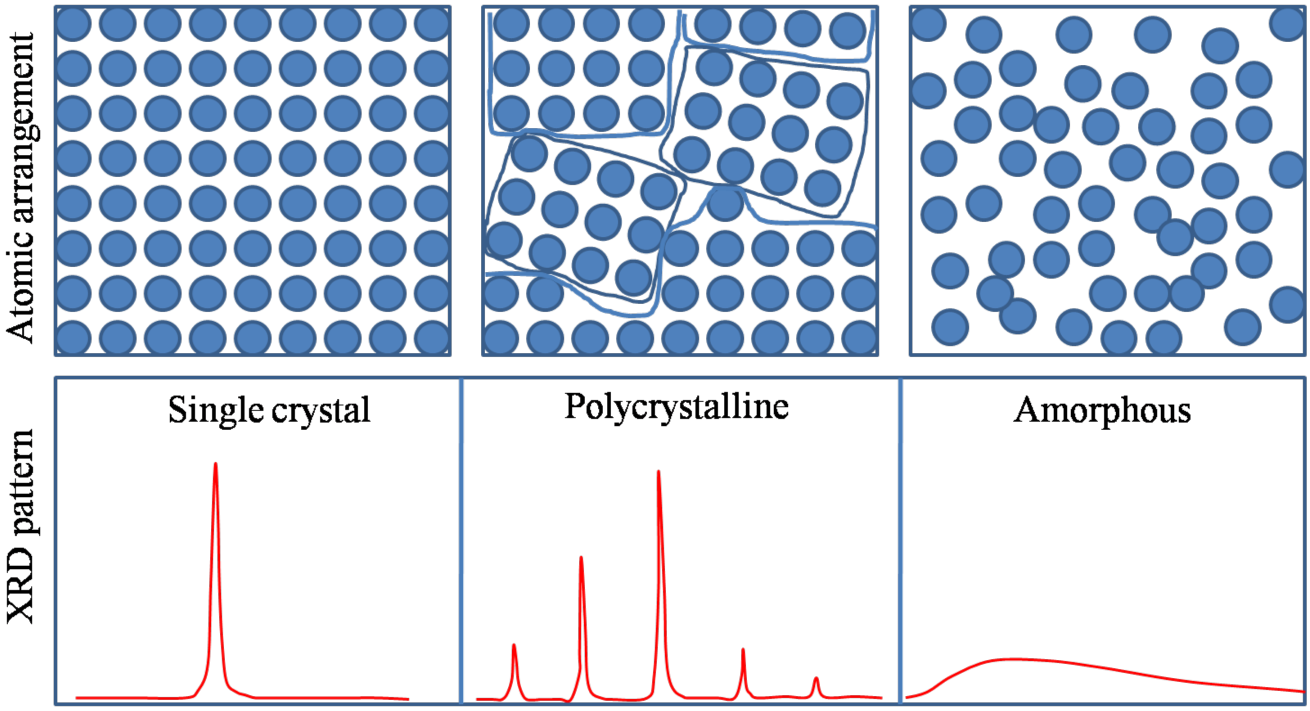

Figure 1.1: Cartoon showing the difference between single crystal, polycrystalline and amorphous forms of the material along with their XRD signatures.

Single crystals are the pillars of modern technology. Many of modern industries like electronic industry, photonic industry, radiation detection/imaging industry etc. depend on single crystals. Though it is more difficult to prepare single crystal than poly-crystalline material, the extra effort is justified because of the outstanding advantages of single crystals. The reason for growing single crystals and its application in many fields is that many physical properties of solids can become obscured or complicated by the effect of grain boundaries like transparency, electrical conductivity etc. The main advantages of the single crystal form of a material are the anisotropy, uniformity of composition and the absence of grain boundaries. The strong influence of single crystals in the present day technology is evident from the continued advancements in the single crystal growth technology [3]. Hence, in order to achieve high quality single crystals at reasonable cost new crystal growth techniques are being developed or the old techniques are refined or modified.

As such applications of single crystals are very vast, but only a few fields are being mentioned here with the emphasis on scintillator and phosphor applications. A relative consumption of single crystals in various applications is given in Fig. 1.2. The field of semiconductor applications is omitted here as in this thesis only the optical crystals are considered.

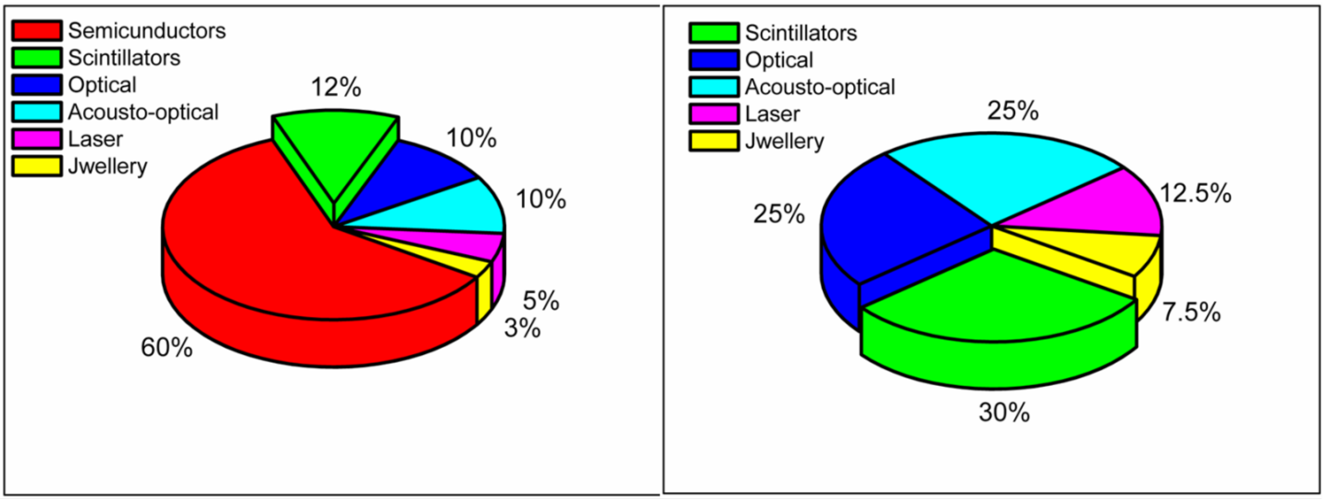

All category crystal application

Optical crystal application

Figure 1.2: Pie-chart depicting applications of single crystals.

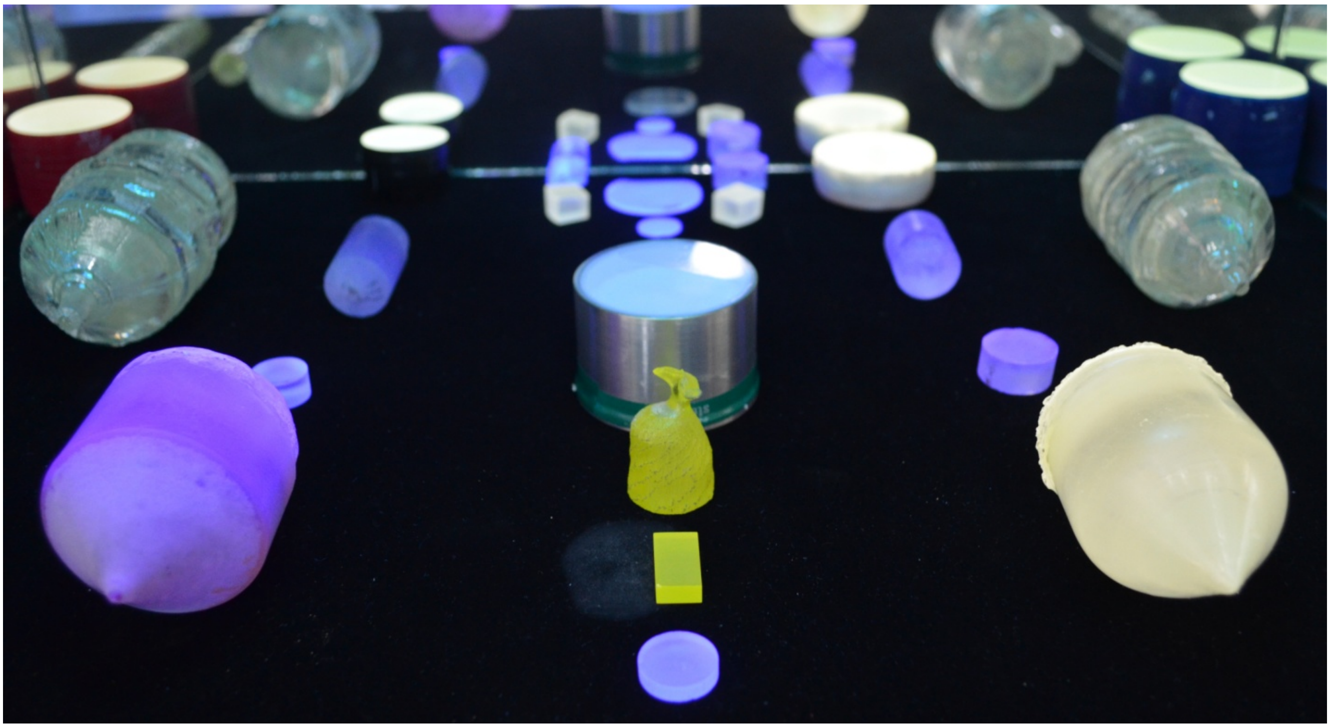

Figure 1.3: Photograph of scintillator crystals under UV illumination.

1.2.1 Scintillator and phosphor

Scintillation is a kind of luminescence processes. Luminescence can be excited in many different ways; by UV-photons, ionizing radiation (X-, γ-, α-, β-rays, charged particles, etc.), electron beam, or electric fields. Photograph of a few scintillator crystals (grown in our laboratory) under UV excitation is shown in Fig. 1.3. The core of the scintillation process is the transformation of energy of ionizing radiation into a variety of optical photons. The delayed scintillation is known as phosphorescence and the materials are called phosphors. The detailed explanation of scintillation process will be given in Chapter-2 of the thesis. The use of a scintillator to detect high energy radiation is century old science. Earliest scintillator that was used for the first time following Roentgen's discovery of X-rays was $CaWO_4$ [8,9], uranyl salts were used by Becquerel in 1896 to discover radioactivity, ZnS was used by Crookes and by Rutherford to study alpha particle scattering. All these scintillators were used as polycrystalline powder sheets to detect the radiation by visual inspection or using a photographic plate [6]. Though the technique led to a number of important discoveries but it does not provide any spectroscopic information about the radiation and was obviously tedious. The period of visual scintillation counting ended in 1944 with the development of photomultiplier tubes (PMT) by Curran and Baker [10, 11]. The PMTs could convert the weak light flashes into measurable electric pulses that could be counted and analyzed electronically in modern-day devices.

Though the PMT was discovered in 1944 its full potential in radiation detection could be utilized only after the discovery of scintillation in Tl doped NaI in 1948 by Robert Hofstadter and availability of NaI:Tl in single crystal form [12]. The NaI:Tl was patented as a first scintillation material in 1950, and John Harshaw from Harshaw Chemical Company (US), initiated interest in growing NaI:Tl crystals by the Stockbarger method. Since then the single crystal growth process has been developed to a state-of-art level. The NaI:Tl is still the most widely used scintillation material and has the highest light yield among the commonly used scintillators. The spectrum of its applications is quite large and ranges from nuclear physics and nuclear medicine to geophysics and environmental measurements. In a burst of exploration during the following decades, variety of new inorganic scintillator were discovered (CsI, CsI:Tl, CsI:Na, $CdWO_4$, CaF_2:Eu, BaF_2 etc) and the growth and production process of scintillator single crystal were refined and perfected. Lithium-containing compounds used to detect neutrons and the first glass scintillators were also developed in the 1950s.

The past two decades have witnessed a great flurry and progress in research and development of scintillator materials, prompted to a major degree by the need for scintillators for precision calorimeters in high-energy physics, high photo-yield scintillators for medical imaging, geophysical exploration, and numerous other scientific and industrial applications [9, 13]. Few excellent materials discovered in past two decades are $LaBr_3$:Ce, LuI_3:Ce, SrI_2:Eu, Lu_2SiO_5:Ce, Gd_2SiO_5:Ce, $Li_6Gd(BO_3)_3$:Ce, $Li_6Yb(BO_3)_3$:Ce, $PbWO_4$ etc. The discovery of $PbWO_4$ by L.L. Nagornaya [14] from the Institute for Scintillation Materials of Ukraine led to a revolution in the collider physics and created a base for the new generation of detection systems in high energy physics, starting from a calorimeter for CMS (LHC, CERN) and finishing with the project PANDA (DSI). Cerium doped Lu_2SiO_5 first discovered by C.L. Melcher [15] that has fast timing characteristic combined with a high light yield revolutionized the positron emission tomography (PET) technology providing unmatched spatially resolved 3D images in medical diagnostics. The Ce activated crystals $LaBr_3$ and $LaCl_3$ with high light yield and excellent proportional response show unprecedented energy resolutions for scintillator detector that was, a few decades back, thought unsurpassable by scintillator detectors.

Though there has been tremendous development in inorganic scintillators, still there are very active researches going on to develop better, bigger and cheaper scintillator crystals. Concurrent with the materials development and use of many new characterization techniques based on synchrotron radiation and laser spectroscopy, have led to a greater understanding of the complexities inherent in exciton and defect formation during and after crystal growth, and the numerous other processes involved in scintillation. These physical processes are now generally well understood and are being used to improve the properties of scintillator material by improving their growth processes [16].

1.2.2 Cherenkov detector

Apart from scintillator, Cherenkov radiation is an electromagnetic radiation emitted as a consequence of passage of charged particle through an insulator at speeds greater than speed of light in that medium [17]. The energy of emitted radiation is proportional to the refractive index of that medium and phase velocity of charged particles passing through it. It is a continuous radiation in UV/visible range without any characteristic spectral peaks. The intensity is very high which is emitted nearly immediately unlike scintillation that occurs with a characteristic time constant. Generally, materials with high density, high refractive index, large band gap, and with no scintillation are better candidates for a Cherenkov detector [18]. Due to the absence of scintillation and high energy threshold for Cherenkov radiation these detectors are best suited for use in Beam end-caps as there is very high background of low-energy charged particles [19,20]. An energetic charged particle can be identified through the measurement of mass-dependent threshold energy of Cherenkov radiation if its momentum is known [21, 22]. Detectors based on Cherenkov radiation are used for particle physics experiments, nuclear reactors, astrophysics experiments, detection of bio-molecules, etc.

1.2.3 Laser host

The first solid state laser built in 1960 by T. Maiman was based on a pink ruby crystal (Al_2O_3:Cr). Since then the there has been tremendous development in the laser host materials and their growth techniques. Single crystals with very high optical quality and minimum defects are essential in the solid state laser applications. Solid-state host materials may be broadly grouped into crystalline solids and glasses. The host must have good optical, mechanical, and thermal properties to produce laser and withstand the severe operating conditions of practical lasers. Desirable properties include hardness, chemical inertness, absence of internal strain and refractive index variations, resistance to radiation-induced color centers, and ease of fabrication. Some of the most useful laser host materials are synthetic garnets: yttrium aluminum garnet,

$Y_3Al_5O_{12}$ (YAG); gadolinium gallium garnet, $Gd_3Ga_5O_{12}$ etc. These garnets have many properties that are desirable in a laser host material [23, 24]. They are stable, hard, optically isotropic, and have good thermal conductivities, which permit laser operation at high power levels. Vanadates (AVO_4: A-Y, Gd, Lu etc) and fluorides ($YLiF_4$:Nd) are other category of good laser host materials [25, 26].

Rare-earth doped double tungstate crystals $NaY(WO_4)_2$, $NaGd(WO_4)_2$, $NaLa(WO_4)_2$, $NaBi(WO_4)_2$, $KY(WO_4)_2$, $KGd(WO_4)_2$ etc. having a disordered structure are of current interest as high gain solid state host materials for lasers due to broad absorption lines of the dopants and low melting temperatures that make their growth easy compared to garnets and vanadates crystals [27, 28].

1.2.4 Others applications

Apart from above mentioned applications that are main theme of the thesis there are several other applications of single crystals.

Acousto-optic devices are based on the effect of propagation of sound waves on the refractive index of a medium, resulting in the formation of refractive index grating are called acousto-optic modulator (AOM). This acousto-optic interaction makes it possible to modulate the optical beam in both temporal and spatial domains by varying the amplitude, phase, frequency and polarization of the acoustic wave. These types of devices are extensively used in mobile communication devices. Single crystals of $LiNbO_3$, $PbMoO_4$, etc. are frequently used in many such applications [29, 30].

Optical window is a piece (mostly circular but sometimes rectangular, optically flat and parallel disc) of a transparent optical material that allows light (for a wavelength range of interest) into an optical instrument isolated from vacuum or other medium. Highly transparent optical windows from deep UV to far IR region are technologically important. The materials to be used in these applications should have large band gap, isotropic and of good mechanical properties. Most popular materials used in optical windows are CaF_2, LiF, BaF_2, ZnS, etc [31].

1.3 Optically transparent ceramics: an introduction

Optically transparent ceramics (OTC) are the highly compacted (to near theoretical density) polycrystalline bulk that show transparency in UV-VIS-NIR region. There are many applications that require optically transparent material like scintillator detector, solid state laser generation, optical window etc. Conventional optical transparent materials mainly include glasses, polymers and alkali hydrides, which have been widely used in industries and daily life. However, these materials have relatively poor mechanical strengths and sometimes insufficient chemical and physical stabilities. With the advancement in technologies in crystal growth, single crystals of some compounds appeared as new transparent materials. Compared to the conventional transparent materials, single crystals of many materials have desired properties and are being used in such application for the last five decades. However, growth of single crystals requires sophisticated facilities and it is time consuming, thus leading to expensive products that are only used in cases where cost is not the deciding factor. Machining of single crystals in various shapes to meet the requirement of specific applications is a difficult task and results in wastage of materials. The variation of dopant in the crystal bulk due to segregation coefficient other than unity is another difficulty faced in the single crystal growth. The non-homogeneity in the dopant concentration may change several properties of a material like luminescence, refractive index, absorption etc. In some applications like thermal dosimetry where batch calibration is required, use of single crystals becomes very difficult. Other problems of single crystals include difficulty to produce in large quantities particularly for brittle materials. Even in case of few materials, that have tendency to decompose or phase change prior to melting, it is not possible to prepare single crystals. In this respect, transparent ceramics become more important. Transparent ceramics have various advantages over single crystals, such as cost-effectiveness, large-scale production, feasibility of shape control and better mechanical properties. Therefore in many applications optically transparent ceramics are proven superior to single crystals [32-33].

The most significant factor to the transparency of a ceramics is the porosity. The surface of a pore (generally filled with air or moisture) is a boundary between phases with sharply different optical characteristics, which therefore intensely reflects and refracts light. Therefore to make a polycrystalline material transparent it is necessary to remove nearly all the pores from the bulk. Pores could be intergrain or intragrain. The elimination of intragrain pores, even if they are submicron in size, is a more difficult and much longer process than the elimination of closed intergrain pores. Another reason of the opacity is the presence of secondary phases at the grain boundaries. Therefore, to fabricate transparent ceramics, it is necessary to use raw materials of high purity and to avoid any possible contamination during processing. Crystal structure and anisotropy in optical properties of a material pose some limitations over the OTC preparation. In ceramics of optically anisotropic crystals, an additional scattering of light arises at the boundaries when the light travels from one grain to another even if there are no pores in between. This is the reason why transparent ceramics generally have a cubic lattice structure, which is isotropic, such as MgO, Y_2O_3, YAG, and $MgAl_2O_3$ (spinel) [34].

1.4 A literature survey

1.4.1 Alkali halides: Tl doped CsI, NaI

The era of inorganic scintillators materials begins with the discovery of NaI:Tl in 1948 by R. Hofstadter. Since then the alkali halides are at the forefront of this field despite discoveries of new and better scintillators. The chief advantages of these materials over the newly discovered $LaBr_3$:Ce and similar crystals are the cost effectiveness and large size production. Followed by the discovery of NaI:Tl, the thallium doped CsI was discovered by same person in 1950 [35]. The CsI:Tl single crystal is a well-known scintillator material, and has been deployed in a variety of applications owing to its moderate density, high light yield and suitably matched emission with photodiodes [36-39]. It shows better scintillation efficiency (if used with a suitable photo-detector), and is less hygroscopic and less brittle than NaI:Tl crystal. This material could not achieve its full potential in the past due to the unavailability of a matching photo-multiplier tube (PMT). However, the possibility to use compact silicon P–I–N photodiodes (PD) that show good efficiency at longer wavelengths and lower operating voltages has renewed the interest in the CsI:Tl crystals. The choice of the CsI:Tl-PD as a detector has been dictated by some considerations in terms of compact size, insensitivity to magnetic fields, reduction of cost and complexity, no requirement of high voltage power supply and mechanical robustness compared to the classical NaI:Tl scintillator with photomultiplier (PMT) read-out. Though, new materials like $LaBr_3$:Ce, $LaCl_3$:Ce etc. show superior scintillation properties, their peak emission in the 350 – 400 nm range makes them unsuitable for use with photo-diodes.

Further, most of these materials are also highly hygroscopic, brittle and expensive. Later Na doped CsI discovered by J. Menfee et al. [40] was proved an excellent scintillator similar to Tl doped NaI [41,42].

Single crystals of CsI can be grown using the Bridgman-stockberger method as well as the Czochralski method [43-46]. The growth of CsI crystals using the Bridgman method does not pose major problems. However, sticking of the grown crystal to crucible walls makes their extraction difficult and stresses are generated during the recovery process [47]. These issues are important and need to be addressed to grow device grade crystals. In addition, the luminescence and scintillation properties, after glow, and radiation hardness etc of CsI:Tl are known to depend upon various stages of crystal preparation, viz.: starting material preparation, Tl concentration, growth technique and post growth annealing treatments [48-50]. Despite considerable efforts for many decades on this material, its poor radiation hardness and long afterglow are still major areas of concern that hinder its application to several other fields. It was found that despite being very old material, literature on the crystal growth of CsI and NaI employing Bridgman technique is less available and few problems like crystal recovery, after growth, annealing steps etc are not explained in details. The research in these fields may improve the crystal quality and make them more useful in radiation detection application.

1.4.2 Double tungstates: $NaBi(WO_4)_2$, $NaGd(WO_4)_2$

A large number of tungstate (AWO_4: where 'A' stands for large size divalent ions like Ca, Pb or Ba) are naturally occurring crystals. Their Scheelite structure is characterized by tetrahedrally coordinated $(WO_4)^{2-}$ group positioned at four corners of a unit cell and the divalent A^{2-} located at bcc is octahedrally coordinated with oxygen ions [51]. The research interest in tungstate materials dates back to early 20th, with the use of $CaWO_4$ as scintillator [8]. In the late 20th century due to the demand from high energy physics crystals of $PbWO_4$ were developed and extensively used as scintillation detectors [52, 53]. Rare-earth doped double tungstates [Re:$NaT(WO_4)_2$ with T being a trivalent ion are also iso-structural to $PbWO_4$ having the same functional group $WO4^{2-}$. Therefore these materials have potential to be used in radiation detection application [54], though these are multifunctional material and are also of current interest in laser generation [55, 56].

Single crystals of $NaT(WO_4)_2$ T: Bi and Gd having high density and radiation hardness are the promising materials that can be used as radiation detector for both luminosity and calorimetric measurements (CERN like conditions) [57]. From the chemical point of view these materials may be regarded as related to $CaWO_4$ Scheelite-type compound with the replacement of Ca by a 1:1 mixture of R and Na. These materials are intrinsic scintillators and WO_4^{2-} group is responsible for the luminescence [58]. The W^{6+} is surrounded by four oxygen atoms in a regular tetrahedral environment. We consider a one-electron charge transfer process from the oxygen 2p orbital to the 4d and 5d of the W^{6+}. For the tungsten compounds, the ground state corresponds to the $^1A_1$ level ($4d/5d^0$ $W6^+$ /$2p^6$ O^{2-} state) and the lowest energy excited state results from the splitting of the $^3T_1$ level ($4d/5d^1$ W^{5+}/$2p^5O^-$ state) [59]. Therefore the absorption band is a charge transfer excitation band. After the relaxation processes through the different vibration levels of the excited state, electrons reach the more stable state of the lowest energy excited state (LEES) from which the system can emit photons. As the emission comes from a level associated to an electron transfer mechanism, it is described as charge transfer emission band. The energy difference between the maximum of the emission and excitation band related to the same two levels is called Stokes Shift. This value gives information about the non-radiative contribution to the relaxation processes.

Tungstates in general are characterized by the presence of two emission bands in the blue and green regions that arise due to electronic transitions within WO_4 groups [60]. The relative intensities of these two emission bands depend on crystal stoichiomtery with regard to both cationic and anionic sub-lattices. Campos et al. [61] and others explained experimentally and theoretically the phenomena responsible for luminescence in $CaMO_4$ (M = W, Mo). The blue-green emission comes from the slightly distorted WO_4^{2+} tetrahedra, while the orange comes from a distortion in the long and medium range orders. Though there have been extensive studies on the effect of growth ambient and annealing on the luminescence and scintillation properties of $PbWO_4$ and other single tungstates [62-64], literature on the growth ambient effect on the luminescence properties of double tungstate is lacking. The present study aims to analyze the intrinsic characteristics of the structure and role of oxygen (during crystal growth as well as annealing in various ambient) in order to know about the role of oxygen in the intrinsic luminescence of the sodium double tungstates.

1.4.3 Fluoride: Doped and undoped CaF_2

The CaF_2 is among the earliest known thermo-luminescence (TL) emitting materials [65-67]. A variety of dosimeters based on Mn or rare earth elements doped CaF_2 have been developed over the years [68-70]. Mineral of CaF_2 is formed in nature in the form of crystalline blocks. Due to its large band gap (~8 eV) it shows a variety of hue and brilliant luminescence on the incorporation of impurity ions. Undoped CaF_2 single crystal is an important optical material with high transmission in a broad wavelength range (165 – 1600 nm) and used as IR windows and other types of optical components such as lenses, prisms, etc. [71]. On the other hand, doped CaF_2 is a multi-functional material that finds applications in laser production (CaF_2:Yb) [72, 73], as radiation detectors (CaF_2:Eu) [74] and as a thermo-luminescence (TL) dosimeter (CaF_2:Dy, CaF_2:Mn, CaF_2:Tm) [75]. The CaF_2:Mn is also a known TL dosimeter called as TL-400 [76]. It has a single TL peak at around 260°C and is linear for a wide range of doses, from 0.5 mGy to few kGy. However, the TL curve depends on the Mn concentration [77] and the maximum glow curve intensity is achieved for a doping of about 2.5 at.% Mn. It is desirable to use transparent CaF_2:Mn samples to obtain better sensitivity, higher light output and repeatability for dosimetric applications. The difficulty in growing doped single crystals of this material arises from the high vapor pressure of MnF_2 that prohibits its incorporation in the CaF_2 crystal lattice during the growth under vacuum conditions. It also leads to variations in the Mn concentration throughout the crystal. Hence, most of the reports on this material are either on polycrystalline powder samples or pellets [77, 78]. The difficulty in the growth of single crystals can be circumvented by using optically transparent ceramics (OTC) of this compound. Recently, fabrication of CaF_2 transparent ceramic doped with Yb, Eu, Er has been reported in literature. Except for CaF_2:Yb applications of these transparent ceramics have not been fully explored yet. In the present thesis the synthesis of CaF_2 transparent ceramics doped with Mn (2.5 at.%) is reported. These ceramics were found to exhibit TL properties superior compared to the CaF_2 single crystal.

1.5 Scope and Aim

The material properties like transmittance, luminescence, radiation hardness etc are highly dependent on the defect centers in the bulk. Various types of defects viz point defects, linear defects (screw and line dislocation), grain boundaries, stacking faults etc. are inherently present in crystals [79]. Color centers, most numerously found defects are basically point defects arising due to lattice vacancies, interstitial atoms (self trapped and impurities) and substitutional impurity ions. They play deterministic role in the optical and emission/scintillation properties of the crystal. These defects act as trap centers resulting in the formation of optical absorption bands in transparent region. These defects may be formed due to elemental impurities or inherently during the material preparation due to growth ambient, stoichiometric variation, thermal and mechanical shock, etc.

The partial oxygen pressure during the material preparation or crystal growth is known to affect the scintillation mechanism to very large extent by creating either oxygen vacancies/interstitial and by changing the oxidation state of dopants. For examples single crystals of Ce doped Lu_2SiO_5 grown in various partial oxygen pressure show different light output due to changes in the Ce oxidation states and emission spectrum [80]. On the other hand, the scintillation decay times of Ce-doped $Gd_3Al_3Ga_2O_{12}$ depend on the oxygen content in the growth atmosphere; crystals grown under a high oxygen concentrations show faster decay time than the one grown under a lower oxygen concentration [81]. Similarly Ce doped $YAlO_3$ is also known to be very sensitive to the growth ambient [82]. In case of halides like NaI and CsI and fluorides, oxygen plays a major role in the defect formation during dehydration and growth processes by creating iodine/fluorine vacancies and F centers. These defects considerably decrease the radiation hardness and increase the afterglow thus adversely affecting the scintillation performance of the material. Oxygen content in the growth atmosphere thus appears to be an important parameter in the optimization of the growth process of scintillation materials that can be used to tailor the performance of the scintillators.

The stoichiometric variation during the growth of the multi-component materials due to selective evaporation or segregation of one of the constituent element or compound is another parameter that affects the crystal quality and properties. For example during the growth of $PbMoO_4$ single crystal the selective evaporation of MoO_3 creates various defects that in turn generate crystal cracking and coloration [83]. On the other hand during the growth of $PbWO_4$, the melt become progressively deficient in PbO that affect the crystal quality. To solve these problems the initial material is taken in an off-stoichiometris composition compensate for the excessive loss of one of the components, for example in the case $PbMoO_4$ and $PbWO_4$, MoO_4 and PbO respectively are taken 1-2% excess in the initial material. In some cases pre-crystallized charge is also used to solve this kind of problem.

The defects are also formed due to the thermal and mechanical stresses generated during the crystal growth. The thermal and mechanical shocks faced by a crystal highly depend on the crystal growth technique. Like in the Czochralski growth technique (RF heating) growing crystal faces large thermal shock as the free crystal surface is continuously in contact with ambient air flow and is subjected to very high temperature gradients. While in a Bridgman furnace the mechanical stresses exerted by crucible walls on the growing crystal during the growth and cooling are high. These shocks generate stresses in the crystal that are one of the reasons of crystal cracking.

The segregation of the dopant during the crystal growth is another issue faced by crystal growers. This creates non-uniformity in the dopant distribution in the crystal that in turn affects the optical and scintillation properties of the crystal. In case of scintillation the light-output response of the scintillator becames position dependent that degrades the resolution of the radiation detector fabricated using these crystals. Further, the refractive index variations play a detrimental role in the laser crystals and make lasing action impossible if the variation is beyond a certain limit.

It is well established that defect density plays a deterministic role in device applicability of a crystal and its control is quite challenging. There are continued efforts to grow single crystals with least defects and maximum uniformity by improving the growth process and developing new growth techniques. The development of processes to grow crystals with tight specifications for light yield, decay time and radiation damage, pose challenging problems to be solved by experts working in different fields of material science. This requires a multidisciplinary approach, with a good coordination of efforts and a well-organized support. To solve the growth problem it is very important to understand the effect of growth process on the defects and the crystal quality. There are many advance techniques to probe the defects experimentally like optical absorption, thermoluminescence or electron spin resonance (ESR) techniques, scintillation characteristics etc. The effect of many defect centers (color centers) on electronic band structure can be simulated by first principles calculations that then can be identified experimentally and the true nature of the defect center may be found. A deeper understanding of color centers could be obtained through band formalism and calculations of electronic band structure and supported by detailed experimental work.

The scope of this thesis is to study the effect of growth processes on some technologically important crystals. Three kind of material ware considered for the study with the major emphasis on their scintillator and phosphor characteristic. The main aim is to develop suitable growth processes (mainly involving the growth techniques, the growth ambient and after growth thermal treatment) to grow crystals with desirable properties. In one case (Mn doped CaF_2) a better substitute for single crystal has been developed.

CHAPTER 2

EXPERIMENTAL TECHNIQUES

In this Chapter, techniques to grow single crystals have been described in general and Bridgman and Czochralski techniques in particular. Other experimental techniques like X-ray diffraction, Laue back reflection, absorption and luminescence spectroscopy, gamma-ray spectroscopy, etc employed to characterize the starting materials and grown crystals during the present research are described. In addition, the theoretical electronic band structure calculations for CsI, CaF_2, $NaBi(WO_4)_2$ and $NaGd(WO_4)_2$ are also briefly described.

2.1 Crystal growth: Fundamental aspect

A material is transformed into the single crystal form by slow and gradual solidification of its fluid form (melt, solution or vapor phase). The process involves the change of phase where molecules of the material undergoing phase change, lose their random character gradually but uniformly and attain a long range order in the form of crystalline solid [84]. Crystal growth is a two step process involving mass transport, either by diffusion or convection from the solution to the crystal face, followed by integration in the lattice of the building units at the active site of crystal surface. Either step may control the overall growth process while several integration mechanisms may play a role, depending on the character of the crystal surface, temperature and the degree of supersaturation of solution.

Theoretical understanding of crystal growth process started with the development of thermodynamics and nucleation theories in the late 19th century (Gibbs, Arrhenius, Van't Hoff) and the increasing understanding of the role of transport phenomena in the 20th century [3,85,86]. There are three basic steps involved in the crystal growth; supersaturation or supercooling of mother solution, controlled nucleation and growth of select-nuclei into a single crystal.

Supersaturation and supercooling: When, at a given temperature a solution contains more solute that it can hold in normal conditions the solution is called supersaturated solution and the phenomena is called supersaturation. The supersaturation provides the driving force for nucleation and further crystallization in case of single crystal growth from solutions. On the other hand, the melt at temperature below its freezing point is called supercooled melt and the process is called supercooling. A controlled supercooling is a must for the growth of a single crystal from the melt.

Nucleation: Gibbs free energy plays the most important role in first order phase transformation and decides the direction and rate of the reaction/transformation. Crystallization is a phase transition through which matter is transformed from a state of high free energy in a solvated state to one of low free energy in the crystal lattice. The nucleation is the first step in the transformation of one phase in to the other. Tiny aggregates of atoms/molecules of solid or liquid phase formed through mutual interaction into a supersaturated liquid or gaseous form are called nuclei and process is known as nucleation. Alone supersaturation/supercooling is not sufficient to initialize the process of crystallization in a system. The formation of crystal nuclei is a complex process and difficult to envisage. Not only have the constituent molecules to coagulate, resisting the tendency to re-dissolve, but they also have to become orientated into a fixed lattice. The number of molecules in a stable crystal nucleus can vary from about ten to several thousand. Generally, nuclei may arise by progressive molecular addition to form a critical cluster. Further molecular additions to the critical cluster would result in nucleation and subsequent growth of the nucleus. Initially, short chains or flat monolayers may be formed that eventually transformed into a 3D-crystalline lattice structure. The construction process, which occurs very rapidly, can only continue in local regions of very high supersaturation, and many of the embryos or `sub-nuclei' fail to achieve maturity; they simply re-dissolve because they are extremely unstable. If however, the nucleus grows beyond a certain critical size, it becomes stable under the average conditions of super-saturation obtained in the bulk of a fluid. As accepted generally, process of nucleation can be divided in two categories: (i) homogeneous and (ii) heterogeneous nucleation.

The formation of stable nuclei in a supersaturated homogeneous solution in melt is called homogeneous nucleation. Though it is very difficult to have a homogeneous nucleation as there may be impurities present in the solution or even containers wall may act or facilitate the nucleation by providing free surface and thus minimizing the free energy. The free-energy changes associated with the process of homogeneous nucleation may be considered as follows.

The difference in the overall free-energy, ΔG, between an atom or molecule of small solid particle of solute (assumed here to be a sphere of radius r) and that of solute in solution is equal to the sum of the surface excess free-energy, ΔG_s (the difference between the free-energy of the particle at surface than that of the particle in the bulk), and the volume excess free-energy, ΔG_v, i.e. the difference in the free-energy between a very large particle ($r = \infty$) and the solute in solution. Here, ΔG_s is a positive quantity, the magnitude of which is proportional to r^2. In a super-saturated solution $\Delta G_v$is a negative quantity proportional to r^3. Thus,

$$\Delta G = \Delta G_s + \Delta G_v = 4\pi r^2 \gamma + \frac{4}{3}\pi r^3 \Delta G_v \tag{2.1}$$

Here γ is the surface free-energy per unit area and ΔG_v is volume free-energy per unit volume. The typical curve of total free-energy is plotted in Fig.2.1. From the curve it is clear that ΔG passes through a maximum,

$$\frac{d\Delta G}{dr} = 4\pi r_c^2\gamma + \frac{4}{3}\pi r_c^3\Delta G_v = 0; \qquad r_c = -\frac{2\gamma}{\Delta G_v} \tag{2.2}$$

Now the rate of nucleation can be given by Arrhenius reaction velocity,

$$J = Aexp(\frac{-\Delta G}{kT}) \tag{2.2a}$$

And from the basic Gibbs-Thomson relationship,

$$kTln\frac{c}{c^*} = \frac{2\gamma v}{r}; \qquad \Delta G_v = \frac{2\gamma}{r} = \frac{kTlnS}{v} \tag{2.3}$$

Here S is the degree of supersaturation. The Eq.2.3 gives the free-energy change per unit volume in solution growth. The same may be applicable for the melt growth by changing the degree of supersaturation by the degree of supercooling. Thus, by controlling the degree of supersaturation or supercooling one can control the rate of nuclei that is most important parameter in the crystal growth.

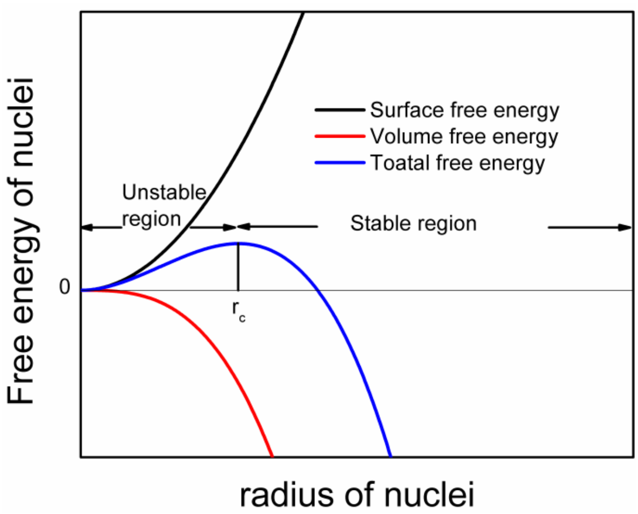

Figure 2.1: Free-energy curve for the surface free-energy, volume free-energy and total free-energy as a function of radius of nuclei.

When the nucleation occurs due to the presence of a nuclei of foreign or of same material (called hetero–nuclei: like introduction of seed crystal in a supercooled melt) in the mother solution or melt it is called heterogeneous nucleation. The presence of foreign nuclei may either increase the rate of nucleation or it may decelerate it depending on its surface free-energy.

Growth of select nuclei: The third step of the single crystal growth is the growth of select nuclei. In a supersaturated or supercooled mother solution or melt more than one nuclei of the radius greater than the critical radius may be formed. These nuclei may have different crystallographic orientation that is not conducive for the crystal growth. To have a single crystal one has to kill all but one nuclei. This is done with the help of a proper temperature profile, specially designed crucibles and slow cooling rate (Homogeneous nucleation: generally occurs in the Bridgman growth technique) or by initiating growth by introducing a seed crystal (Heterogeneous nucleation: in the Czochralski growth technique). Nearly all the single crystal growth techniques are based on these steps, though the methods to achieve these three stages are different in different techniques.

2.2 Crystal growth techniques

Single crystals may be formed by three types of phase transformation; (i) solid-solid (ii) liquid-solid and (iii) gas-solid. While a number of techniques adopting one of these three basic methods of crystal growth can be employed to grow small size crystals, development of device quality single crystal is quite a challenging task. Most of the industrial level crystal growth methods are based on the liquid-solid process to grow high quality device grade crystals. Further division of liquid-solid growth process is listed in Table-2.1. In the pie chart of Fig.2.2 the relative contributions of different growth processes in the overall industrial production of single crystals are depicted. This shows that among all the processes the melt growth accounts for about 80% of single crystal production despite it is used only for selected congruently melting materials [3, 87]. The Verneuil melt growth technique, one of the oldest techniques used for the industrial production of sapphire crystal, is called the father of industrial crystal production [88, 89]. All the other melt growth techniques draw their fundamentals (to control nucleation and then increase the diameter etc) from the Verneuile method like Bridgman method, Czochralski method etc.

The choice of a crystal growth technique to grow single crystals of a particular material is not trivial. There are many parameters that decide which crystal growth technique will be the most suitable to grow single crystals of a particular material. The suitability of a particular technique for a given crystal is guided by material properties like melting behavior, melting temperature, thermal expansion, melt viscosity, thermal conductivities, chemical stabilities of melt/solid, vapor pressure of components at melting temperatures and requirement of size and quality, etc. The material studied in this thesis are grown in the single crystal by using two different, oldest and most widely used melt growth techniques (i) Czochralski and (ii) Bridgamn techniques. In the following section these two techniques are described in details.

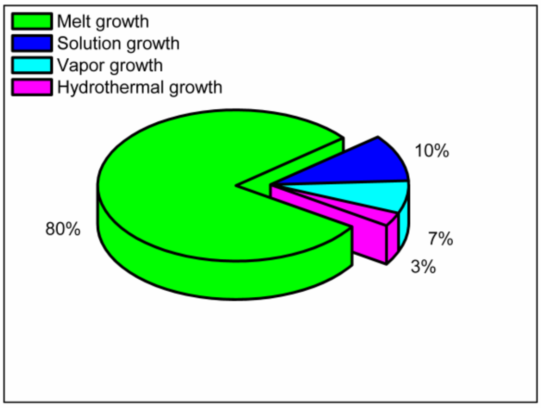

Figure 2.2: Estimated shares of world crystal: methods of growth.

Table.2.1: List of techniques of crystal growth from liquid phase.

Melt growth	Solution growth
Czochralski	Growth from aqueous solution
Kyropolus	Travelling heater method
Bridgman	Solution solute diffusion
Float-zone	Solvent evaporation
Vernuil	Hydrothermal method

2.2.1 Czochralski technique

The Czochralski technique (CZ) was named after Jan Czochralski, a polish chemist, who first developed this technique in 1918 while studying the crystallization velocity of metals [90]. Later this method was applied with unprecedented success in the growth of semiconductor and oxide crystals. Many variations of these techniques like Liquid encapsulated CZ method, high pressure CZ method, etc. were evolved over the time to grow many complex semiconductors and inter-metallic compounds [87,91]. Particular advantage of this technique lies in the wide assortment of parameters that can be controlled during the growth like temperature gradients, growth orientation, the ambient, the forced convection by rotation and applied magnetic field and many others. Further, as it is possible to observe the process of seeding and growth, corrective measures can also be taken in real time. These points make the CZ as the most versatile and preferred technique for the crystal growth of semiconductors and oxide materials at industrial scale. In CZ technique crystals are grown by slow pulling of a seed/wire/ capillary from the free surface of a melt contained in a crucible. A growth station, to contain crucible and minimizes heat losses (by conduction and radiation), is made using appropriate ceramic tubes, felts, and wools. The material to be grown is melted in a crucible by heating it in a suitable furnace (resistive heating, RF heating, Arc heating, etc). A seed is lowered in to the melt, and then pulled (at a typical rate 0.2-5 mm/h) along with rotation (at a typical rate of 5-25 rpm) after achieving a dynamic equilibrium at the solid-melt interface. After the completion of the crystal growth with desired length and diameter, the process is terminated by suitably adjusting pull rate and temperature at the solid-melt interface. The grown crystal is then cooled down to room temperatures at a slow cooling rate suitable for the material. In normal conditions (if there is no stoichiometric deviation due to decomposition and dissimilar evaporation of melt components), the melt temperature is nearly constant during the growth. The shape of the crystal can be determined by controlling the diameter of the growing crystal through the manipulation of the melt temperature and pull rate depending on properties of the material under consideration.

Theoretically, every material that melts congruently and does not undergo any phase transition during cooling, can be grown by this technique but there are some practical restrain that put some limits on the materials which can be grown by this technique [87]. These limits are: suitable crucible material (unreactive, withstand high temperatures, easy in cleaning, easy in fabrication, e.g. Pt, Ir, graphite, quartz etc), a low vapor pressure of melt, high thermal conductivity of the material (to conduct away the heat released from crystallization at the solid-melt interface) etc.

Crystal growth system: The crystal growth system used in this technique is called “CZ crystal puller”. The CZ puller is equipped with an RF heating coil and automatic diameter control as shown in Fig.2.3. It consists of the following components,

1) An RF power supply: to melt the material and maintain high temperature through induction heating of the crucible.
2) A growth station: containing crucible to contain the melt and thermal insulation to achieve desired temperature profiles.
3) The growth chamber: A double walled water cooled cylindrical chamber of adequate dimension, arrangement to hold the growth station, provision for pull-rod insertion, gas inlets and various view ports to monitor the growth.
4) Mechanism for pulling, rotation and crystal weighing, which is used as input for the diameter control algorithm.
5) Electronic/Computer controlled system for maintaining the crystal diameter through adjustment of heater power [92].

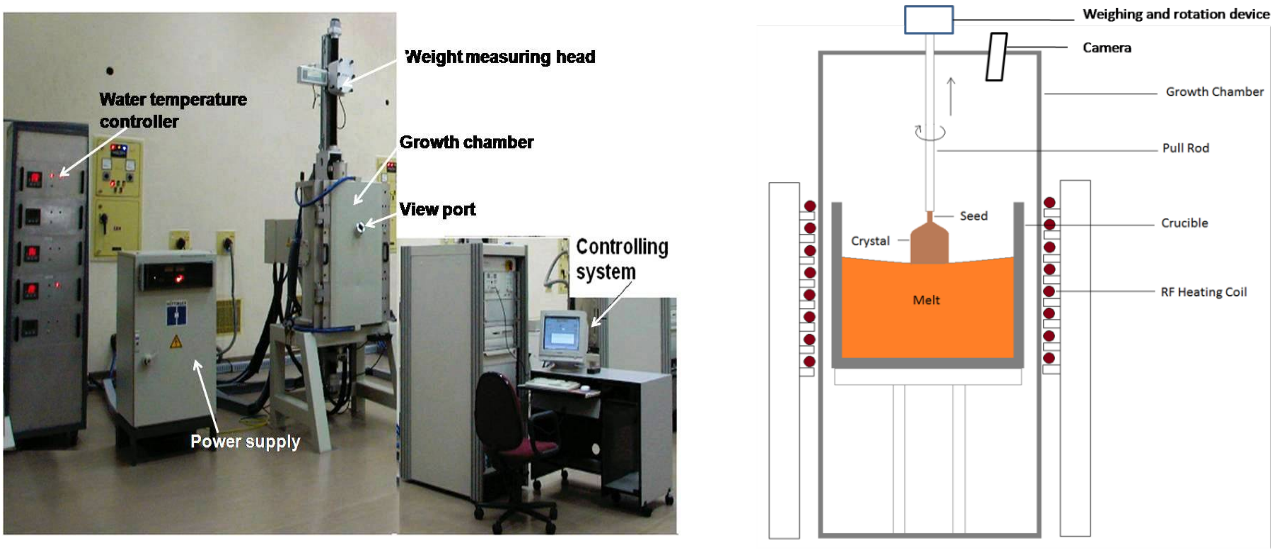

Figure 2.3: Photograph of the Crystal puller system [Cyberstar make Oxypuller] along with schematic of CZ puller.

A photograph of an automatic diameter controlled (ADC) crystal puller system Model: Oxypuller, Cyberstar, France used in the present work is given in the Fig.2.3. This system employed 50 kW and 8-20 kHz induction supply, a weighing head of 6 kg capacity with an accuracy of 1 mg, total crystal translation of 600 mm with positioning accuracy of 0.01 mm. The system controls the diameter through a closed-loop feedback. The ADC software generates the reference growth rate (solidified mass/h) based on the pre decided geometry of the crystal to be grown. The difference between the reference growth rate and actual growth rate (as measured by the weighing device) the system generates an error signal and through a PID control it adjusts the power to keep error signal close to zero.

2.2.2 Bridgman technique

This method is based on the work of Bridgman in 1925 [93]. This is a popular technique to grow single crystals of various halides. In this method temperature gradient moves slowly relative to a crucible (vertically or horizontally) until the melt in the crucible solidifies. The main economic advantage of the method is simple basic apparatus, and little operator attention. Disadvantages arise from the contact between container and melt/solid which can give spurious nucleation, sticking of the crystal ingot inside the crucible and consequently generating thermal and mechanical stresses. Therefore to choose appropriate crucible material and its proper processing and design are important considerations. A typical Bridgman crystal growth system consists of two heating zones controlled independently and separated from each other using a baffle to increase the temperature gradient and minimize temperature fluctuations (Fig.2.4). A crucible containing the material is kept in the upper zone (hot zone) for complete melting then it is slowly lowered (1-5 mm/h) to the lower zone (cold zone) through an optimized temperature gradient until complete solidification. A modified form of Bridgman method and probably simplest method for directional crystallization is the gradient freeze technique. In this method freezing isotherm is moved by slowly reducing the power input to the furnace. The main advantage lies in absence of any movement of either furnace or crucible which eliminates any possibility of vibration or other mechanical problems. Though it is difficult to keep a constant growth rate throughout the crystal growth process due to a relatively small temperature gradient (otherwise temperatures at the top of the furnace will be out of limit), in some cases it is achievable by a segmented cooling program in accordance with the temperature gradient to keep the rate of movement of freezing isotherm constant.

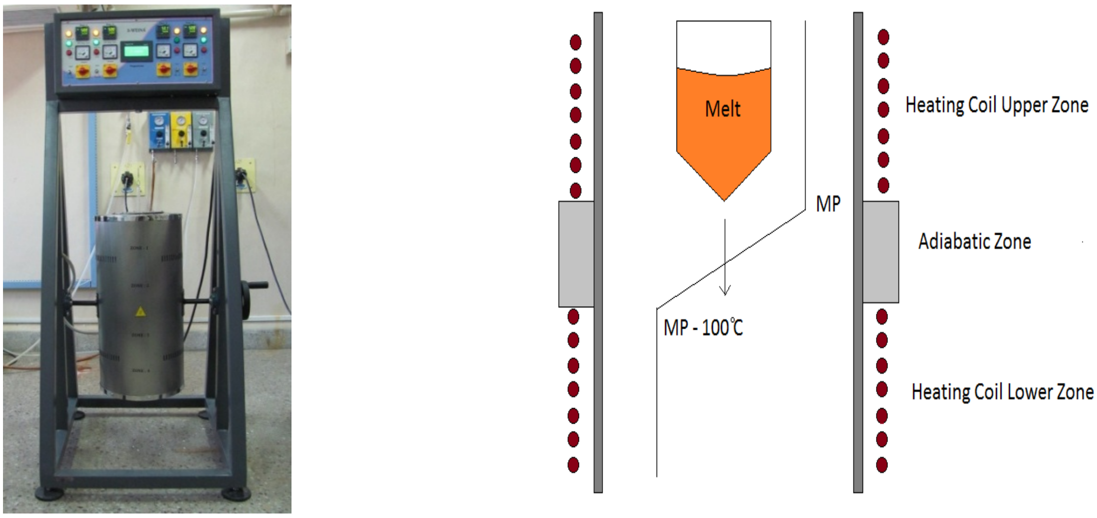

Figure 2.4: Photograph of a Bridgman crystal growth system along with the schematic of the furnace.

2.3 Optically transparent ceramics: Preparation method

The process of transparent ceramics fabrication consists of synthesis of precursor powder, compacting, calcination/sintering and post-treatment (annealing, machining and polishing). The process has its special requirements like high purity of precursor material, specific distribution of particle size, controlled grain growth, amount of additives etc. Further, the sintering techniques play the most important role in the fabrication of transparent ceramics. There are various sintering techniques employed to achieve high degree of compactness. Some of these techniques are hot uniaxial pressure sintering (HP), hot isostatic-pressure sintering (HIP), vacuum sintering, spark plasma sintering (SPS) and microwave sintering. Among these techniques HP sintering is simplest and widely used method to prepare transparent ceramics [94, 95]. It is a high-pressure low-strain-rate powder metallurgy process to form a powder or powder compact at a temperature high enough to induce sintering and creep processes. This is achieved by the simultaneous application of heat and pressure. Unlike the conventional sintering process that usually requires high sintering temperatures the HP process is able to achieve desired densification at relatively low temperatures [96]. Densification at high pressures works through particle rearrangement and plastic flow at the particle contacts. The HP is mainly used to fabricate hard and brittle materials. The sintering mechanism at high pressures is entirely different from that at ambient pressure. High pressure can restrain grain growth and initiate plastic deformation to eliminate pores and/or additional phases that exist in triple junctions of the grains. The application of HP allows for more freedom to optimize the sintering parameters like temperature, pressure, duration. One can use a segmented step wise sintering under various pressures and temperatures [97].

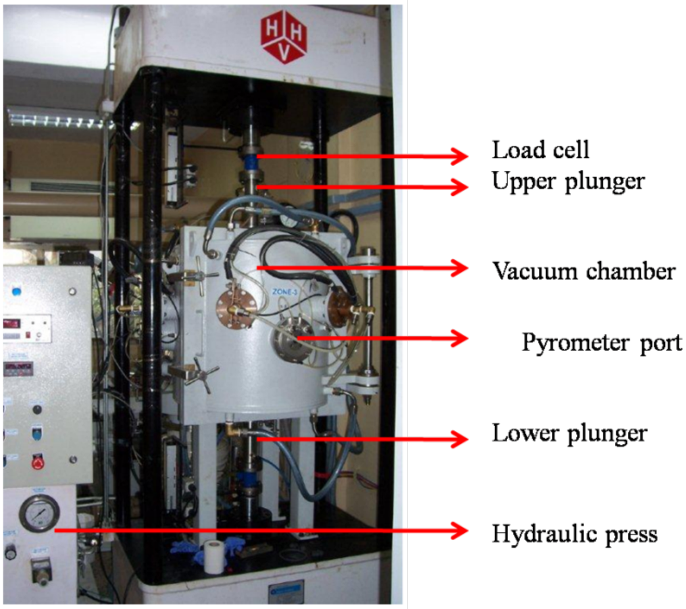

Figure 2.5: Photograph of a vacuum hot press.

In this work HP sintering technique has been employed to obtain optically transparent ceramics of CaF_2. The system consists of a vacuum chamber (base pressure: $1x10^{-6}$ mbar using diffusion pumps) a hydraulic press and two perfectly aligned (vertical) plungers to press the sample in a graphite die. A graphite heater was used to heat the samples. Photograph of the HP used in the experiments is shown in Fig.2.5.

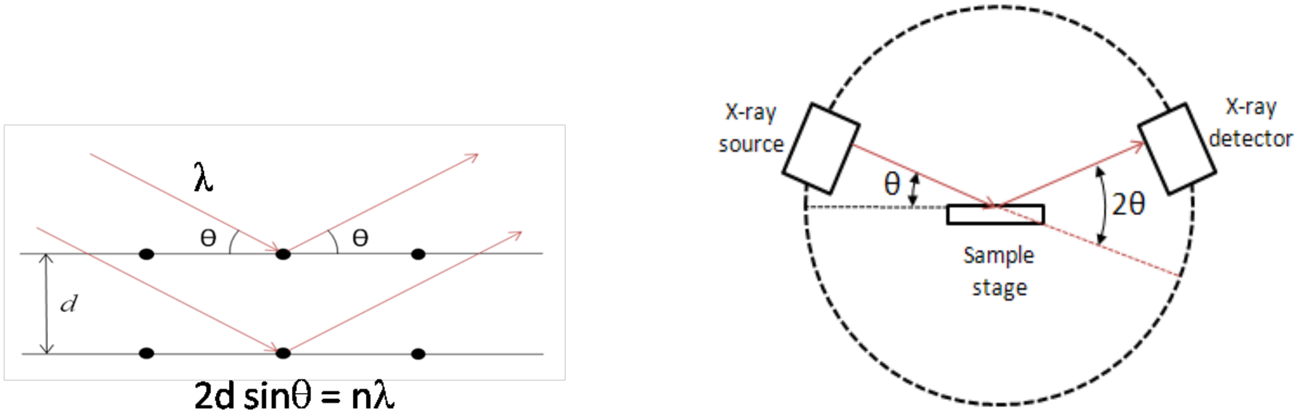

Figure 2.6: Bragg's law of x-ray diffraction and sschematic of X-ray powder diffractometer.

2.4 Characterization Techniques

2.4.1 Crystal structure

The discovery of X-rays in 1895 and law of its diffraction from materials (1920's) enabled scientists to probe crystalline structure at the atomic level. X-ray diffraction is used in two main areas; for the fingerprint characterization of crystalline materials and the determination of their structure. Each crystalline solid has its unique characteristic X-ray powder diffraction pattern which may be used as a "fingerprint" for its identification. Once the material has been identified, X-ray crystallography may be used to determine its structure. Other uses of XRD are determination of grain size, texture and residual stress of materials and compounds. The X-ray diffraction is one of the most important characterization tools used in solid state chemistry and materials science. For such measurements the wavelength of X-rays should be in the range of 0.5 – 2 Å (of the order of distances between atoms or ions in a molecule or crystal). The fundamental of these measurements lie in constructive interference of X-ray beam diffracted from different plane of atoms of crystalline solid as shown schematically in Fig.2.6. Interference phenomena between two reflected rays are governed Bragg's x-ray diffraction law [98].

X-rays are predominantly diffracted by electron density clouds and the scattered X-ray intensity is proportional to the square of the Fourier transform of the charge density:

$$I(\vec{q}) \propto \left| \int d^3 r e^{i\vec{q}.\vec{r}} \rho(\vec{r}) \right|^2 \tag{2.4}$$

Where, ρ(r) is the charge density. The analysis of scattered X-ray intensity as a function of diffraction angles is used to produce electron density map of a given crystal or crystalline structure. Though in theory for perfect crystals I(q) consist of delta functions, in practical cases the diffraction peaks have finite width due to strains, defects, finite size effects and instrumental resolution.

A typical X-ray powder diffraction system mainly consists of an X-ray generator, goniometer, sample holder, and X-ray detector [99]. In this thesis most of the powder XRD pattern are recorded employing Rigaku powder X-Ray diffractometer Model-RINT 2000 consisting of a Cu target X-ray source and a scintillator [NaI(Tl)] detector. The XRD pattern was recorded by employing Cu $K\alpha$ line (λ = 1.54056 Å) and scanning with a typical step size of 0.01°- 0.03°.and dwell time of 1-2 s. Samples for measurements were prepared by crushing the transparent crystal chunks and sieving in to ~10μm size particles.

2.4.2 Crystal Orientation

Laue Back-Reflection technique is used for the determination/orientation of bulk single crystals by fitting of the Laue back-reflection pattern. Fig.2.7 shows a schematic diagram for back-reflection Laue experiments. In Laue method a white X-ray source is used to study the diffraction pattern. As in this case the Bragg angle is fixed for every set of planes in the crystal, each set of planes diffracts a particular wavelength from the white radiation that satisfies the Bragg's law for the values of *d* and *θ* involved. Each point therefore corresponds to a different set of planes. These reflections generate a unique pattern for a particular orientation that is used to identify the crystal orientation. Beam which are diffracted in a backward direction are recorded on a photographic film placed between the X-ray source and the crystal in the back-reflection method [100].

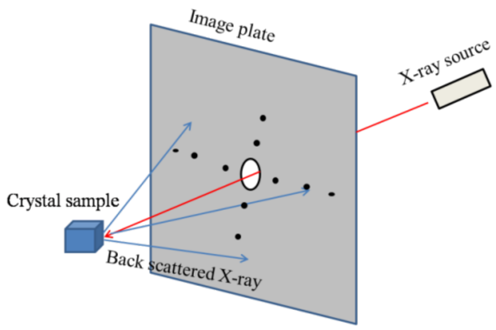

Figure 2.7: The schematics of Laue back reflection method.

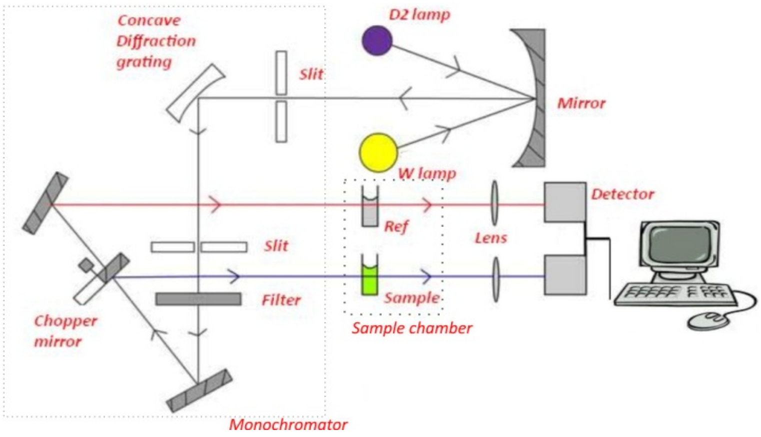

Figure 2.8: Schematic diagram of a double beam UV-VIS-NIR spectrophotometer.

2.4.3 Optical transmission

Transmission/absorption spectroscopy is a strong tool to observe optical quality of a sample and to probe the absorption levels introduced by dopants or impurities. Optical transmission/absorption measurements were carried out on a spectrophotometer that measures intensity of light transmitted/absorbed through a sample with respect to a reference sample (in most cases air or vacuum). The ratio of the intensity of light passing through a sample (I), to that of light without passing through the sample (Io) is called the transmittance, and is usually expressed as a percentage (T). The absorbance, A, is related to the transmittance as

$$A = -\log\left(\frac{T}{100}\right) \tag{2.5}$$

The schematic diagram of a double beam UV/VIS spectrophotometer is shown in Fig.2.8. Here the light is split into two beams before it reaches the sample. One beam is used as the reference and the other beam passes through the sample. Two separate detectors are used for the measurement of light passing through the sample and the reference. Generally, two lamps one deuterium lamp for UV and second tungsten lamp for VIS/NIR, are used to cover UV-VIS-NIR range of the spectrum. Photomultiplier is used for UV/VIS (range 190-850nm) and cooled PbS detector is used for NIR (range 800-2500 nm). The measurements were carried out in the wavelength range from 200 nm to 1100 nm and samples were taken in the form of thick slices (2-20 mm) prepared from the transverse section of the ingot.

2.4.4 Luminescence

Luminescence is UV-VIS-NIR light (apart from the thermal emission) emitted from certain material, called luminescence material, under certain kind of excitation. Some energy source kicks an electron of an atom out of its ground state into a higher energy excited state. The electron then returns to the ground state either by thermally (phonon assisted) transferring its energy to lattice called non-radiative transition or by emitting light photon called radiative transition. With few exceptions, the excitation energy is always greater than the energy (wavelength, color) of the emitted light. Based on the source of excitation luminescence can be put in various subcategories. A few of these subcategories studied in this work are mentioned below.

Photo-Luminescence: Photo-luminescence (PL) is the phenomenon in which absorption of light of a given wavelength by a molecule is followed by the emission of light at longer wavelengths [101]. The wavelength-dependent intensity pattern of emitted energy is called emission spectrum, while the distribution of wavelength-dependent intensity that causes the emission is known as the excitation spectrum. The PL studies of a material may elucidate the electronic structure and dynamics of an excited state of electronic states as it is a property related to the difference between two electronic states, viz. the emitting state and the ground state. The difference in the timing between the absorption of the higher energy photon and emission of secondary photon of lower energy is defined by the luminescence decay time or the lifetime of excitation states. Decay time can vary many orders of magnitude depending upon different materials and weather the transition is allowed or not. Based on practical observations of persistence, PL was historically divided in two categories; fluorescence for life times shorter than 100 μs (generally spin allowed) and phosphorescence for much longer lasting luminescence (up to a few hours and even days: generally spin forbidden).

In the present work, (PL) studies were performed over wavelength range from 300 to 800 nm and temperature range of 77–300K employing Edinburgh fluorescence spectrometer model FLP 920 (schematic shown in Fig.2.9 [102]). The instrument consists of a source, monochromator, sample chamber, emission monochromator and detector. Two types of excitation source viz. Xe or H_2 filled flash lamps were used for recording life times in the range of μs and ns respectively. The lamp produces a broad spectrum of high intensity radiation through the UV-Vis-NIR range which is imaged onto the entrance slit of the excitation monochromator. A specific excitation wavelength with a specific bandwidth is selected by the monochromator and passed from an iris (so that the intensity can be controlled) and then focused onto the sample. A portion of any luminescence from the sample is collected by a lens system and focused onto the emission monochromator. The emission monochromator selects a wavelength and spectral bandwidth of this emission and the light is passed into a photomultiplier tube (PMT) for emission in UV-VIS range. All the emission and excitation spectra were recorded in the reflection geometry by positioning the samples at an angle of 45^o to the excitation beam. Measurements at low temperature were carried out by placing the sample in Oxford Cryostat Model Optistat DN. The recorded luminescence spectra were corrected for spectral sensitivity function of the instrument. The correction file was prepared by recording the spectra under identical conditions after replacing the sample by a scatterer.

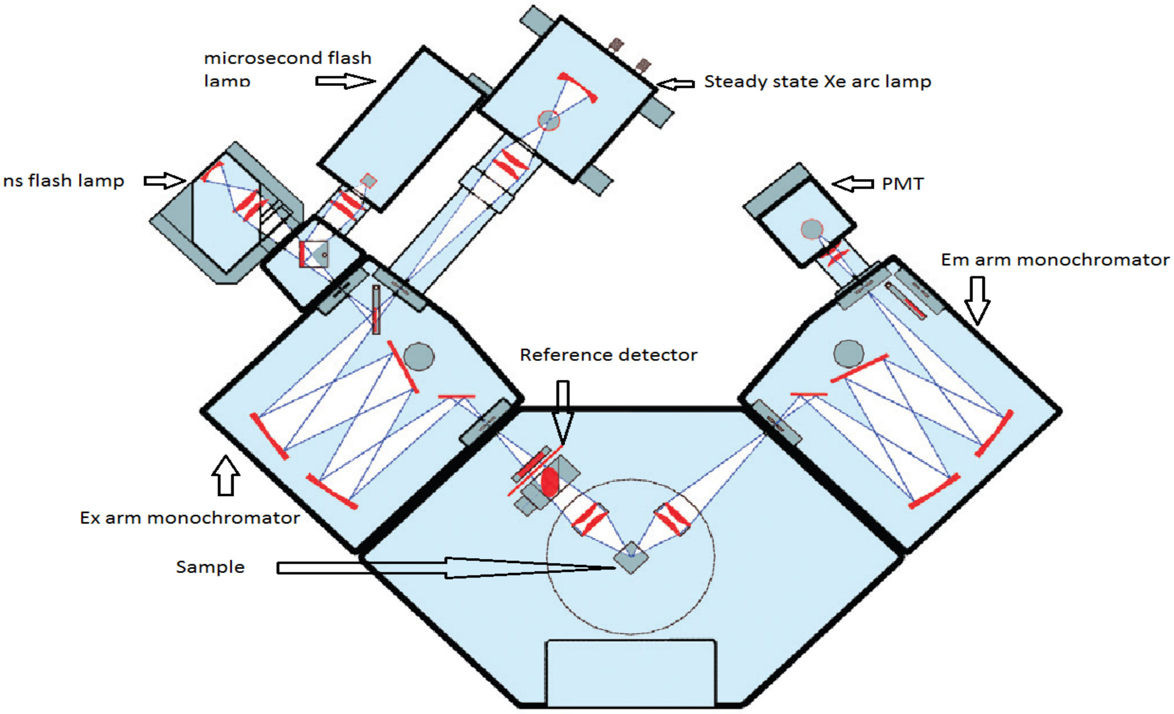

Figure 2.9: The schematic diagram of fluorescence spectrometer FLP920.

The lifetime measurement in this system is based on Time Correlated Single Photon Counting (TCSPC) technique [102]. The TCSPC measures single photons – namely, detection at the quantum limit. The technique requires an excitation source with high repetitive pulse output. The method makes use of the fact that for low level high repetition rate signals the light intensity is usually so low that the probability to detect one photon in one signal period is much less than one. The TCSPC electronics can be compared to a fast stopwatch with two inputs. The clock is started by the START signal pulse and stopped by the STOP signal pulse. The time measured for one START – STOP sequence will be represented by an increase of a memory value in a histogram, in which the channels on the x-axis represent the time. With a high repetitive light source millions of START – STOP sequences can be measured in a short time. The resulting histogram counts versus channels will represent the fluorescence intensity versus time.

Thermally stimulated luminescence (TSL) is a kind of luminescence exhibited by certain materials called thermoluminescent materials. In this phenomenon, the material when irradiated by high energy radiation stores certain amount of energy in the form captured electron and holes by electron or hole traps. These trap centers arise due to localized defects, or imperfections are stationary states that have no formal time dependence though they are not stable energetically. The captured electron and hole get released when thermally agitated on heating. The released electron and holes combine at luminescence center and produce luminescence called thermally stimulated luminescence (TSL or TL) [103]. The TSL occur over a range of temperature typically varying from 4.2 – 700K. The luminescence intensity recorded as function of temperature is called glow curve and the peak is called glow peak. The peak shape and temperature depend on many factors like trap depth, frequency factor, kinetic order etc. All these parameters can be calculated by the analysis of glow peaks. The intensity of luminescence is proportional to the original dose of radiation received and traps density in the material.

To record a TSL glow curve (intensity vs temperature) of small quantities of sample weighing a few mg were taken and were given dose as required by the study using a ^{60}Co gamma source. The sample were heated in the temperature range of 25 – 350^{o}C employing a linear heating rate of 1-2 K/s. The schematic of TSL setup is shown in Fig.2.10. A photomultiplier tube with a GaAs photo cathode having almost flat response in the range from 300 nm to 800 nm was used for recording the TSL. The TSL spectra were recorded by quickly scanning the monochromator once over the 200 to 700 nm while maintaining the sample temperature just below the glow peak position.

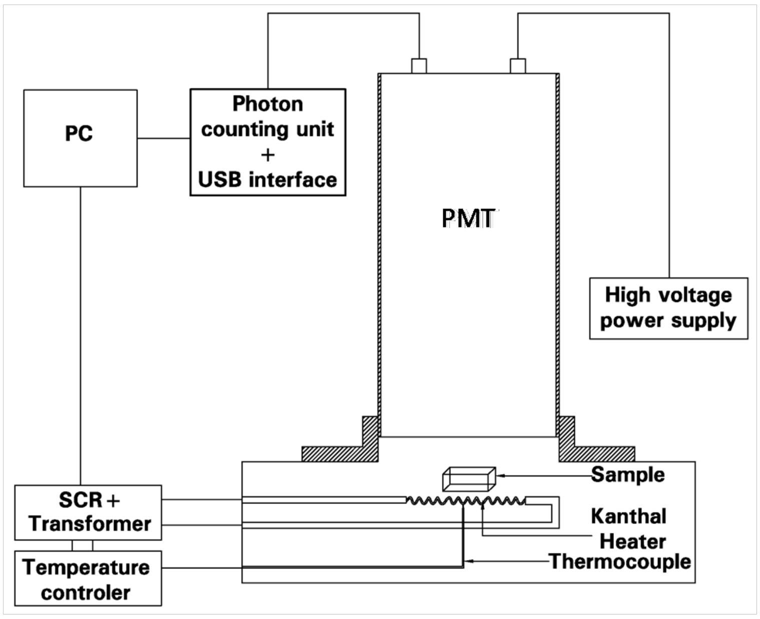

Figure 2.10: A typical setup for recording thermally stimulated luminescence.

Radio-luminescence (RL) is the phenomenon by which light is emitted from a material on bombardment with high energy radiation like X-ray, gamma-ray etc. The radio-luminescence is somewhat different than the PL as in RL the electrons are excited deep in conduction band and there are many complex phenomena involved in this process. The details of this process are given in next section under the heading scintillation process and scintillation detector. The intensity distribution of luminescence, generated due to excitation from high energy radiation, as a function of the wavelength is called radio-luminescence spectrum. In this study, X-ray induced emission spectra were measured using an in-house built set-up. The source was an X-ray tube with a Cu target. The accelerating voltage and tube current were set at 40 kV and 30 mA, respectively. An Avantes make (model: 3648) spectrograph was used to measure the emission spectra.

2.5 Scintillation and Scintillation detector

Luminescence causes by high energy radiation is called scintillation. The core of the scintillation process is the transformation of energy of ionizing radiation into a variety of optical photons. The whole scintillation process (from absorption of energy to generation of optical photon) can be subdivided into following steps [104]; **Conversion:** Interaction of ionizing radiation with the matter and creation of primary (Compton scattered, photo-emitted etc.) high energy electrons followed by interaction of the primary electrons with the bulk of the matter and formation of secondary (Auger, delta-rays, etc.) high energy electrons and production of hot carriers (electrons, holes, excitons) within the ionization track; **Transportation:** Diffusion of the hot carriers from the point of creation to low ionization density regions and their thermalization and creation of electron-hole pairs with energy roughly equal to the band gap; **Recombination:** Energy transfer from the thermalized electron-hole pairs to or direct capture of the thermalized carriers by the luminescence centers and emission. These processes are schematically shown in Fig.2.11.

Scintillators are materials that convert the energy of ionizing radiation into a pulse of light (UV to visible range). Scintillation material can be gaseous, liquid, glass-like, organic (plastics), or inorganic. Scintillation material should be transparent to its own scintillation light. Therefore, for their application in radiation detection or monitoring these can be taken only in few specific phases like single crystals or optically transparent ceramics. Inorganic wide band gap ionic crystals are the most widely used scintillators for detection of X-rays, gamma rays, and thermal neutrons.

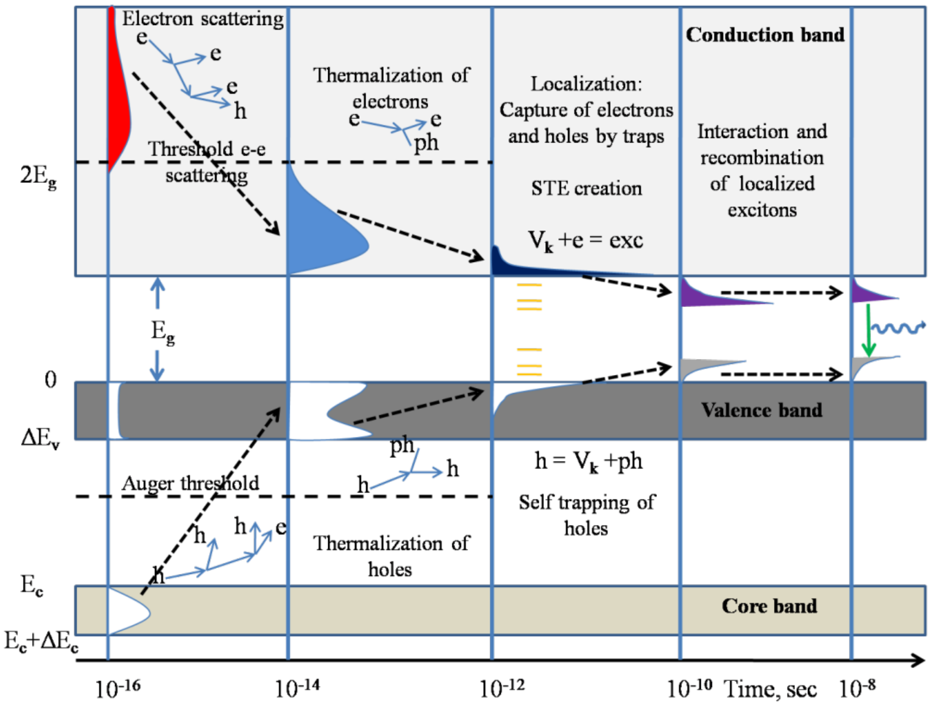

Fig.2.11: Schematic depiction of the scintillation process.

Scintillation Detectors: In this study scintillation detectors were fabricated using the grown single crystal to check their scintillation performance. A scintillator detector consists of following components; A scintillator material: to convert the high energy radiation in to detectable light in proportional to the energy of the ionizing radiation; Photo-detectors: to detect the light produced in scintillator and generate a processable electrical signal proportional to the detected light (PMT, Photodiode etc); Preamplifier: to amplify the signal received from the photo-detector and give a voltage pulse; Shaping amplifier: to shape the pulse received from the preamplifier and transfer it to the pulse height analyzer (0-10 volt pulse); Pulse height analyzer: a multichannel analyzer that assigned register each pulse a channel number (from 0 – 8191 for 8K MCA) proportion to its voltage (0-10 volt). Schematic of detector configuration using a photodiode read out is given in Fig.2.12.

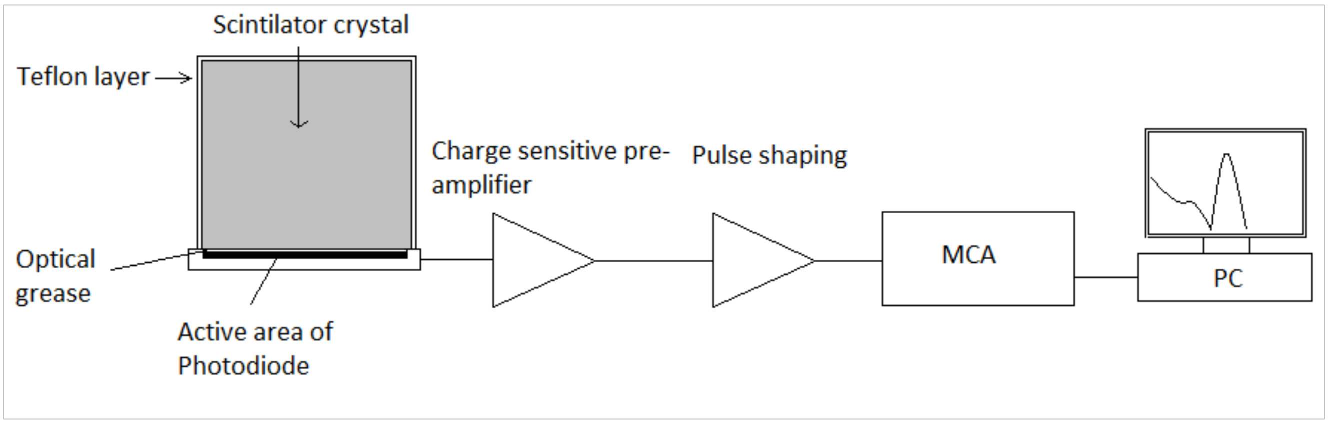

Figure 2.12: Schematic of photodiode based scintillator detector.

2.6Structural refinement

The crystal structure is refined by fitting the entire profile of the diffraction pattern to a calculated profile employing Rietveld method. The X-ray powder diffraction data, obtained from the grown crystals has been analyzed by using GSAS program based on Rietveld method. The lattice parameters, atomic position coordinates, bond length and bond angles between atoms were calculated from the refinement were used to perform calculations within density functional theory.

The Rietveld method is the profile refinement method for analyzing powder diffraction data which is widely used in the field of crystallography [105, 106]. The dependence of full width at half maxima (FWHM) of the reflection i.e. H_k on θ_k for the contribution of a single reflection k can be written in simplified form as [107],

$$H_k = U\, tan^2\theta_k + V\, tan\, \theta_k + W \tag{2.6}$$

Where U, V, W are half-width parameters independent of θ_k. This gives an adequate representation of the variation of FWHM with Bragg angle. U, V, W must be treated as adjustable variables in the refinement. Least-squares refinement is achieved by minimizing the function,

$$M = \sum_i w_i \left[Y_i(obs) - \frac{1}{c} Y_i(cal)\right]^2 \tag{2.7}$$

Where Y_i is the contribution of the Bragg reflection k to the intensity measured at position $2\theta_i$. The summation is over all points in the pattern. w_i is a weighting factor which is inversely proportional to the variance of quantity in square brackets and c is an overall scale factor. The parameters used in refinement of least-squares are of two kinds. There are two group of parameters: (I) ‘structural parameters’ viz. overall isotropic temperature parameter, fractional coordinates, occupation fraction, and isotropic temperature factor individual non-equivalent atoms; (II) 'profile parameters' viz. half-width parameters (U, V, W), zero position of detector and unit-cell parameters. Further parameters may be added as coefficients of the anisotropic temperature factors in first group while the second group may contain the parameters to allow the skewness of the reflections at extreme scattering angles or for preferred orientation. The quality (especially resolution) of the diffraction pattern determines the maximum number of structural parameters which can be safely included in a powder refinement.

The General Structure Analysis System (GSAS) is a set of programs for the processing and analysis of both single crystal and powder diffraction data obtained with X-rays or neutrons [108, 109]. In addition, powder diffraction data from a mixture of phases can also be analyzed by refining structural parameters for each phase. EXPGUI software is a Graphical User Interface (GUI) for GSAS which is written in FORTRAN and organized into several main programs designed for specific type of tasks or type of crystallographic calculations. The quality of fit is determined by the value of reduced χ^2. The χ^2 is defined by the minimization function as

$$\chi^2 = \frac{M}{(N_{obs} - N_{var})} \tag{2.8}$$

Where N_{obs} is the total number of observations in all histograms and N_{var} is the number of variables in the least squares refinement. Minimization function 'M' is made up of several components and in case of powder diffraction data is written as

$$M = \Sigma\, w\, (I_o - I_c)^2 \tag{2.9}$$

Where, I_o and I_c are observed and calculated intensities respectively.

2.7 Electronic band structure calculation

Knowledge of electronic structures of solids are helpful in predicting its relative stability, chemical bonding, atomic relaxation, phase transitions, electrical, mechanical, optical or magnetic behavior etc. These prediction may be used for systematic material designing or explaining certain experimental observation like defect formation, reflectivity, absorption etc.

The band structure problem is a many-body problem that includes the relative motion of electrons and of nucleus in a crystal. The many-body quantum mechanical problem can be solved by mainly two approaches, Hartree-Fock (HF) or with the aid of density functional theory (DFT). The HF method based on wave function solution, treats exchange energy, but correlation effects are ignored by definition while the DFT is based on electron density rather than on wave functions and it treats exchange and correlation but both approximately. In this thesis DFT based theoretical calculation is used to calculate electronic structure of the material and hence only this will be described in detail.

Density functional theory

The DFT is one of the most powerful and widely used ab-initio methods for the calculation of ground state properties of metals, semiconductors and insulators [110-112]. It is based on the Hohenberg and Kohn theorem [113], which states that all ground state properties of an inhomogeneous electron gas can be described by a function of the electron density, and provides a one-to-one mapping between the ground-state density and the external potential. The main idea of the DFT is to solve a many body problem of interacting system of electrons and nuclei by mapping on to a one-electron reference system that leads to the same density as real system. This approximation reduces the variables to three (spatial coordinates x, y, and z) rather than 3N (N number of bodies) degrees of freedom. Spin densities $\rho_\sigma(r)$ are the key quantities here and total energy can be written as,

$$E_{tot}(\rho) = T_s(\rho) + E_{ee}(\rho) + E_{Ne}(\rho) + E_{xc}(\rho) + E_{NN} \tag{2.10}$$

where T_s, E_{ee}, E_{Ne}, E_{xc}, E_{NN} are the kinetic energies of the non-interacting particles, electron-electron repulsion, nuclear-electron attraction, exchange-correlation and repulsive Coulomb energy of fixed nuclei respectively. Out of infinite number of possible densities the one that minimizes the energy is the ground state density. The problem therefore is to solve the Kohn-Sham (KS) equation [114]

$$\left[-\nabla^2 + V_{Ne} + V_{ee}\big(\rho(r)\big) + V_{xc}^{\sigma}\big(\rho(r)\big)\right]\chi_{ik}^{\sigma}(r) = \epsilon_{ik}^{\sigma}\chi_{ik}^{\sigma}(r) \tag{2.11}$$

The spin densities can be written by summing over the orbitals as,

$$\rho_\sigma(r) = \sum_{ik} \rho_{ik}^{\sigma} \, |\chi_{ik}^{\sigma}(r)|^2 \tag{2.12}$$

ρ_{ik}^{σ} are the occupation numbers such that $0 < \rho_{ik}^{\sigma} < 1/\omega_k$, where ω_k is the symmetry-required weight of point k. Orbitals χ_{ik}^{σ} are wave functions of single particle (quasiparticle) but not the wave function of electrons. Overall density of these quasiparticles is equal to true electron density.

Practical applications of DFT are based on approximations and one must choose the function that is used to represent exchange and correlation (*xc*) effects. But after this approximation one can solve the effective Hamiltonian with high precision. A common approximation is the so-called local density approximation (LDA). In LDA the exchange-correlation energy Exc(ρ) of an inhomogeneous system is approximated by the exchange-correlation energy of a homogeneous electron gas, which can be evaluated accurately. Here the density at each point in the space is replaced by a local value of the charge density ρ (*r)* and hence two approximations are taken as, i) exchange-correlation energies E_{xc} written in terms of a local exchange-correlation energy density μ_{xc} times the total electron density as,

$$E_{xc} = \int \mu_{xc}\,(\rho\uparrow, \rho\downarrow) * [\rho\uparrow + \rho\downarrow)dr \tag{2.13}$$

and ii) the particular form chosen for that μ_{xc}. Thus E_{xc} for a particular density ρ(*r*) could be found by dividing the material in infinitesimally small volumes with a constant density. The contribution from each such volume is same as from homogenous gas filled in identical volume and having same density as the original material has in this volume. Though, in many cases (calculation of lattice constant, bulk moduli, etc.) the LDA works well and is used widely for three decades for great variety of systems [115].

Though LDA calculations often yield results in close agreement with experimental values but there are cases where they show large discrepancies. Recent progress goes beyond the LDA by adding gradient terms of the electron density to the exchange-correlation energy or its corresponding potential. Thus,

$$E_{xc}^{GGA} = \int f\,(\rho\uparrow, \rho\downarrow, \nabla\rho\uparrow, \nabla\rho\downarrow)dr \tag{2.14}$$

Therefore in GGA exchange correlation contribution of every infinitesimal volume not only depends on local density in that volume, but also on density in neighboring volume i.e. gradient of density. More advanced approximations are being used in many modern codes using DFT to improve accuracy for certain physical properties. There are several different parameterizations of the GGA e.g. the one by Perdew et al or by Perdew, Burke and Ernzerhof (PBE), which are recommended options [116, 117].

There are many variational methods for solving Kohn-Sham equation for a system. All variational methods differ from each other only by the choice of the basis set and by the construction of the crystal potential. Several efficient basis methods developed in last four decades are widely used for band structure calculations of solids. A designated choice of basis set serves for specific purposes. For example the linearized muffin-tin orbital (LMTO) method or augmented spherical wave (ASW) method provides very fast band structure calculations, with an accuracy which is sufficient for many applications in solids. But usually simple basis methods are very fast but not very accurate. Methods with more complicated basis and potential constructions are appropriate for high precision electronic structure calculations like augmented plane wave (APW) method, full-potential linearized augmented plane wave (FPLAPW) method, projected augmented wave (PAW) method, full-potential local-orbital minimum-basis method etc. The present work uses the full potential linearized augmented plane wave (FPLAPW) method [118, 119]. This method has proven to be one of the most accurate methods for performing electronic structure calculations for solids. For valence states, relativistic effects can be included either in a scalar relativistic treatment [120] or including spin-orbit coupling variationally [121, 122] and core states are treated relativistically [123]. The problem of rapid variation of wave function near nuclei can be solved by dividing the unit cell into non overlapping atomic spheres "A" (centered at the atomic sites) and an interstitial region "B" (Fig. 3.2) [124, 125]. Different basis sets are used in these respective regions. The idea behind this lies in the fact that the inner region of atom (near to nuclei) is shielded from outer region and electron behave as they are in free atom, therefore, could be described by atomic like functions. While in the outer region far away from nuclei (where most chemistry happens), electrons are free, thus can be represented by plane waves.

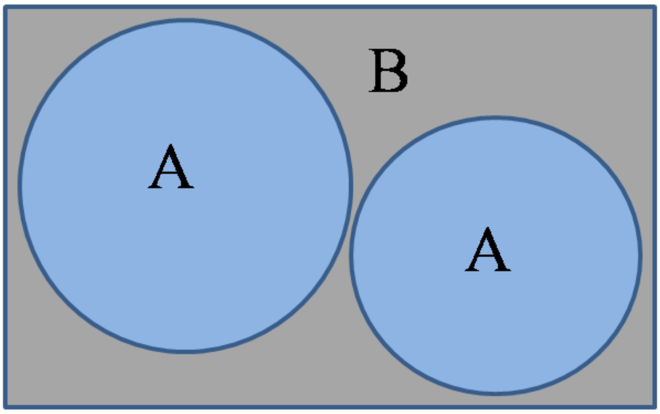

Fig.2.13: Partitioning of the unit cell into atomic spheres (A) and an interstitial region (B).

The computer code WIEN2k [126] and EXCITING [127] are used to study crystal properties on the atomic scale by employing linearized-augmented-plane-wave (LAPW) method within density functional theory (DFT).

The band structure of $NaBi(WO_4)_2$ (NBW) was calculated employing the WIEN2K code. It was observed that the valence band (VB) is mainly formed by non-bonding states of the oxygen *p* orbital, with a very little contribution coming from the tungsten *d* orbital. The conduction band (CB) is mainly formed from W d states with a similar amount of contributions coming from the *p* states of bismuth and oxygen. Code Exciting was used to calculate the band structure of $NaGd(WO_4)_2$. The results were similar to the NBW with the exception that the levels of Gd are formed in the forbidden region at the top of valence band.

The band structure of CsI, CaF_2 were calculated using EXCITING code. The band structure of CsI shows a direct band gap of approximately 3.8 eV. The top of the valence band consists of iodine electronic states while the bottom of the conduction band was made of Cs electronic states. On the other hand CaF_2 shows an indirect band gap (approximately 7.5 eV). The top of valence band, in CaF_2, is mainly formed of F orbitals while bottom of conduction band consist of Ca orbitals.

CHAPTER 3

GROWTH OF SINGLE CRYSTAL OF TL DOPED CsI BY A MODIFIED BRIDGMAN CRYSTAL GROWTH TECHNIQUE

Thallium doped CsI (CsI:Tl) single crystal is an old and well known scintillator material and has been deployed in a variety of applications owing to its high density, sufficient light yield and suitably matched emission with photodiodes [128-131]. Though it is an old scintillator, active research to improve its scintillation properties is going on at full swing in scintillation community [132-137]. It shows better scintillation efficiency (if used with suitable readout) and is less hygroscopic and less brittle than NaI. This material could not achieve its full potential in the past due to the unavailability of a matching photo-multiplier tube (PMT). However, use of P-I-N photodiodes that show good efficiency at longer wavelengths and compact in size, has renewed the interest in the CsI:Tl crystals [138]. The CsI based scintillation detectors are efficient to detect charged particles with energies of E/A=200MeV [132]. The CsI:Tl crystals based detectors are less expensive than solid state detectors, less hygroscopic than NaI:Tl crystals, and can be easily machined into different shapes, therefore have been incorporated in many large solid angle detection arrays [139]. Many problems related with CsI:Tl based detectors like temperature dependence has been solved by holding the temperature constant, and by reading out the detectors via photodiodes instead of photomultipliers, whose gains may vary with time.

Scintillator alkali halide crystals, in particular, NaI:Tl, CsI:Tl and CsI:Na are generally produced using the directional crystallization of the corresponding melt in a crucible using the Bridgman/Stockbarger method [140,141]. Single crystals of CsI can be grown by Bridgeman as well as Czochralski methods. Though, the crystal growth using the Bridgman method is not a problem, sticking of the crystal with crucible wall and hence recovery of the crystal after the growth and thermal and mechanical stresses generated therein are important issues and of considerable interest [141]. Luminescence and scintillation properties of CsI:Tl are also found to be highly dependent to various stages of crystal preparation viz. starting material preparation, growth technique and post growth treatments, etc. Despite considerable efforts for many decades on this material, its poor radiation hardness and long afterglow are still major areas of concern that hinder its application to several other useful fields [142].

In this chapter the main focus is on the development of a cost effective and efficient technique to grow alkali halide crystals particularly doped and pure CsI and NaI single crystals. Two different approaches that yielded, with considerable ease, good quality device grade single crystals of Tl doped CsI have been developed during the course of this work.

3.1 Growth of CsI:Tl single crystals in carbon coated silica crucibles

In this section the growth of high quality radiation hard Tl doped CsI single crystals in carbon coated fused silica crucibles by a gradient freeze technique is described. Effect of axial temperature gradient (inside the melt), cooling rate and post growth annealing on the crystal growth and luminescence properties were studied and optimum conditions were determined. Gamma-ray detectors were fabricated and characterized to study the effect of growth conditions on the scintillation quality of crystals. The best resolution found (with PMT readouts) for optimum growth conditions was about 7.5% at 662 keV gamma-ray (from a ^{137}Cs source) which is comparable to the reported values [143].

3.1.1 Furnace and crucible description

A crystal growth furnace has been designed to have a positive and adjustable temperature gradient (from the bottom to the top of the furnace). Fig.3.1 shows the gradient of the furnace with an empty crucible along with the furnace diagram. To determine the actual axial temperature profile in the melt, potassium chloride was melted in a silica crucible that has an open end. It may be noted that KCl can be heated in air (melting point: 780°C) and has a heat capacity approximately equal to that of CsI. A K-type thermocouple enclosed in a thin silica tube was inserted in the melt and the profile was recorded as a function of position from the bottom to the top in the furnace. The axial temperature profiles in the melt for different positions of the controlling thermo-couples in the furnace are also shown in Fig.3.1.

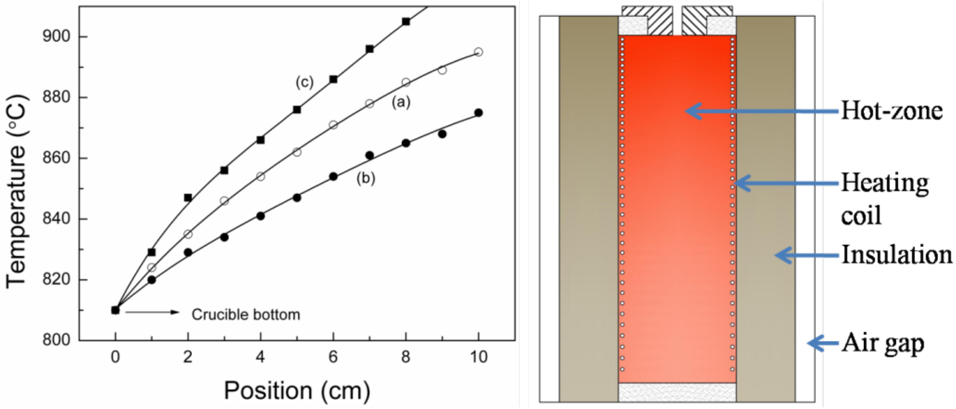

Figure 3.1: Temperature profiles in the furnace (a) blank furnace, (b) furnace with silica crucible (controlling thermo-couple at the crucible bottom) and (c) furnace with crucible (controlling thermo-couple 3 cm above the crucible bottom). Furnace diagram is shown on the right side of the figure.

Fused silica crucibles 35 mm in diameter with conical bottom that had thin carbon films deposited on the inside surfaces were taken for the growth experiments. To deposit carbon films, first the crucible was cleaned using a 10% HF solution for a few minutes and was transferred to a horizontal tubular furnace and heated up to 900°C. Argon was flown into the tubular furnace through a flask containing n-hexane that on cracking deposited a carbon film on the crucible walls. The carbon film coated crucible was transferred in a vacuum furnace and further annealed at 1100ºC for 2 h. Fig.3.2 shows the design of the crucible and its appearance before and after the carbon coating.

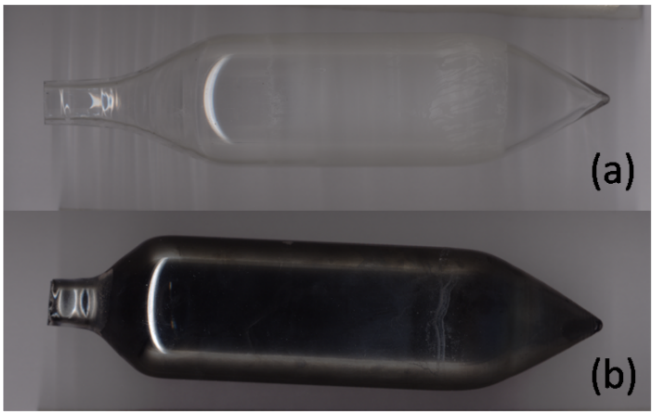

Figure 3.2: Photograph of silica glass crucibles (a) before and (b) after carbon coating.

3.1.2 Material preparation and dehydration

The 500 g of high purity (99.99%) CsI was taken in a clean and dry carbon coated crucible. After filling of material the crucible was placed in the furnace (already at 50°C) and was connected to a vacuum system consisting of a rotary and cryo-sorption pumps. The crucible was evacuated to $1x10^{-2}$ mbar pressure. After this, the temperature of the furnace was increased up to 250ºC in the steps of 50ºC under vacuum. A one hour dwell was given at each step and the crucible was thoroughly shaken in between to avoid formation of lumps during the dehydration process. After the completion of dehydration the crucible temperature is brought down to 50ºC and 1.275 g of TlI (0.2 mol%) is mixed in the dehydrated material in a manner that the dehydrated material is least exposed to ambient moisture. Again the crucible is connected to the vacuum system and evacuated gradually to $1x10^{-2}$ mbar pressure. After this the furnace temperature is increased to 150ºC in the step of 50ºC with a dwell of 30 minutes at each step. This completes the dehydration process of the material though finally a proper visual inspection of the material is required to ensure the complete dehydration of the material. After this the crucible is sealed using an LPG gas torch under the running vacuum condition and at ~1x10^{-2} mbar pressure of Ar (The crucible is flushed with Ar gas 3-4 times when the crucible is at 100ºC).

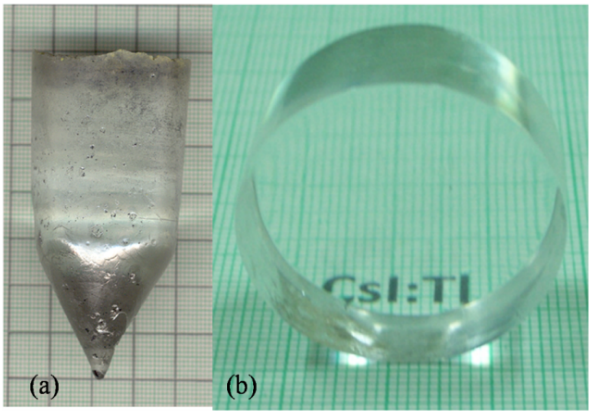

Figure 3.3: Photograph of (a) crystal ingot and (b) polished cylinder.

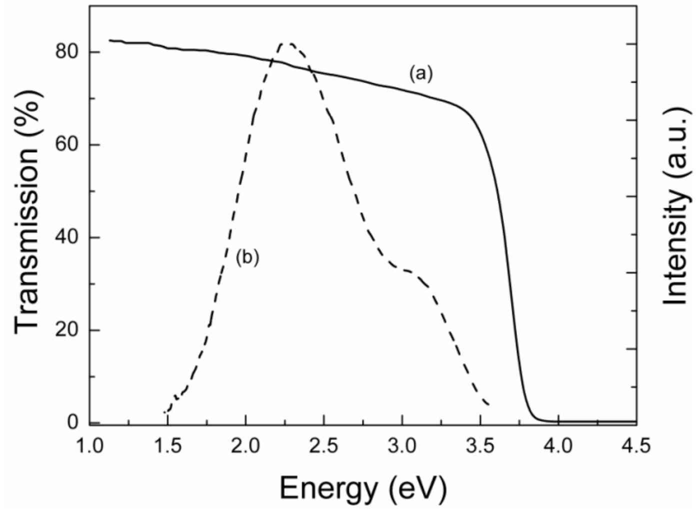

Figure 3.4: Transmission (a) and fluorescence (b) spectra of 0.2 mole% Tl doped CsI single crystal. (sample thickness 20 mm).

3.1.3 Crystal growth

After dehydration and sealing the crucible was placed inside the furnace on a growth station and temperature was raised so that the bottom of the crucible was at 640°C. Melt was kept at this temperature for 4 h and then cooling was started. Two different cooling rates, 4°C/h and 2°C/h, were applied for the growth. The growth experiments were carried out at two different temperature gradients (10 and 15°C/cm) and for different Tl concentrations in crystals of size 35 mm in diameter and 40 mm in length in each growth experiment. Different annealing procedures were used to study the effect of annealing on the crystal quality. In some crystals

(Type-I), the growth was followed by a slow cooling (25°C/h) and post growth annealing at 400°C in a uniform zone for 10 h. The other crystals (Type-II) were cooled at a faster rate (~50°C/h) down to room temperatures. Cylindrical samples of size 35 mm in diameter and 25 mm in length were cut from the ingots for the optical characterization (Fig.3.3). A typical transmission spectrum of a polished CsI:Tl cylinder is shown in Fig.3.4.

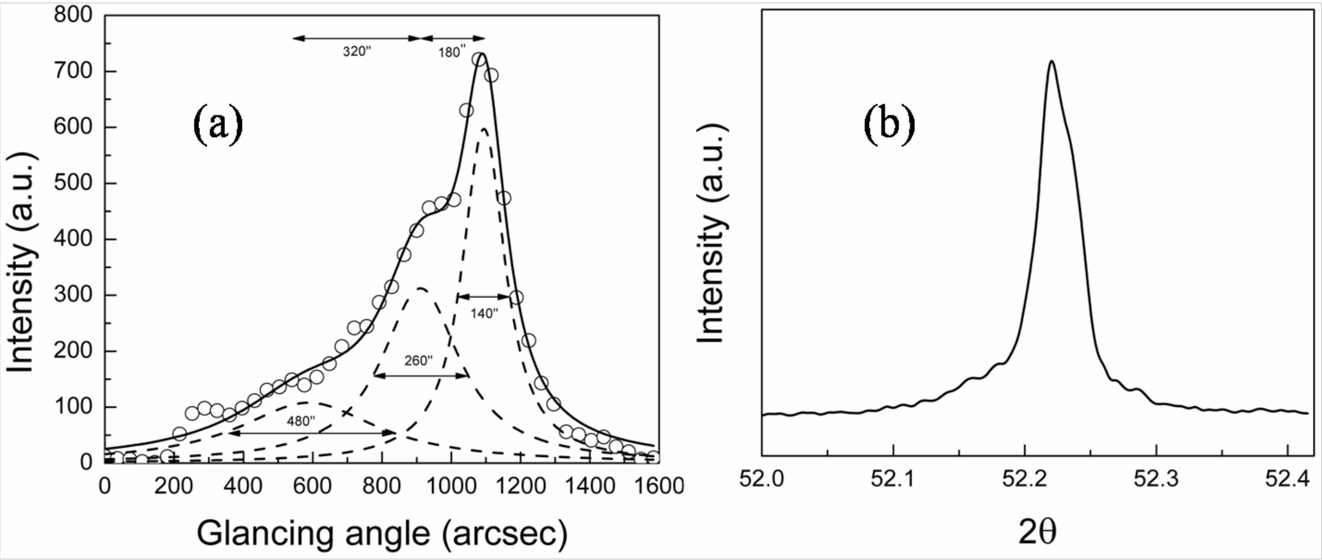

Figure 3.5: (a) Rocking curve for (4 2 2) plane of 0.1 mole% Tl doped CsI and (b) 2Θ position of same plane. (X-ray energy- 9750 eV).

3.1.4 High-resolution X-ray diffraction experiment

Thin slices of as-grown crystals were cut carefully and polished to the optical finish. Single crystal XRD was recorded on an angle dispersive XRD (ADXRD) beamline (BL-12) at the INDUS-2 synchrotron radiation source [144]. The beamline consists of a Si(311) based double crystal monochromator and a collimating pre-mirror for high energy resolution. The measured energy band-width and the angular resolution (for single crystal diffraction) are 1.4eV (at 8 keV) and 16 arc-sec, respectively. The measurements were carried out using a six circle diffractometer (Huber 5020) and a scintillation detector (Fig.3.5).

3.1.5 Optical and scintillation properties

Transmission spectrum was recorded in the wavelength range from 200 nm to 1100 nm employing a double beam photo-spectrometer Chemeto 2500. The polished samples (20 mm thickness) were exposed to the day-light for 10 days to study its effect on the transmission characteristics (Fig.3.6 and Fig.3.7). For the photoluminescence measurements samples (2 mm thick) were cut from the crystal ingot and polished to optical finish. Thermally stimulated luminescence (TSL) glow curves (Fig.3.8) of Type-I and Type-II crystals were recorded in the 25-200°C range employing a heating rate of 0.5°C/s. Luminescence spectra (Fig.3.4b) as well as afterglow spectra (Fig.3.9a) were recorded in the range 200-900 nm in a reflecting geometry employing a florescence spectrometer Edinburgh model FLP-920. The TSL emission spectrum (Fig.3.9b) was recorded by holding the sample at 45°.

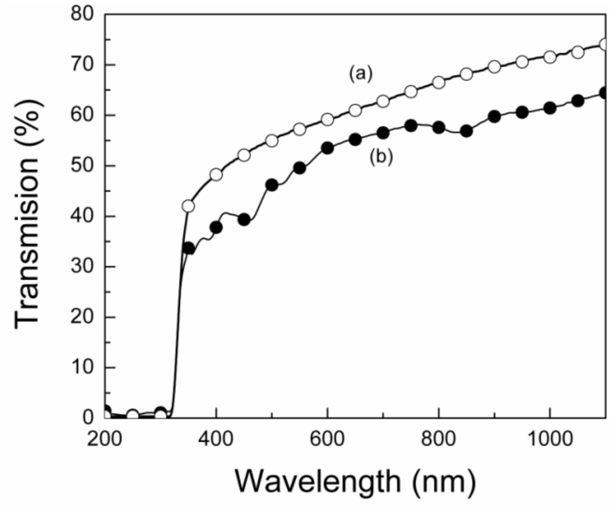

Figure 3.6: Transmission spectra of Type-I (a) and Type-II (b) crystals after 10 days of daylight exposure (sample thickness - 20 mm).

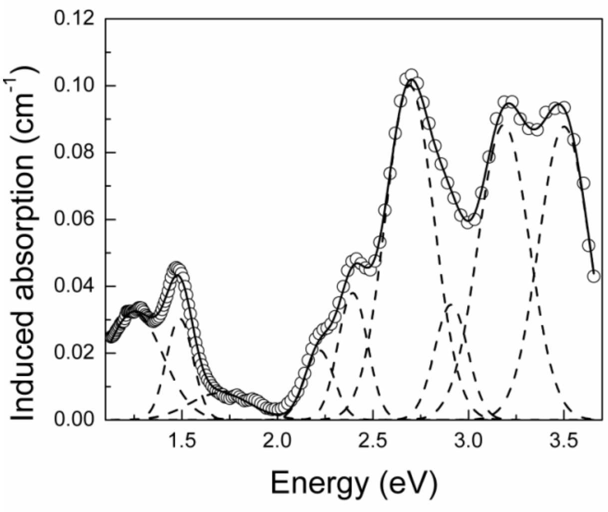

Figure 3.7: Calculated induced absorption (○), individual fitted peaks (----) and envelope fitted peak (—).

Scintillation studies were carried out on a 30 mm diameter and 25 mm long crystal (Type-I) that was wrapped with 10 layers of Teflon tape leaving one face open to connect with a PMT. Gamma spectra of ^{137}Cs, ^{134}Cs, ^{60}Co, ^{22}Na and ^{57}Co sources were recorded using the detector assembly consisting of CsI:Tl scintillator, a PMT (Electron Tube Limited Type: 9814A), a preamplifier, a spectroscopic amplifier and an 8k multi-channel analyzer. A shaping time constant of 3 μs was used (Fig.3.10).

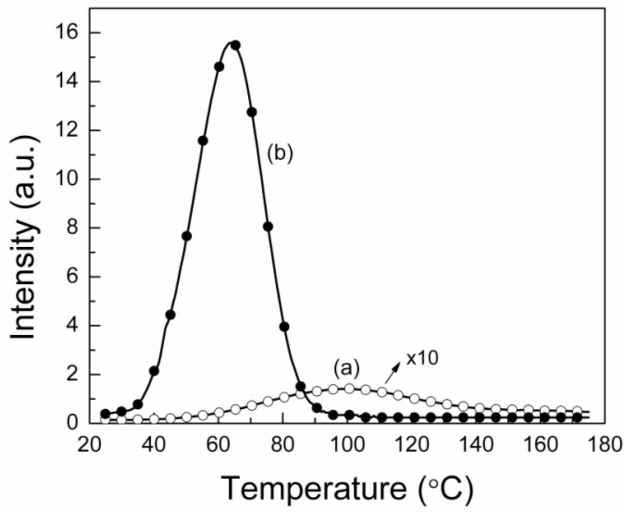

Figure 3.8: TSL glow curves of (a) Type-I and (b) Type-II crystals. (heating rate 0.5ºC/s).

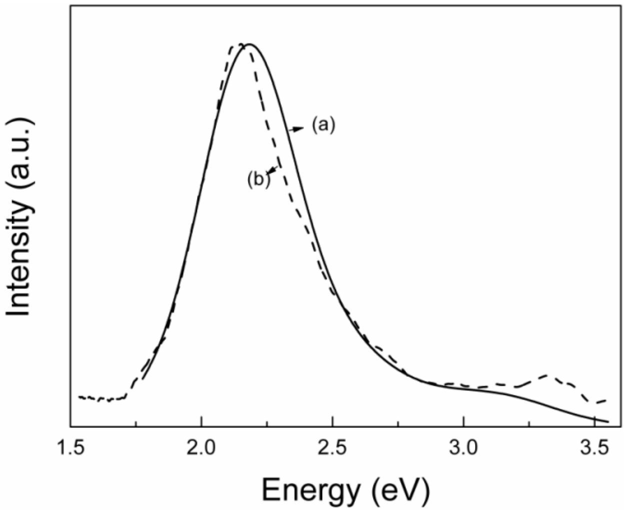

Figure 3.9: Afterglow (a) and thermally stimulated glow (b) spectrum of type-II crystal.

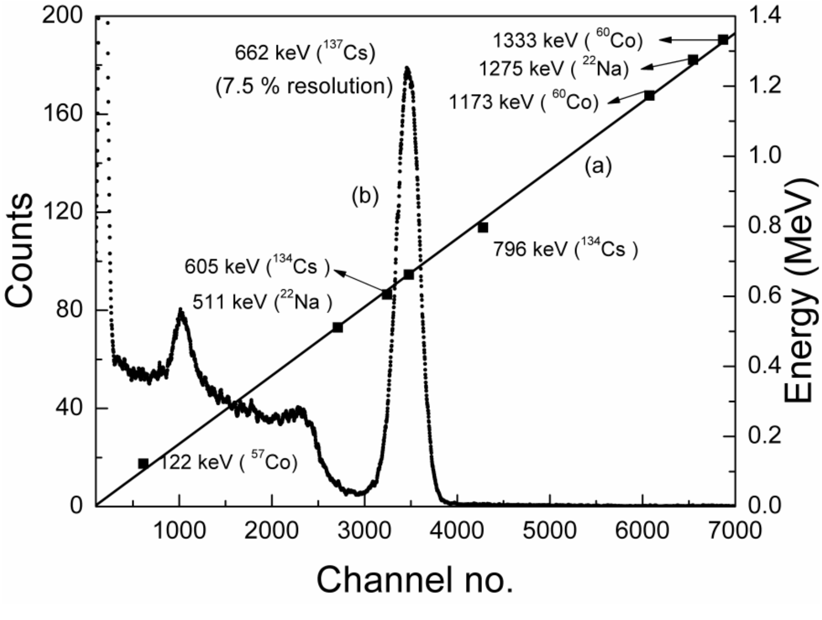

Figure 3.10: Scintillation performance of 0.2 mole% Tl doped CsI crystal (a) Calibration curve drawn from detector response to different radionuclide and (b) a typical gamma spectra of ^{137}Cs recorded using detector (30 mm diameter and 25 mm thickness).

3.1.6 Discussion

The crystal ingots were visibly clear of any carbon particles and were highly transparent. As no part of the furnace or crucible was moving or vibrating, the probability of peeling off the carbon film from crucible walls and mixing with the melt was minimal. Upper parts of the crystals which were grown employing a temperature gradient (10°C/cm, Fig.3.1b) show a cloudy structure with a definite pattern. On analysis (using SIMS) it was found that Tl concentration in that part of crystals was relatively high (0.25-0.3 mole % for 0.2 mole % doping). This indicates a constitutional supercooling due to the segregation of Tl and low temperature gradient. A slower cooling rate (2°C/h) could not resolve the problem. In view of these observations, growth experiments were carried out under a higher temperature gradient (15°C, Fig.3.1c) which successfully solved the problem of constitutional supercooling. A typical photograph of a crystal grown in a higher temperature gradient and slow cooling rate is shown in Fig.3.3(a). Transmission and luminescence spectra of this crystal are shown in Fig.3.4. The spectra do not show any extra peaks related to carbonate or any other impurities. This observation supports that the carbon coating was of good quality without any oxygen contamination and free of other impurities.

High resolution diffraction curve recorded for the 0.1% Tl doped CsI single crystal (not annealed) is shown in Fig.3.5. The X-ray rocking curve (Fig.3.5a) was measured for the (4 2 2) plane (Fig.3.5b). It can be seen from the rocking curve that there are low angle grain boundaries in the crystals. The separation of the grains in the plane is about 200 arc-sec. These low angle grain boundaries may arise during the growth itself or during the processing of the crystal owing to its plastic nature. N. Balamurugan et al [145] have reported an FWHM of the main rocking curve to be 480 arc-sec for the 0.06% Tl doping while in the present work an FWHM of about

140 arc-sec was obtained even at a higher Tl doping concentration of 0.1%. The carbon coating on the crucible wall that prohibits sticking of the crystal to the crucible also minimizes the stresses generated due to different thermal expansions of crucible and the crystal. The low angle grain boundaries may also arise due to the crystal processing (cutting/ polishing). These mechanically generated stresses could be eliminated by annealing the crystal at 400°C which is supported by a better performance of detector assemblies fabricated using annealed crystals. Thus from HRXRD study it is clear that crystals grown using the method described here, are of good quality compared to conventionally grown crystals.

The transmission spectra of Type-I and Type-II crystals after a daylight exposure for 10 days at room temperature are shown in Fig.3.6. It is evident that the absorption in Type-II crystals has been induced. This induced absorption is calculated using the following equation,

$$\mu = \left(\frac{1}{d}\right) ln\left(\frac{I_0}{I}\right) \tag{3.1}$$

where, d is sample thickness in cm, I_0 and I are transmission in percentage before and after the exposure. Calculated curves are then de-convoluted into their constituent peaks. The combined curve is presented in Fig.3.7. A total number of 9 peaks could be clearly identified which are in good agreement with the reported values [146, 147]. In order to confirm that the defect centers induced by high energy radiation and daylight exposures are similar, the Type-II crystals were irradiated with a ^{60}Co gamma radiation source. The same induced peaks were observed in the transmission spectra recorded for the irradiated crystal. The TSL glow curves for Type-I and Type-II crystals (For radiation dose of 200 Gy) are shown in Fig.3.8. It is apparent from this figure that the number of defects/traps are far less (two orders) in Type-I crystals compared to those in Type-II crystals. The peak temperature shifts towards higher temperatures for the Type-I crystals. This result is in agreement with the HRXRD data. After-glow and TSL emission spectra shown in Fig.3.9 suggest that the same kind of center is responsible for both the phenomena.

As UV light does not have sufficient energy to create new defect centers in the CsI:Tl crystal, the root cause of coloration of Type-II crystals may lie somewhere else. One possibility for such coloration could be proposed as the capture of electrons by defect centers already formed during the crystal growth process. In Type-I crystal no considerable day light coloration was found. Another benefit of the post growth crystal annealing in the controlled ambient of the silica ampoule is avoiding the fogginess of the crystal that sometimes arises due to moisture or oxygen contamination [138]. A detailed study of color centers is reported elsewhere [148].

Linearity of the pulse height response of the gamma detector was checked up to 1332 keV gamma-rays. The calibration curve for a detector fabricated using the grown CsI:Tl crystal is shown in Fig.3.10 and a typical ^{137}Cs gamma spectrum is also depicted in the same figure showing an energy resolution of about 7.5% at 662 keV which is comparable to or better than reported values [143]. Optimization of light collection at the PMT photocathode was necessary to get the best results. To achieve this nearly 10 layers of Teflon that had reflectivity better than 98%, were wrapped around the crystal and optical grease was applied to couple the crystal with the PMT avoiding any trapped air bubbles.

3.2 Growth of CsI:Tl crystals using a modified Bridgman method

In a different approach a modified Bridgman technique has been designed and developed to grow the CsI single crystal of 50 mm diameter and 60 mm length, in a simple and effective manner. In this part of Chapter-3, design and construction of the modified Bridgeman system employed for the crystal growth of Tl doped CsI are elaborated. A specially designed crucible along with the modified furnace was used to grow single crystal of CsI:Tl of 50 mm diameter and 60 mm length. By employing this technique the thermal and mechanical shocks to the crystal were minimized that reduced the day light coloration and enhanced the radiation hardness of grown crystals.

3.2.1 Furnace and crucible design

The furnace employed for the crystal growth consists of four independently controlled resistive heating elements. The top isothermal zone consisting two heating elements is separated from the bottom isothermal zone by a 50 mm thick baffle (adiabatic zone). Fig.3.11 shows the schematic diagram of the furnace along with the photographs of the complete crystal growth system. The furnace can be rotated along a horizontal axis passing through middle of the furnace. There is also a provision for locking the crucible while rotating the furnace if necessary. A maximum 20^{o}C/cm temperature gradient was achieved in the adiabatic zone. The axial and radial temperature profiles of the furnace are shown in Fig.3.12.

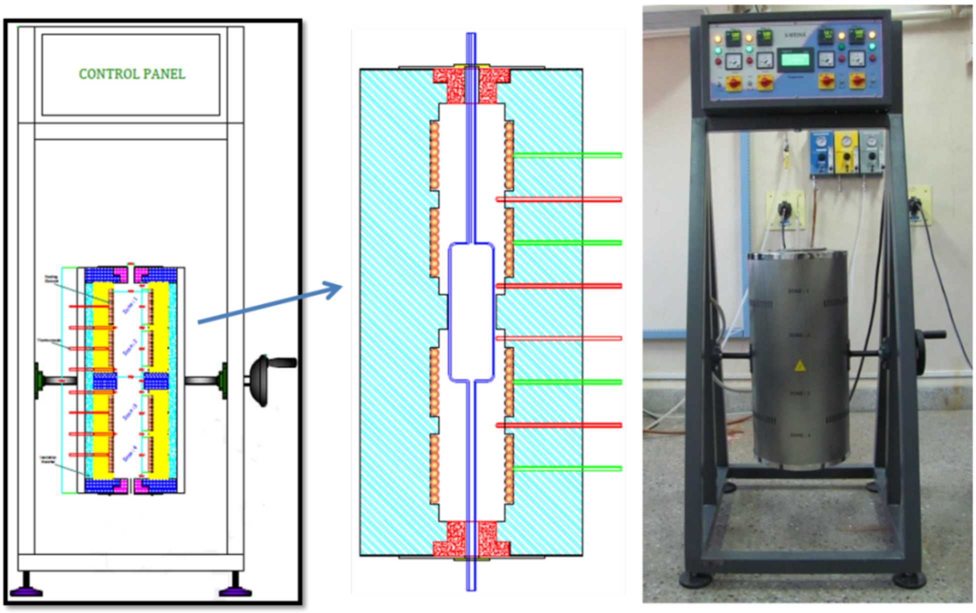

(a) (b) (c)

Figure 3.11: Modified Bridgman furnace diagram (a) schematic of the crystal growth system, (b) enlarge view of furnace along with the control and monitoring thermocouple positions (green coloured ones are the controlling and the red coloured are the monitoring thermocouples) and (c) photograph of the fabricated crystal growth system.

The crucible has been specially designed to be used with the modified Bridgman furnace. It consists of two parts of approximately equal lengths (as shown in Fig.3.13). The lower part has a slightly less diameter (ID: 55 mm) than the upper part (ID: 60 mm). The crystal grows in the lower part of the crucible while after the growth the crystal is retrieved in the upper part by a definite process involving the rotation of the furnace along with the crucible. The detailed description of the growth is given in next section.

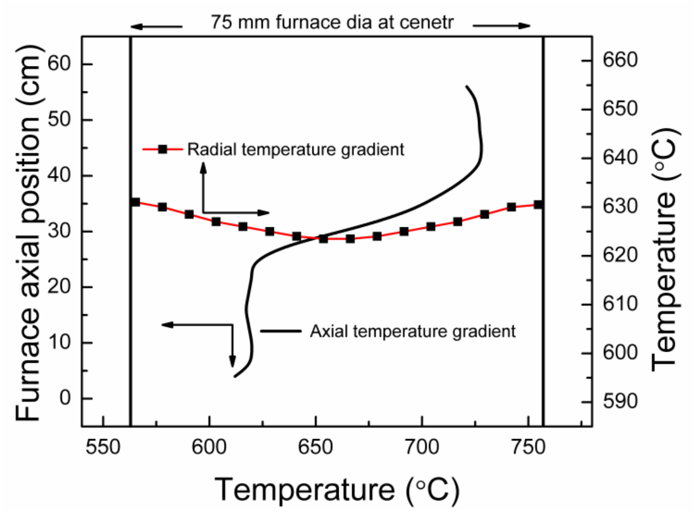

Figure 3.12: Radial and axial temperature gradients of the crystal growth furnace.

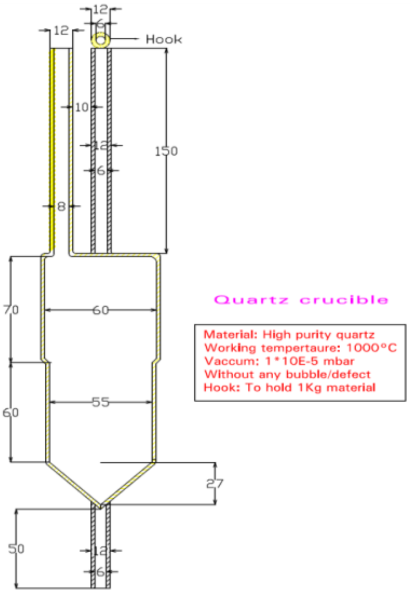

Figure 3.13: AutoCAD drawing of the crucible used in the crystal growth in the modified Bridgman furnace.

3.2.2 Crystal growth

The material was dehydrated following the same procedure as described in section 3.1.2. The silica crucible containing the material (discussed in previous section) is kept in the upper zone of the furnace for complete melting. The temperatures of all the zones are raised in such a manner that the temperature of the upper zone is about 50°C above the melting temperature (MP) of the material while the lower zone temperature is about 50°C lower than the MP (Fig.3.14-1). Once the material inside the crucible melts completely it is allowed to thermalize for 4 h. The crucible is then lowered at a typical rate of about 0.5 mm/h to the bottom zone of the furnace through the temperature gradient (adiabatic zone) for a complete solidification of the melt into single crystal (Fig.3.14-2).

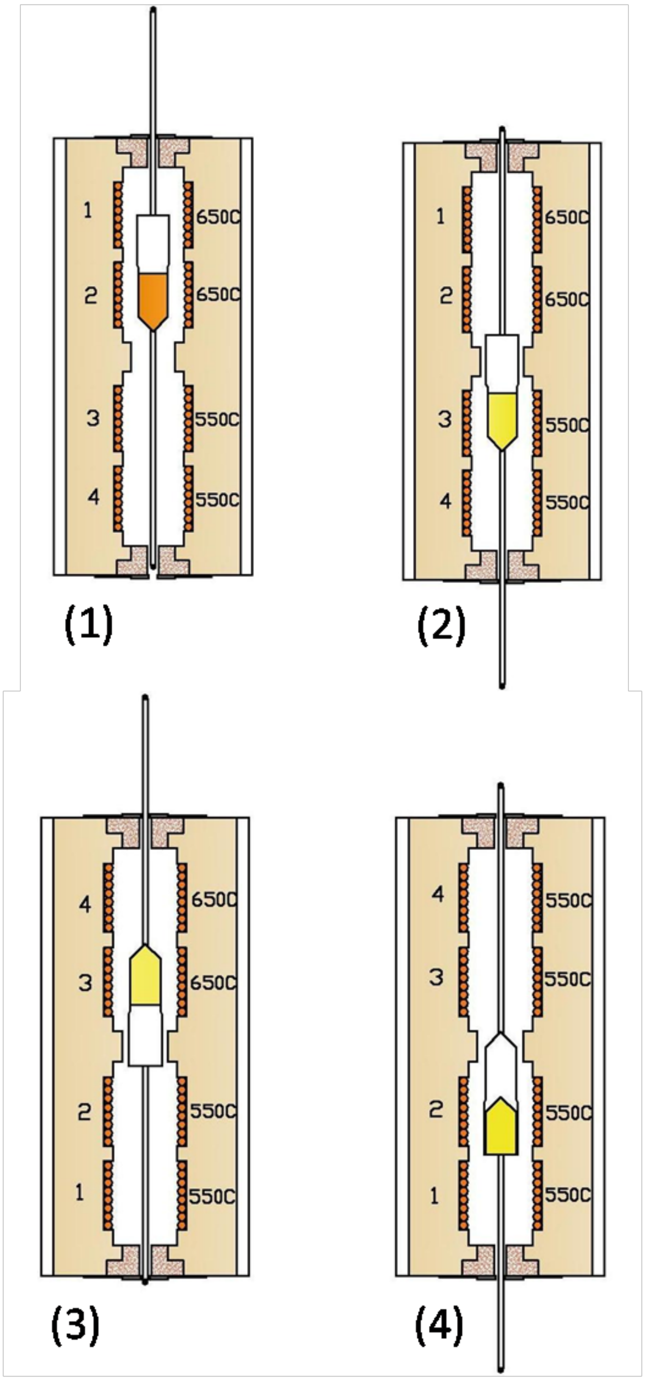

Figure 3.14: The schematic diagram of the complete growth process of the CsI:Tl single crystal in the modified Bridgman furnace. (1) Loading of the crucible and melting of the material, (2) Lowering of the crucible to lower zone and solidification, (3) Locking of the crucible in the furnace and rotation by 180 degree and (4) retrieval of the crystal .

After complete solidification of melt into single crystal the crucible is locked inside the furnace using a locking mechanism and the furnace together with the crucible is inverted (rotated through 180º) (Fig.3.14-3). Now the temperature of the zone 3 and 4 containing the grown crystal is raised so that the temperature of the zone containing the grown crystal becomes slightly higher than the MP of the material. As the temperature of the outer part of the crystal increases above its MP it starts melting from the outer portion and leaves the walls of the crucible. The grown crystal slides down to the lower zone of the crucible that has a slightly larger diameter. Temperatures of the all the zones are then lowered quickly to the same temperature (MP-50°C) to achieve a uniform temperature in the furnace (Fig.3.14-4). The crystal is annealed at this temperature for 4 h. Finally the furnace is cooled down to room temperature at a uniform rate of 30ºC/h. Afterwards the silica glass crucible is cut open to retrieve the grown crystal.

3.2.3 Optical and scintillation characterization of grown crystals

Transmission spectrum was recorded in the wavelength range 200-1100 nm employing a double beam photo-spectrometer Chemeto 2500. X-ray induced emission spectra were measured using an in-house built set-up. The X-ray source was an X-ray tube with a Cu target. The accelerating voltage and tube current were set at 40 kV and 30 mA, respectively. An Avantes make (model: 3648) spectrograph was used to measure the emission spectra.

To test the scintillation properties detector element of 18 mm x 18 mm x 18 mm were fabricated by processing of crystal ingot (50 mm diameter and 50 mm length). About 5 to 6 layers of 0.1 mm thick Teflon tape were used as reflectors. Silica based optical grease was used for the optical coupling. The fabricated detector element were tested for scintillation performance using to different readouts, namely, (i) P-I-N photo-diode (Hamamatsu: S3204-8 18 mm x18 mm active area) and (ii) Photomultiplier tube (Hamamatsu: R6095 25 mm diameter). In case of PIN photodiode 10-12 μs pulse shaping was used while in case of PMT read out it was kept 3-4 μs. To check the performance of the scintillator with the standard 50 mm diameter head-on PMT (Hamamatsu: R1306), a scintillator detector element of 45 mm diameter and 45 mm length was fabricated from the crystal ingot and was mounted on the PMT. Reflector and mounting arrangement were similar to the earlier detector. Different gamma sources (^{60}Co, ^{57}Co, ^{137}Cs, ^{134}Cs, ^{22}Na) were used to check the energy dependence of the scintillation characteristics. To get photo-peak at lower energy (10-100 keV) ^{57}Co was used in different metal wrapping like Mo, W, Pb etc. An Am-Pu alpha source was used to test the pulse shape discrimination characteristic of the CsI:Tl detector.

3.2.4 Discussion

The main advantage of the present method over the conventionally used Bridgman system was that the grown crystal was subjected to minimum thermal and mechanical shocks during the retrieval of the crystal. After the growth, crystal could be annealed for various durations to improve the properties without any contamination or stress as in this condition crystal is free from the crucible walls. A typical photograph of grown crystal along with the processed scintillator is shown in Fig.3.15. Absorption spectra of grown crystals containing varying amounts of thallium (0, 0.001, 0.01, 0.05, 0.2 mol%) were recorded and are shown in Fig.3.16. Gradual development of Tl related absorption can be seen in the graph indicating the increasing Tl concentration in the crystal. All the crystals show more than 80% transmission in the 350-1100 nm wavelength range indicating excellent optical quality of the grown crystals. The cutoff wavelength for un-doped crystals was about 240 nm. The band structure calculation of the CsI

(Fig.3.17) shows a direct band gap of 4 eV, while the experimental value was about 5.2 eV. The difference in observed and calculated value is acceptable as the full potential LAWP method used to calculate the band structure is known to underestimate the band gap. The calculation was done using the EXCITING code [127].

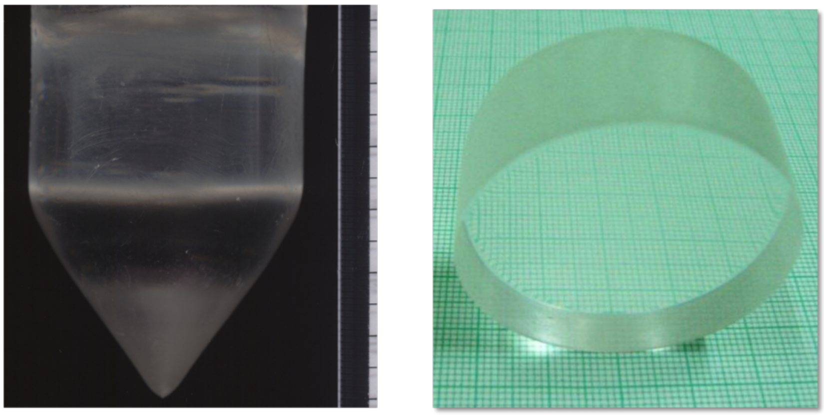

Crystal Ingot Processed scintillator

Figure 3.15: Photograph of crystal ingot grown using the modified Bridgman technique and processed scintillator.

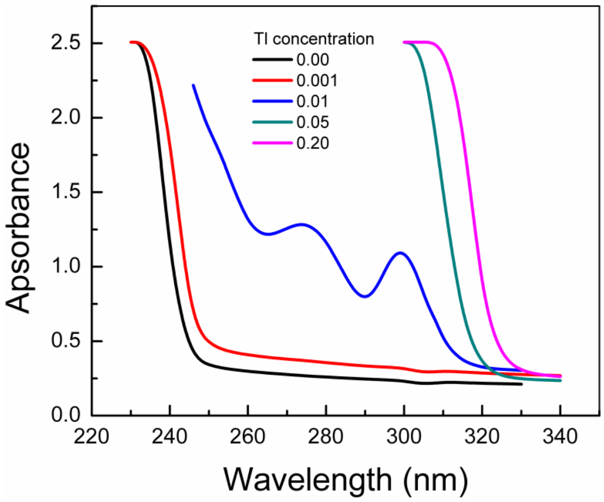

Figure 3.16: Absorption spectra of CsI crystal as a function of Tl concentration.

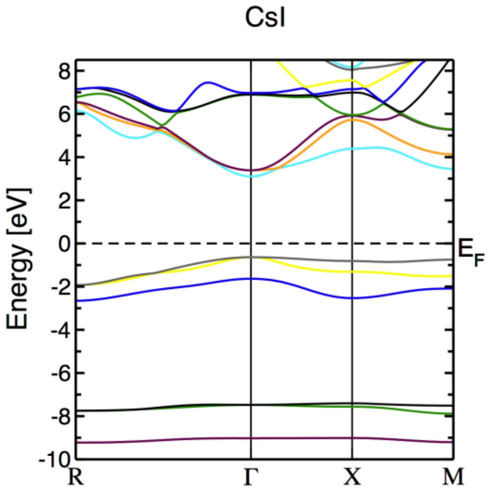

Figure 3.17: Electronic band structure of CsI calculated using Exciting code.

The radio luminescence (RL) spectra were recorded for all the samples and are shown in Fig.3.18. The characteristic luminescence of Tl centered at 545 nm evolves with increasing Tl concentration in the CsI crystal. The luminescence of undoped CsI centered at 310 nm indicates the high purity of the initial material and excellent growth (no oxygen contamination).

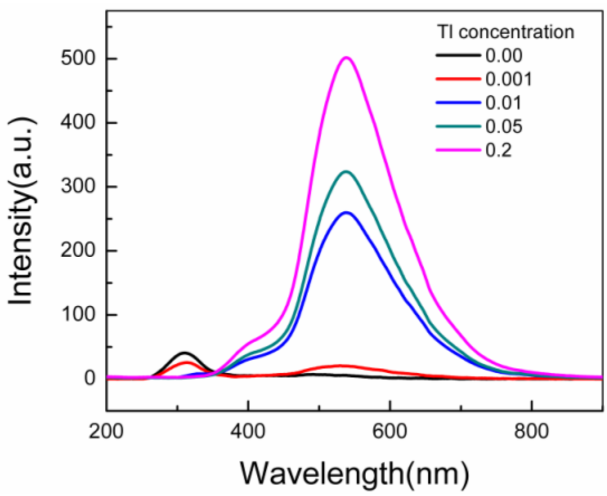

Figure 3.18: Radio-luminescence spectra of Tl doped CsI as a function of Tl concentration.

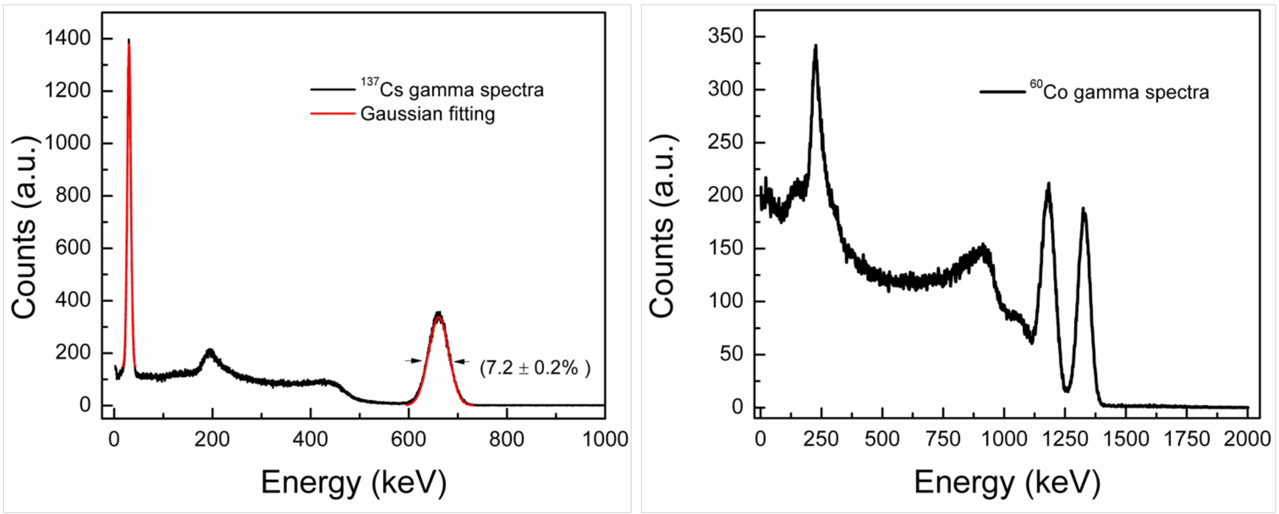

Figure 3.19: Typical gamma spectra of ^{137}Cs and ^{60}Co as recorded using a 18x18x18 mm^{3} cube prepared from the CsI:Tl crystal and coupled to a PMT.

Typical gamma spectra recorded using the CsI:TL (18x18x18 mm^{3}) coupled to a PMT detector for different gamma sources (^{137}Cs and ^{60}Co) are shown in Fig.3.19. The fabricated detectors show an energy resolution of 7.0 ±0.2% at 662 keV. It is well established that the non-proportionality in the photon-yield as a function of gamma energy is the main reason that inorganic scintillators could not achieve energy resolutions theoretically predicted based on their light output. The non-proportionality depends on many factors. One of these factors is growth condition and distribution of dopant throughout the crystal. To see the effect of this growth technique on the non-proportionality in CsI:Tl in response to photon energy was also calculated and is shown in Fig.3.20. The observed non-proportionality is same as reported in the literature [149]. This fact shows that the adopted growth conditions are favorable to grow the crystals for detector application. Linearity of the pulse height response of the gamma detector was checked up to 1332 keV gamma-rays. The detector performance of 45 mm diameter and 45 length scintillator was tested using a 50 mm diameter PMT. The typical gamma spectra are shown in Fig.3.21. The energy resolution at 662 keV was found to be 6.7 ±0.2% that is remarkable for a CsI detector of this size. The resolution obtained from this detector was comparable to the resolution quoted for commercially available NaI based detectors despite the mismatch of the PMT response with the emission profile of CsI:Tl, again suggesting the good quality of the grown crystals.

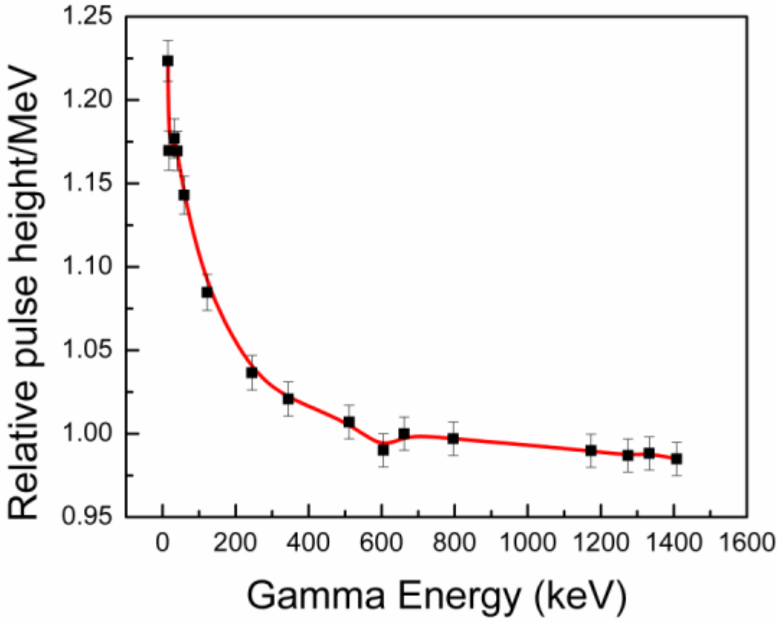

Figure 3.20: Non proportionality response of Tl doped CsI as a function of photon energy.

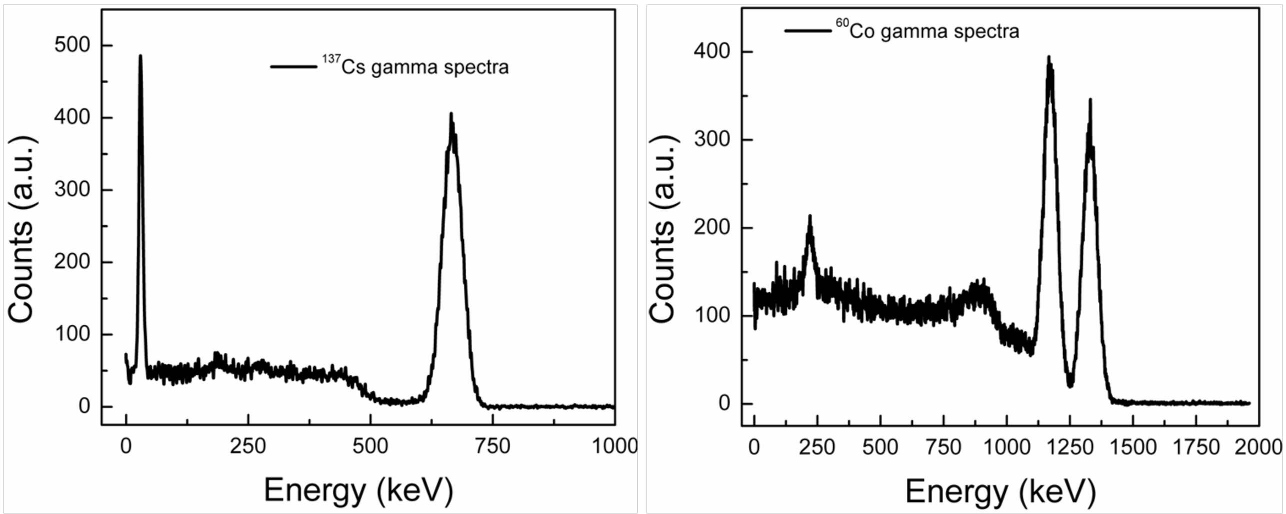

Figure 3.21: Typical gamma spectra of ^{137}Cs and ^{60}Co as recorded by CsI:Tl crystal (45 mm ϕ x 45 mm L) coupled to a PMT.

As the emission at 550 nm from the CsI:Tl scintillator matches well with the response of photodiodes, a combination of CsI:Tl and P-I-N photodiode is expected to have sevral advantages over the conventionally used PMT based detectors. Few advantages to be mentioned are low voltage requirement, insensitivity to magnetic fields, ruggedness, compactness, low cost, etc. The 18x18x18 mm^3 detector element was coupled to the photodiode of same active area. As in this case the time response of detector also depends upon the junction capacitance of the photodiode, the time integration time was taken about 12 μs. The typical gamma spectrum recorded using the detector is shown in Fig.3.22. The energy resolution calculated at 662 keV was 8±0.2% while at 1332 keV it was 5±0.2%. Though, in this case, the energy resolution at higher energies (>1 MeV) was comparable to the resolution obtained from the PMT based detector, at lower energies the resolution was poor. The main reason behind this is that, as the P-I-N photodiode has no gain the electronic noise generated in various components like pre-amplifier, connecting pins/wire etc becames dominant at lower energies. This is the reason that to detect gamma energy below 100 keV special low noise electronics is required [150].

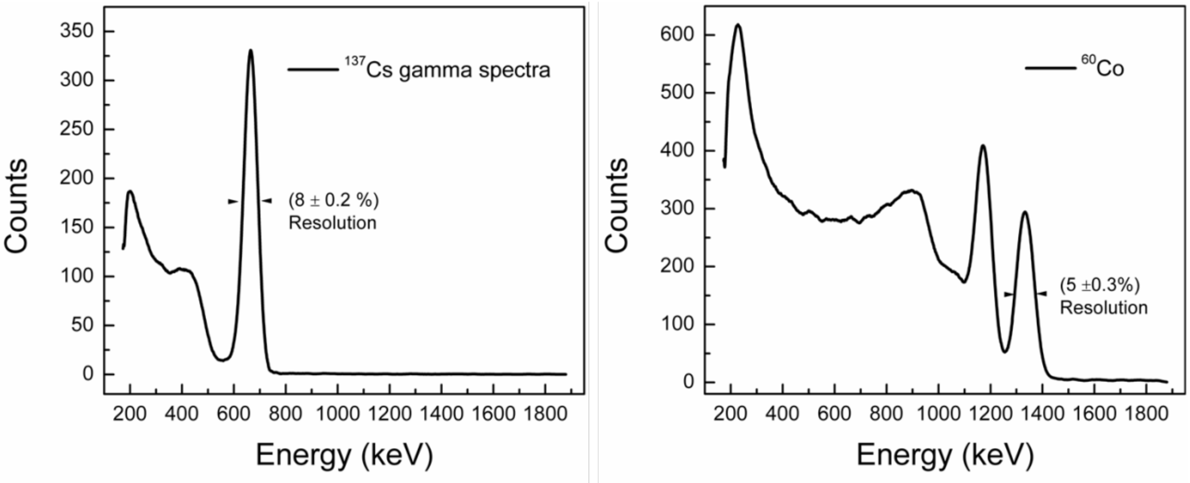

Figure 3.22: Typical gamma spectra of ^{137}Cs and ^{60}Co as recorded by 18x18x18 mm^3 CsI:Tl coupled to a P-I-N photodiode.

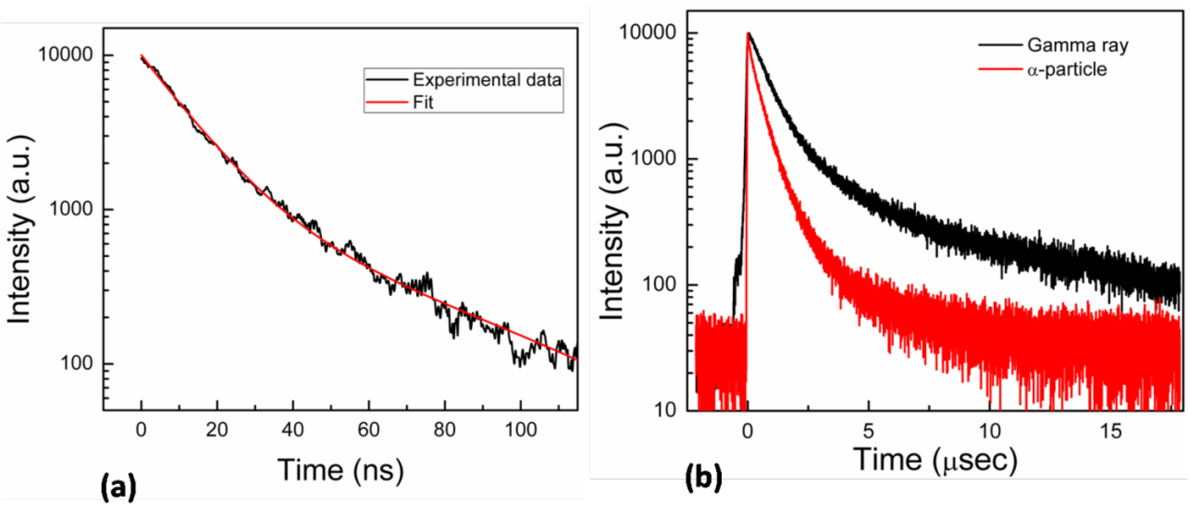

Figure 3.23: The decay profiles of (a) Undoped CsI for gamma and (b) CsI:Tl for gamma and alpha particle.

The scintillation decay profiles of un-doped and doped CsI crystals were calculated by analyzing the pulse shape of PMT output read by an oscilloscope (Tectronix: MDO3102) and is shown in Fig.3.23. The values of decay time constant are given in Table-3.1. The un-doped CsI crystal has two decay components with average decay constant of 13 ± 1 ns that is as per the reported values in the literature [151, 152]. The decay profiles of Tl doped CsI were recorded for gamma as well as alpha particle response. For gamma-rays the CsI:Tl crystal shows an average decay constant of 1200 ± 50 ns while it was found to be 550 ±25 ns for alpha particles. This shows an excellent pulse shape discrimination characteristic of CsI:Tl.

Table-3.1: The scintillation decay constant of undoped and Tl doped CsI.

Scintillator	Scintillation decay time	
	Gamma-rays	Alpha particles
CsI	12 ns (95%), 50 ns (5%)	-
CsI:Tl	800 ns (90%), 4400 ns (10%)	115 ns (20%), 550 ns (75%), 2000 ns (5%)

3.3 Growth of NaI:Tl crystals using a modified Bridgman method

Though this crystal growth system was designed for the growth of CsI:Tl it can be used to grow any halide crystals having melting point up to 900°C. To demonstrate the versatility of the system single crystals of NaI:Tl were grown and characterized. All the growth parameters were same as for the CsI except that the material was handled in a glove box with controlled moisture and oxygen content. The material was dehydrated following the same procedure as described in the section 3.1.2. The TlI doping level was kept at 0.1-0.12 mol%. After the growth the crystal is annealed at 600°C for 4 h and finally the furnace was cooled down to room temperature at a uniform rate of 10-20ºC/h. Afterwards the silica crucible is cut open to retrieve the grown crystal. The photograph of as grown crystal is shown in Fig.3.24.

The scintillator performance was checked by processing a detector element of 45 mm length and 45 mm diameter from the crystal ingot. All the processing was done inside the glove box to avoid any moisture contamination. The scintillator was coupled with a 50 mm diameter PMT (ADIT: B51D01S) and a gamma spectrometer (1k MCA, 1 μs shaping time) was used for the pulse height analysis. The detector was hermitically sealed prior to testing. A typical gamma spectrum recorded using the system is shown in Fig.3.25. The typical resolution calculated at 662 keV was 6.8±0.2% which is at par with the commercially sold NaI detectors [27,28].

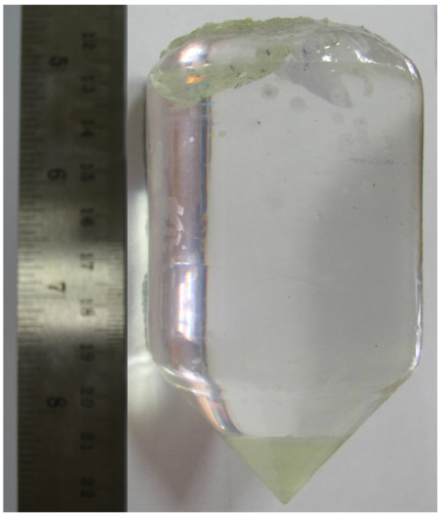

Figure 3.24: Photograph of as-grown Tl doped NaI crystal.

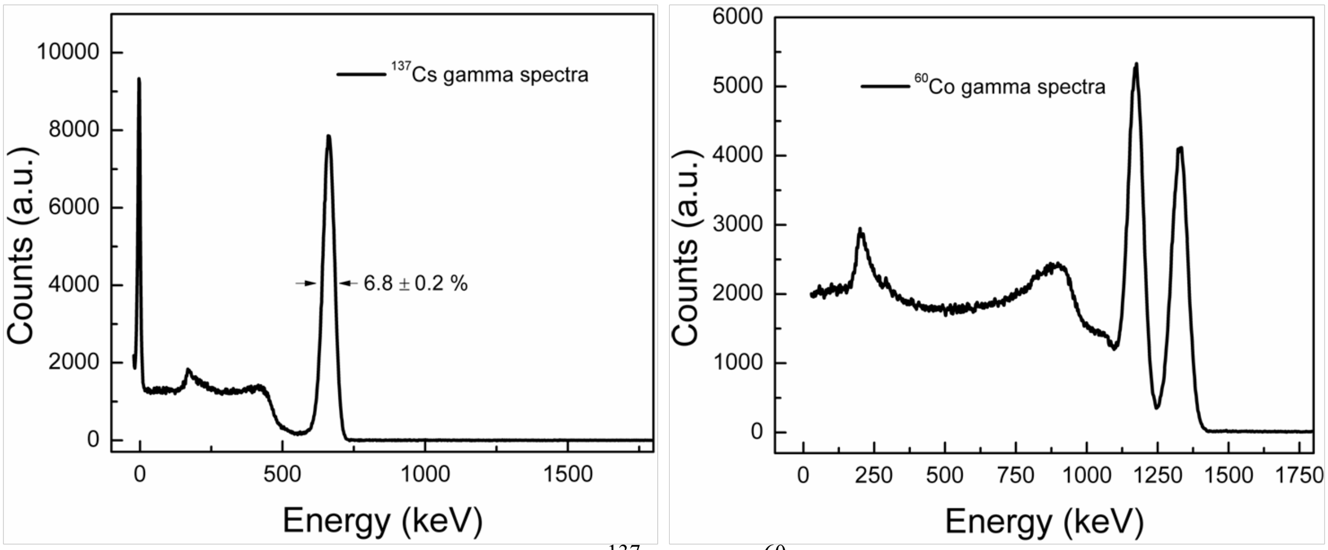

Figure 3.25: Typical gamma spectra of ^{137}Cs and ^{60}Co recorded using a NaI:Tl crystal scintillator (45 mm ϕ x 45 mm L) coupled to a PMT.

3.4 Conclusions

During the course of this thesis two different approaches were adopted for the growth of alkali halide crystals of 50 mm diameter and 60 mm length in general and CsI:Tl in particular. In the first approach Tl doped CsI crystals were grown in the carbon coated fused silica crucibles using a gradient freeze technique. No adverse effect of carbon is seen and problem with sticking of CsI crystals with crucible wall was successfully solved. The quality of the crystal grown using the present methodology was better than the conventionally grown crystals. After-glow and daylight coloration are mostly related to defects generated during the crystal growth process. These defects became mobile above 400°C and can be eliminated if the crystal is annealed for a sufficient time. It is beneficial to anneal the crystal immediately after the growth without opening the silica ampoule to avoid deterioration of the transparency. With this approach crystal of 40 mm diameter and 50 mm length could be grown successfully.

In the second approach a modified Bridgman crystal growth furnace has been designed for the crystal growth. The system was modified to retrieve the crystal after the growth without cracking the crucible and the crystal. The main advantage of the process was that the grown crystal was subjected to minimum thermal and mechanical shocks. After the growth, crystal could be annealed for varying durations and without any contamination or stress, as in this case crystal is not in contact with the crucible walls. The grown crystal showed the best scintillation properties possible for the materials that proved the efficacy of the crystal growth process. With this process single crystals of alkali halides of 50 mm diameter and 60-70 mm length could be grown with almost 100% yield. This low cost method can be used for the industrial production of medium size (50 mm diameter and 70 mm length) alkali halides and the technology is being transferred to industry.

CHAPTER 4

GROWTH OF SINGLE CRYSTAL OF NaBi(WO$_4$)$_2$ AND NaGd(WO$_4$)$_2$ AND STUDY OF THE EFFECT OF OXYGEN STOICIOMETRY ON THEIR LUMINESCENCE PROPERTIES

In this chapter the growth of single crystals of NaBi(WO$_4$)$_2$ and NaGd(WO$_4$)$_2$ has been discussed along with the effect of oxygen environment around W on the luminescence and optical properties of these crystals.

4.1 Growth and annealing studies on NaBi(WO$_4$)$_2$ single crystals

4.1.1 Introduction

Single crystals of NaBi(WO$_4$)$_2$ (NBW) with high density and radiation hardness is one of the promising materials that can be used as a Cherenkov detector for both luminosity and calorimetric measurements under higher charge backgrounds that are encountered in the high energy physics experiments [18, 20, 154, 155]. From the chemical point of view NBW may be regarded as related to PbWO$_4$ (PWO) with the replacement of Pb by a 1:1 mixture of Bi and Na. The NBW structure belongs to I4$_1$/a space group with lattice parameter a= 5.28 Å and c= 11.50 Å [156]. While literature for PWO is widely available [62, 157-159], optical and luminescent properties of NBW are not studied in details. Further, it was reported that X-ray luminescence spectrum of NBW has a maxima at about 520 nm and the luminescence intensity is about 5% that of Bi$_4$Ge$_3$O$_{12}$ (BGO) [54, 160]. However there is no report on photoconductivity properties of this material though two decades back in 90’s, Nitsch et. al. have mentioned the necessity of these measurements to explain different decay kinetics in these crystals [161].

For application of this material in high energy physics experiments (CERN like conditions) thorough characterization of $NaBi(WO_4)_2$ single crystal will be necessary. In this work we investigated the spectral dependence of photoconductivity (PC) along with photoluminescence (PL) of these crystals. This simultaneous evaluation is highly desirable for better understanding of the excitation mechanism and relaxation of excited states. In addition, the influence of defect structures has been investigated by carrying out PL on high temperature annealed crystals. The studies on effect of annealing would also help to improve the radiation hardness of these crystals.

4.1.2 Experimental

(i) Crystal growth: Un-doped NBW crystals (Fig.4.1) have been grown using the Czochralski technique in air ambient [162]. The growth was carried out employing automatic diameter controlled Cyberstar crystal pullers, having a 50 kW induction heater. The system employed crystal weighing technique to control the diameter where the difference between actual and set values of mass growth rates was used as feedback for adjusting the percentage of power fed to the inductively coupled crucible. The value of axial temperature gradients just above the melt (within 5 mm) was about 60°C/cm. A uniform pull rate of 2 mm/h and a rotation rate of 15-20 rpm was employed to grow 60 mm long crystals of 30 mm diameter from the melt contained in a 75 mm diameter platinum crucible of 70 mm height. About 500 g of charge was used in each growth experiment. Uniform post growth cooling rate of 30°C/h was employed in regular crystal growth experiments. Few growth parameters employed in particular growth experiment are listed in Table-4.1.

Figure 4.1: Photograph of a typical $NaBi(WO_4)_2$ single crystal ingot.

Table-4.1: Parameters used to grow $NaBi(WO_4)_2$ single crystals.

Parameters	Value
Solid Density	7.6
Melting	930°C
Growth Method	Czochralski technique
Ambient	Air
Pull rate	1-2 mm/h
Rotation	15 rpm
gradient	60°C/cm
cooling	30 °C/h

(ii) Optical and luminescence experiments: For performing optical transmission, reflection and luminescence measurements, the opposite faces of the crystal slices were optically polished. Optical transmission spectra of the samples were recorded over the wavelength range of 200–800 nm by a PC-based spectrophotometer (Model: 8500 Techcomp). The reflection spectra, over the wavelength range of 200–500 nm, were recorded by a Shimadzu spectrophotometer Model 3100. The PL studies were performed over a wavelength range from 300 nm to 800 nm and in a temperature range of 77–300K by employing a fluorescence spectrometer (Edinburg Model-FLP920) as described in the experimental techniques, Chapter-2. The recorded luminescence spectra were corrected for the spectral sensitivity function of the instrument.

(iii) Photoconductivity and annealing study: The spectral dependence of photoconductivity was measured at an applied field of 500 V/cm. The field was applied using thermally deposited gold electrodes on one side of the crystal. A Lock-in amplifier was used to measure photocurrent across a load resistance of 1MΩ. The output signal as a function of excitation wavelength can be measured with the help of V/F converter and plotted on a PC. The schematic of the setup is shown in Fig.4.2. For annealing studies two discs cut from a crystal ingot were used. One disc was annealed in air at 700°C for 6 h. The other disc was annealed at 700°C under high vacuum conditions (10^{-6} mbar) for about 1h to avoid surface degradations.

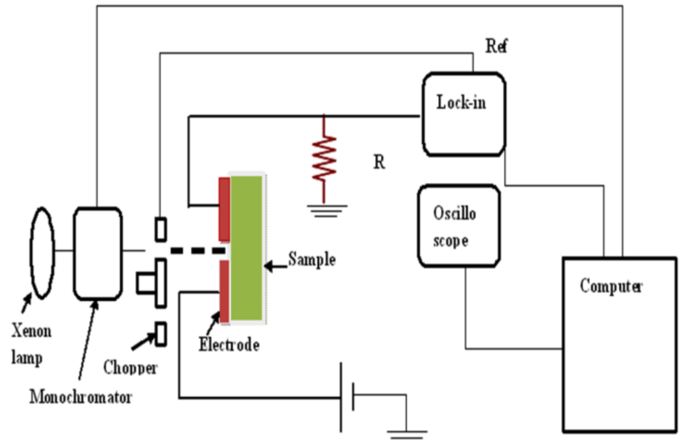

Figure 4.2: Schematic of Photo-conductivity setup.

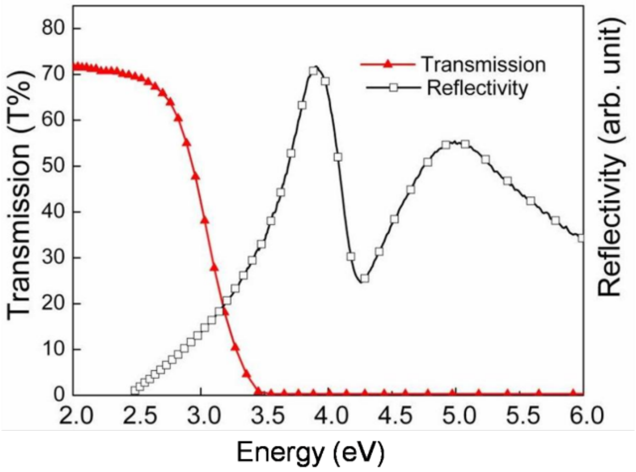

Figure 4.3: Spectral dependence of transmission and reflectivity of as-grown $NaBi(WO_4)_2$ crystal.

4.1.3 Result and discussion

Optical transmission and reflection spectra recorded for NBW crystal are shown in Fig.4.3. Fig. 4.4 (a), (c), and (e) show excitation and emission spectra recorded at 77 K for as-grown, oxygen annealed and vacuum annealed samples respectively. As-grown crystal shows an excitation band peak at 322 nm with a shoulder at 280 nm for a broad emission band peaking at ~495 nm. A large stoke shift of ~ 10854 cm^{-1} for the emission band was found to be similar to other molybdate and tungstates crystals and therefore indicates excitation and emissions to originate from the singlet–triplet transitions [$^3T_1$ – $^1A_1$] [158]. It is an expected result as it has been reported that the electronic and optical properties of NBW and other Scheelite crystals, particularly PWO are found to have striking similarities as the 3*s* states of Na in the NBW lie fairly above the bottom of the conduction band. Anisotropy of emission band and presence of two excitation band indicates the presence of more than one emission processes. The presence of two emission processes has been also reported by Nitsch et al [161], although Volkov et al have reported single excitation and emission band peaking at 335 and 505 nm respectively [160]. In the case of annealed crystal two emission bands peaking at 460 nm and 510 nm could be well separated for photo excitation at different energies. The excitation band at 280 nm was found to be suppressed significantly in the case of crystal annealed in air. Excitation peak at a higher wavelength (322 nm) can be ascribed to excitons which is independent of annealing while the lower wavelength (higher energy) excitation at 280 nm could be interband transitions between O *p* and W *d* states. The optically excited excitons may be created at Bi^{3+} ions and can move freely through the crystal and then get self-trapped on $(WO_4)^{2-}$ ions by inducing the Jahn–Teller distortion of the tetrahedral oxy-anion molecules [163]. The annealing changes the energy structure of regular WO_4 complex due to defects in anion sub-lattices including interstitial oxygen and oxygen vacancies which subsequently influence the higher energy excitation as observed in the excitation spectra measured for the annealed samples.

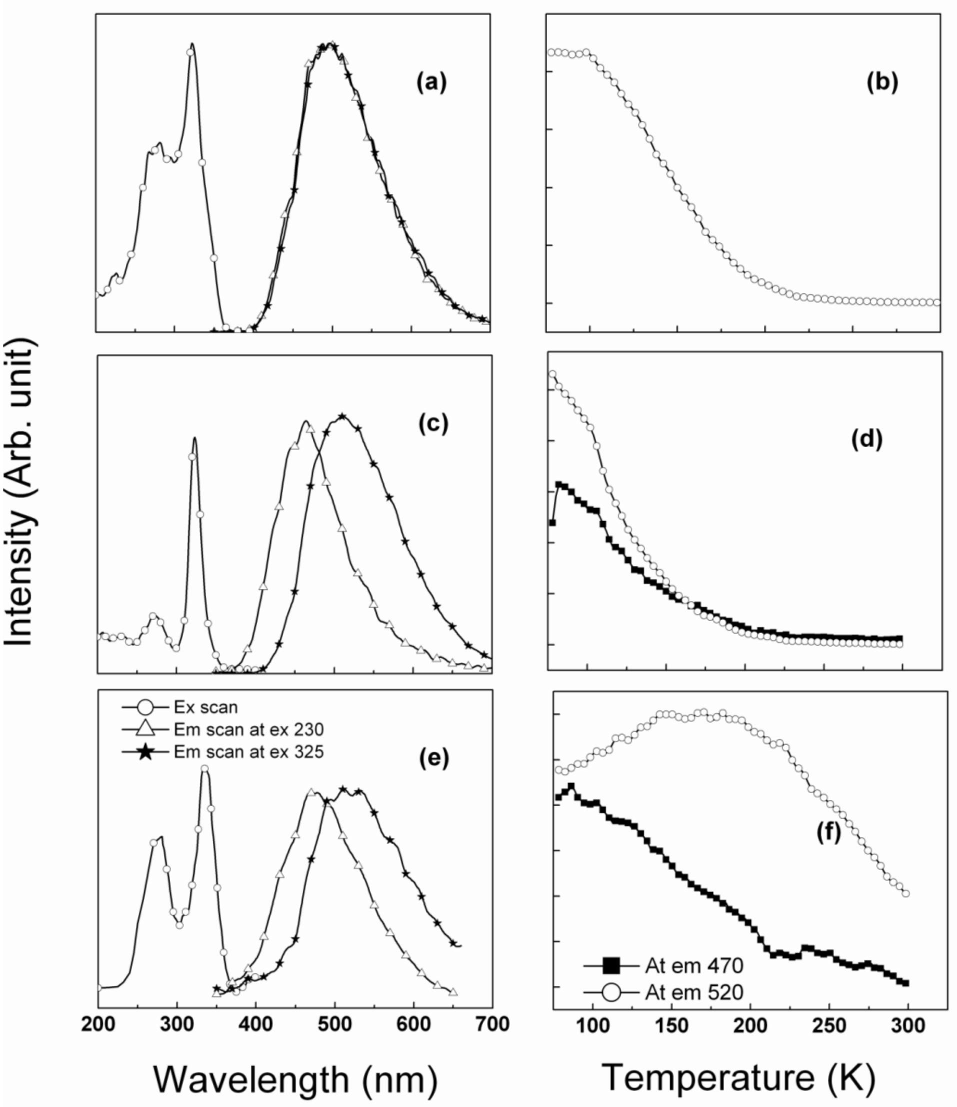

Figure 4.4: Excitation, emission and temperature dependence of emission for $NaBi(WO_4)_2$ crystal (a) and (b) as-grown, (c) and (d) annealed in air, and (e) and (f) annealed in vacuum.

The temperature dependence of emission is shown in Fig.4.4 (b), (d) and (f). In as-grown crystals the PL intensity becomes half at ~145 K and completely quenched after 200K. The thermal activation energy for the quenching was calculated from a Mott-Seitz dependence of photoluminescence as given in the following equation,

$$\eta = \frac{1}{1+Aexp\left(\frac{-\Delta E}{kT}\right)} \tag{4.1}$$

The ΔE is the thermal activation energy for quenching of emission and presents the height of the crossing point where parabola for excited state crosses that of the ground state and hence emission quenches through the non-radiative transitions. This energy for 495 nm emission was calculated to be about 160 meV in the case of NBW crystals which is smaller than that for PWO (~200 meV) [164]. The observed temperature dependence of PL is also consistent with the reported results for other AWO_4-type crystals [61, 165]. The anisotropy in emission band and temperature dependence of emission also indicates the presence of more than one excited states. Therefore PL intensity quenches with increasing the temperature as non-radiative transitions increase. Thermal quenching profile was also observed to be changed for vacuum annealed samples and even at room temperature, PL could be observed for these samples. Present studies suggest a different thermal quenching of PL due to different growth conditions compared to those reported earlier in the literature for this class of materials. Consequently the crystals having desired properties can be grown in controlled ambient that could affect its luminescence characteristics in a desired manner. The emission scans recorded at different temperature are shown in Fig. 4.5 for the grown crystal. The emission is found to shift towards higher wavelengths (red shift) with increasing temperature. Similar shift in the emission peak towards higher wavelength is also observed on annealing in air and vacuum as shown in Fig. 4.6. This red shift in emission with temperature can be ascribed to increase in the absorption in urbach tail that suppresses the excitation in higher wavelength excitation band and simultaneous quenching of both emissions. Dilation of lattice and electron lattice interaction increases with temperature which consequently leads to red shift and thermal quenching of luminescence.

This mechanism of PL has also been supported by our electronic band structure calculations as shown in Fig.4.7 [166]. It was observed that the valence band (VB) is mainly formed by non-bonding states of the oxygen *p* orbital, with a very little contribution coming from the tungsten *d* orbital. The conduction band (CB) is mainly formed from W *d* states with a similar amount of contributions coming from the *p* states of bismuth and oxygen. But the presence of Bi states in VB and CB indicates that the excitons are created at Bi ions and then trapped at the $(WO_4)^{2-}$ complex.

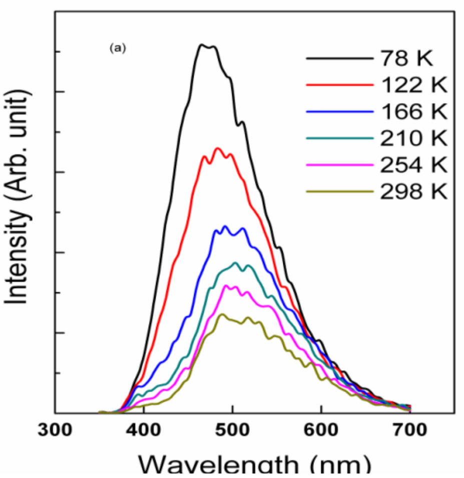

Figure 4.5: Effect of temperature on emission of as-grown $NaBi(WO_4)_2$ crystal.

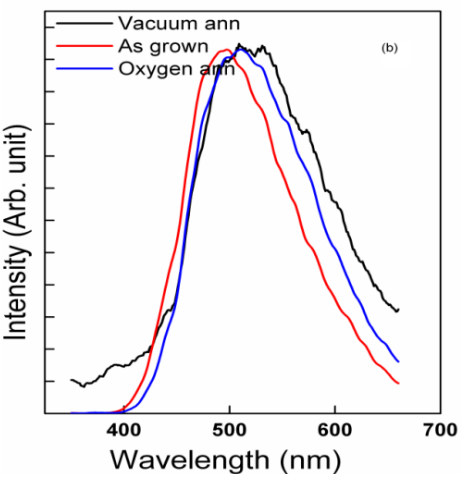

Figure 4.6: Effect of after growth annealing on emission of as-grown $NaBi(WO_4)_2$ crystal.

The role of these excitons and localization of charge carriers can be understood by comparing the spectral dependence of excitation, photoconductivity, transmission and reflectivity of the as-grown NBW crystal as shown in Fig.4.8 and Fig.4.3. The dependence of measured reflectivity matches well with that of calculated from electronic band structure calculation [166]. Only intrinsic photoconductivity could be observed in these crystals. Though the band structure of NBW is similar to that of Mono tungstates like PWO, but the photoconductivity lies in the excitation region of NBW crystals where excitonic transition is involved. The photoconductivity observed in the excitation region indicates that excitation leads to free charge carriers. These processes correspond to delocalized transitions unlike localized transitions in the case of PWO. Therefore involvement of mobile charge carriers in the luminescence and excitation processes may be one of the reasons for lesser activation energy of thermal quenching of photoluminescence observed in the NBW crystals as compare to that of PWO crystals.

The effect of annealing on PC shown in Fig.4.9 also shows a lower threshold value due to the dissociation of excitons at defects created in the anion sub-lattice. The appearance of PC below absorption edge may be corresponding to the absorption band of O^- centers. According to our studies a total of five types of defect centers were identified in the annealed samples of NBW [167]. In contrast to these results, Volkov et al. have observed no damage or coloration in the crystals after annealing in air [54]. Difference in the effect of annealing and PL results can be attributed to the different type of defect centers present in the grown crystals as Volkov et al. have used different starting charge to grow the crystal. For better understanding and direct observation of these defects, other experiments viz. EXAFS, ESR and ENDOR are required and hence planned for future work.

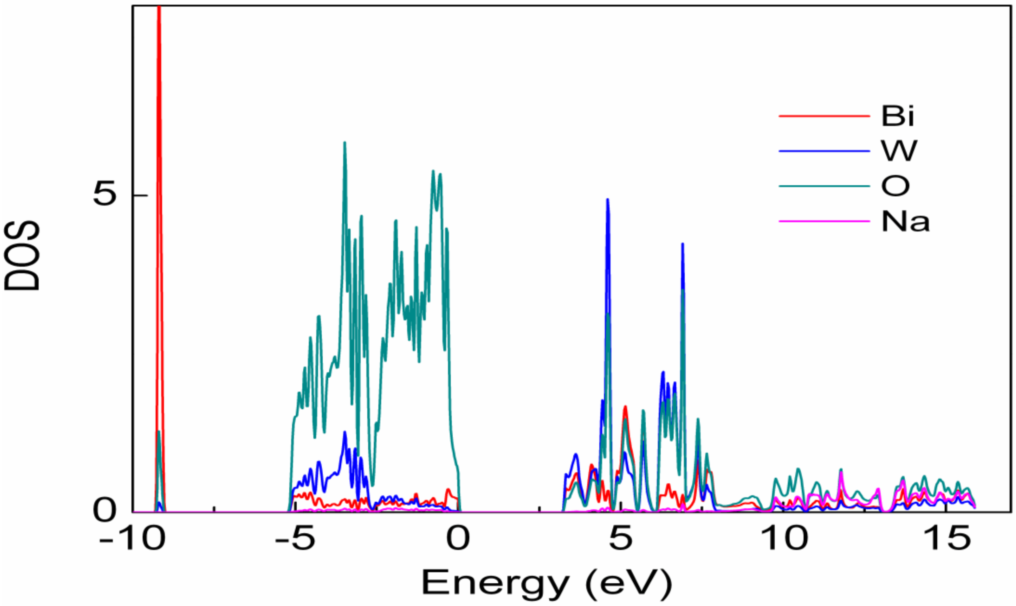

Figure 4.7: Partial density of states of constituent atoms of $NaBi(WO_4)_2$ crystal.

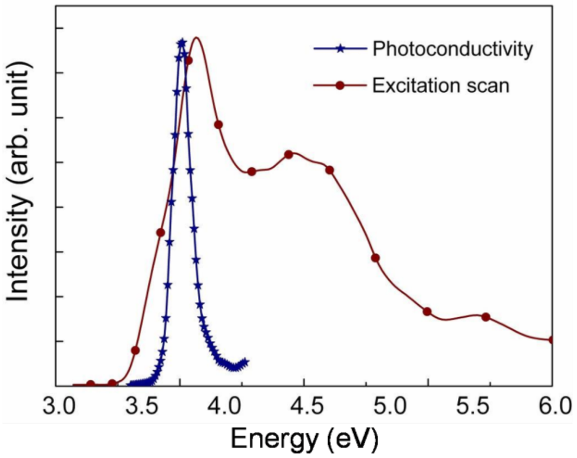

Figure 4.8: Spectral dependence of excitation and photoconductivity of as-grown $NaBi(WO_4)_2$ crystal.

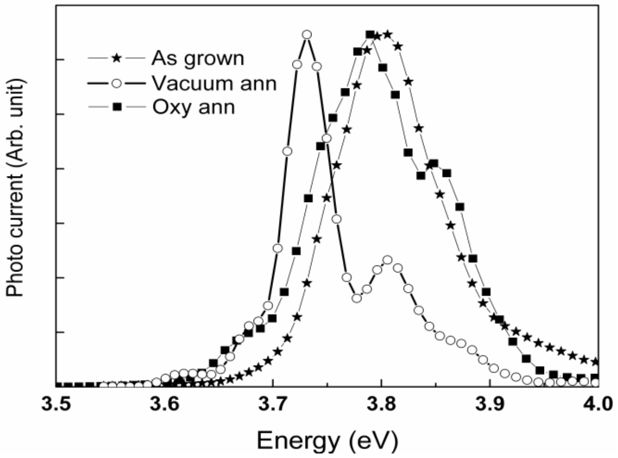

Figure 4.9: Effect of annealing on photoconductivity of $NaBi(WO_4)_2$ crystal.

4.2 Effect of growth ambient in luminescence properties of $NaGd(WO_4)_2$ single crystals.

4.2.1 Introduction

Double tungstate (DT) compounds with the general formula $MT(WO_4)_2$, where M is a monovalent alkali cation Li, Na, K etc and T is a trivalent cation Y, Gd, Bi, La etc, exhibit ordered phases with separate sites for M and T cations and disordered phases where M and Tcations are randomly distributed over the same cationic sub-lattice [56]. Single crystals of $NaR(WO_4)_2$ R: Bi, Gd, Y, La etc having high density and radiation hardness are the promising materials that can be used as radiation detector for both luminosity and calorimetric measurements (CERN like conditions). From the chemical point of view these materials may be regarded as related to $CaWO_4$scheelite-type compound with the replacement of Ca by a 1:1 mixture of R and Na. These materials are intrinsic scintillators and WO_4^{2-} group is responsible for the luminescence. We consider a one-electron charge transfer process from the oxygen 2*p* orbital to the 4*d* and 5*d* of the W^{6+}. For the tungsten compounds, the ground state corresponds to the $^1A_1$ level ($4d/5d^0$ $W6^+$ $/2p^6$ O^{2-} state) and the lowest energy excited state results from the splitting of the $^3T_1$ level ($4d/5d^1$ $W^{5+}/2p^5O^-$ state) [59]. Therefore the absorption band is a charge transfer excitation band. As in these materials emission comes from a level associated to an electron transfer mechanism, it is described as charge transfer emission band. The energy difference between the maximum of the emission and excitation band related to the same two levels is called Stokes Shift. This value gives information about the non-radiative contribution to the relaxation processes. Campos et al. [61] and others explained experimentally and theoretically the phenomena responsible for luminescence in $CaMO_4$ (M = W, Mo). Though it is generally accepted fact that blue-green emission comes from the WO_4^{2+}tetrahedra slightly distorted, while the orange comes from a distortion in the long and medium range order related to oxygen vacancies, the influence of the oxygen vacancies is still subject to discussion. The present study aimed to analyze the intrinsic characteristics of the structure and role of oxygen in in the intrinsic luminescence of the $NaGd(WO_4)_2$ (NGW).

The other interesting fact about disordered phases is their suitability as a laser host for tunable laser operation and generation of ultra-short optical pulses. The random distribution of M^{3+} and T^{3+}cations in tetragonal DTs induces locally variable crystal field acting on the active ion that is expressed in the large bandwidths of the spectral lines of the electronic transitions for the rare-earth elements. Concerning their opto-mechanical and spectroscopic properties such disordered crystals occupy an intermediate position between ordered laser hosts and glasses. In this work Yb doped (NGW) has been grown to show the multi-functionality of the material.

4.2.2 Experimental

(i) Material preparation and Crystal growth: Un-doped and Yb^{3+} doped NGW single crystals were grown by the CZ technique using an automatic diameter control crystal growth system (Cyberstar-oxypuller). The starting materials i.e. Gd_2O_3, Yb_2O_3, Na_2CO_3 and WO_3 of >99.99% purity were used for the single crystal growth. A 300 cc high purity platinum crucible was used to contain the melt. The starting materials were mixed in stochiometry and sintered at 750 °C for 24 hours prior to load in the crucible. The melt was kept at 1275°C for 2 h prior to seed for homogenization. The crystal rotation and pulling rates were kept typically at 15-20 rpm and 0.5–1 mm/h, respectively. The seed was a cylinder of NGW with a diameter of 8 mm, and a length of 20 mm oriented along the **c-**axis. A uniform cooling rate of 30 °C/h was applied in each growth experiment. The cylindrical boules obtained had a weight of about 150 g, a diameter of 25 mm, and a length between 45-50mm. Crystals were grown under three different condition; (i) from fresh charge, grown under 90% Ar + 10% O_2 ambient (crystal-I), (ii) from fresh charge, grown in air (crystal-II), and (iii) from left over charge grown in air (crystal-III). One crystal containing 5mol% Yb in melt was also grown by same procedure as crystal-I.

(ii) Structural and optical study: The crystalline structure of NGW has been the subject of several previous studies and it is debated that whether the structure is I-4 or $I4_1/a$ [56]. According to [168] NGW crystallizes in the Scheelite structure (space group I41/a) with cell parameters; a = 5.2483 Å and c=11.392Å. Phase formation was checked by X-ray powderdiffraction pattern employing RigakuRint 2000 X-ray diffraction system and orientation was verified by recording Laue pattern employing a Huber make Laue camera (Model 801). The UV-VIS-NIR absorption and transmission spectra of NGW were studied over the wavelength range of 200–800 nm on C-cut disks (2-10 mm thick) employing a spectrophotometer (Model: CHEMETO 2500). The crystal disks were polished to optical finish on both sides for optical measurements.

(iii) Photoluminescence studies: The intrinsic emission and excitation spectra were recorded in 200-800 wavelength range employing Edinburgh instruments make FLP 920 spectrometer. The emission corresponding to Yb^{3+} was recorded using an 450 m watt InGaS diode laser emitting at

985 nm as excitation source and an solid state spectrometer (Avantes: 3648) to record the emission in 800-1100 nm range.

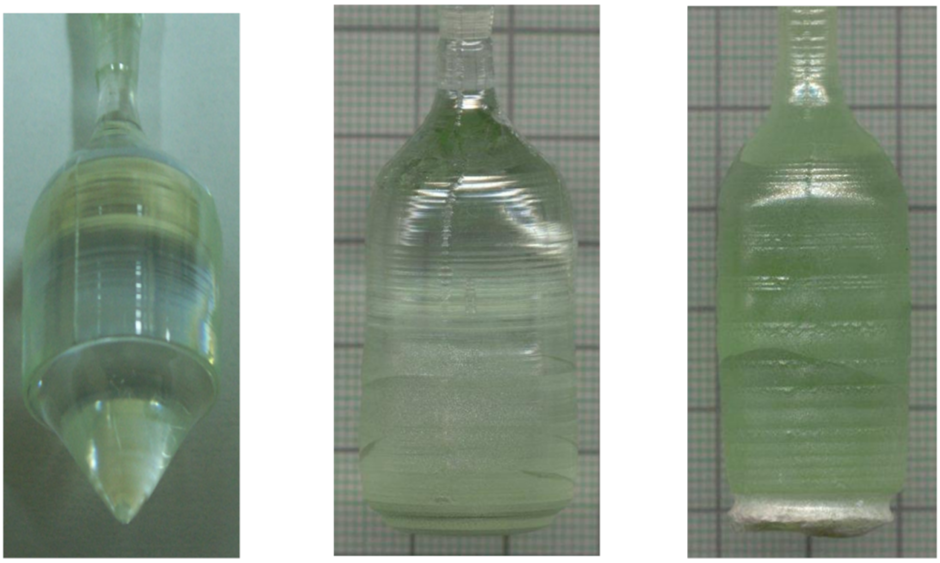

Crystal-I Crystal-II Crystal-III

Figure 4.10: Photographs of as-grown $NaGd(WO_4)_2$ crystal ingots.

4.2.3 Results and discussion

The photographs of crystals grown in three different conditions are shown in Fig. 4.10. The crystal-I was crack free and color less in appearance. On the other hand crystal-II was slightly greenish in color and has few minor cracks while crystal-III was dark greenish in appearance and was full of cracks. The results of crystal growth experiments show that the defects and stress generated due to the oxygen vacancies/interstitial (in crystal-II) and stoichiometry deviation (in crystal-III) are major factor in deciding the crystal quality. The X-ray powder diffraction pattern of crystal-I, crystal-II and III were identical with no detectable peak shifts though there was slight variation in the peak intensity. A typical powder X-ray diffraction pattern recorded for crystal-I is shown in Fig.4.11 along with the calculated pattern using Reitvel refinement. The crystal structure parameters are given in table-4.2 while the unitcell structure realized from the calculated structural parameters is shown in Fig.4.12. The same structural parameters were used for the ab-initio electronic band structure calculation using EXCITING code [127]. Laue pattern recorded of the crystal-I is shown in Fig.4.13. Orient express code was used for the fitting of the Laue pattern that confirmed the *c*-orientation of the grown crystals.

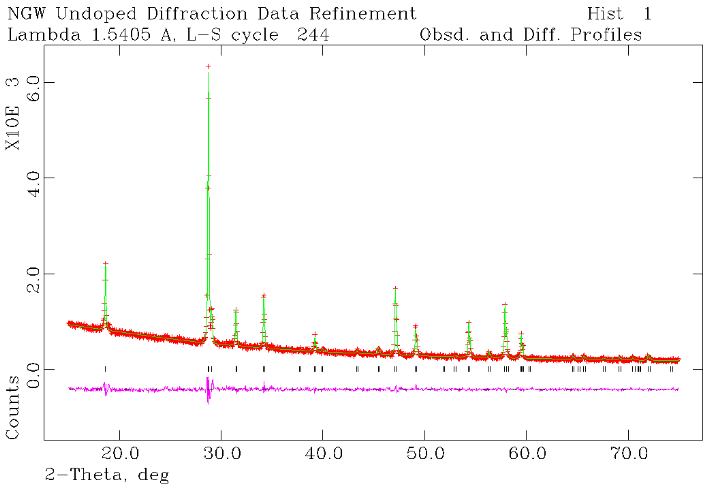

Figure 4.11: Powder XRD pattern of un-doped $NaGd(WO_4)_2$ (- × -) along with the calculated pattern (——) and residual (——).

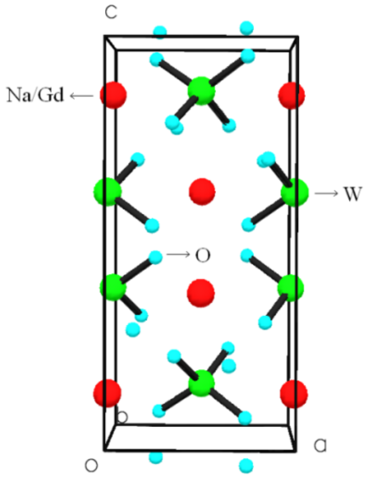

Figure 4.12: Calculated unit cell structure of $NaGd(WO_4)_2$.

Table-4.2: Calculated structural parameters of $NaGd(WO_4)_2$.

Lattice parameter	a=5.24404(12) Å; c= 11.3701(4) Å
Cell volume	312.678(17) Å^3
Space group	I 4_1/a

Atomic coordinates (x, y, z, Occupancy, U_{iso}, multiplicity)

NA1	0.0000	0.2500	0.1250	0.5	0.02554	4
GD2	0.0000	0.2500	0.1250	0.5	0.02554	4
W3	0.0000	0.2500	0.6250	1.0	0.02502	4
O4	0.7441	0.6009	0.0435	1.0	0.04740	16

The UV-VIS-NIR spectroscopy of the crystal revealed that the band edge of the crystals shifts towards lower wavelength in the order crystal-III>II>I (Fig.4.14a). The observed shift may be because of distortion of the WO_4 tetrahedra (that is the functional group of the material) due to change in oxygen coordination number of W. WO_4tetrahedra in crystal-I, that appears colorless and shows no absorption band in visible region (Fig.4.14b), may be considered as least distorted and hence is supposed to show better luminescence properties compare to other two crystals. Furthermore, the crystal-II and III show a broad absorption band throughout the visible range crystal that affects the crystal quality and luminescence properties. Defects generated in crystal-II and III may be of interstitial oxygen related as the growth of these crystal were carried out under oxygen rich environment relative to crystal-I and interstitial oxygen in tungstate and molybdate are known to introduce absorption band in the visible range [169, 170].

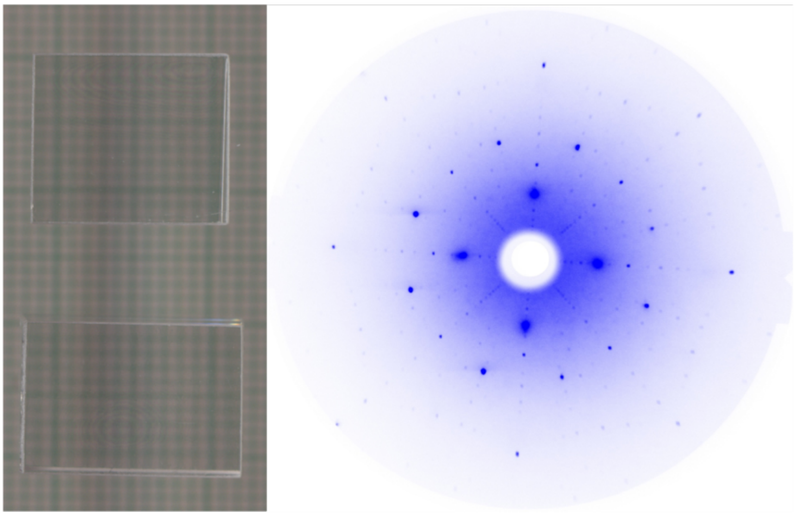

Figure 4.13: $NaGd(WO_4)_2$ crystal samples oriented along c-axis and the Laue pattern.

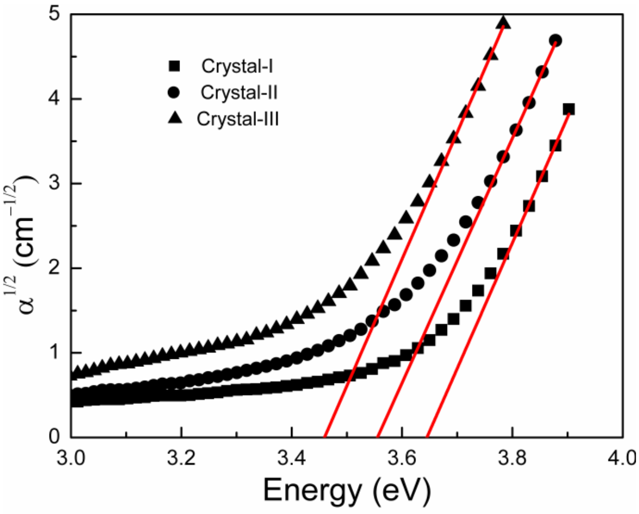

Figure 4.14a: Plot of square-root of absorption as a function of photon energy.

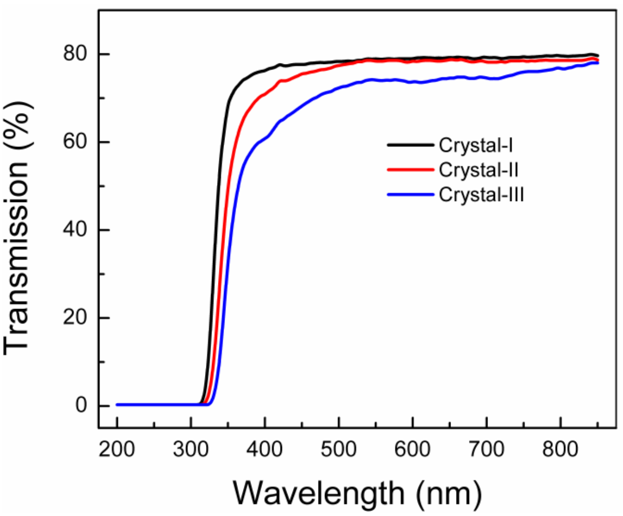

Figure 4.14b: Transmission spectra of $NaGd(WO_4)_2$ crystals.

Though the intrinsic luminescence spectra recorded for crystal-I at room temperature show a broad excitation peak centered at 270 nm and a broad emission peak at 480 nm (Fig.4.15) similar to other tungstates [171, 172], in this case additional sharp peaks centered around 313 nm were observed along with the characteristic excitation band of WO_4tetrahedra. These peaks belong to Gd levels. The density of state calculated for the NGW also shows remarkable difference from the other iso-structural single or double tungstate [173-175]. As shown in the Fig.4.16(a) and (b), there are states of Gd in the forbidden band just above the valence band. These state of gadolinium are related to the sharp peaks observed in the excitation band of NGW. This fact is also supported by the participation of Gd levels in the excitation/absorption spectra of other Gd containing material like $Li_6Gd_2(BO_3)_3$ [176]. The participation of Gd state in the 480 nm emission band indicates towards energy transfer from Gd to O atom of WO_4tetrahedra. This is also supported by the overlapping Gd and O density of states (Fig.4.16(b)). This may be one of the reasons that among double tungstate NGW is more luminescent at room temperature [59]. The PL decay profile for excitation at 313 nm and emission at 480 was recorded and is shown in

Fig.4.17. The profile could be fitted in two decay components;τ_1(45ns 20%,) and τ_2 (1150ns, 80%). This is different from the fast decay observed on other sheltie tungstate like PWO [177-179]. The slower component observed in the decay profile of WO_4 is due to the Gd contribution.

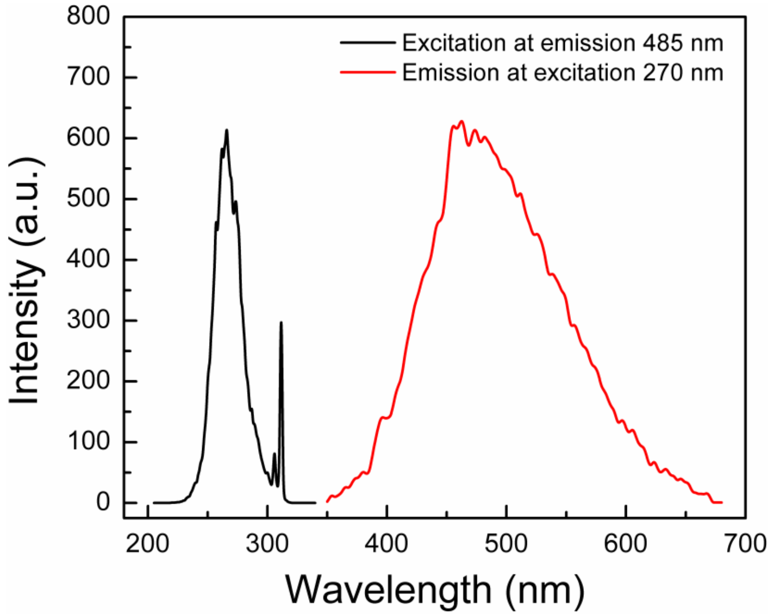

Figure 4.15: Emission and excitation spectra of $NaGd(WO_4)_2$ crystal at room temperature.

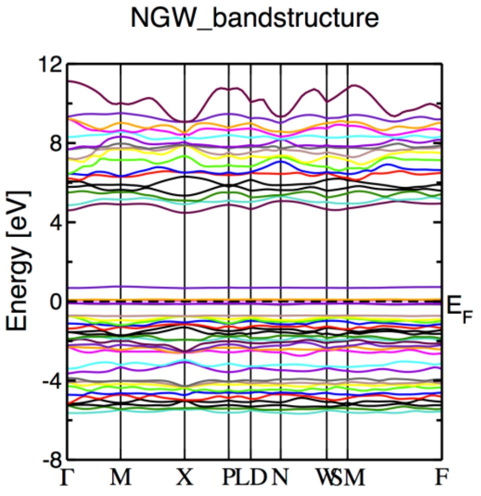

Figure 4.16a: Calculated band structure of $NaGd(WO_4)_2$.

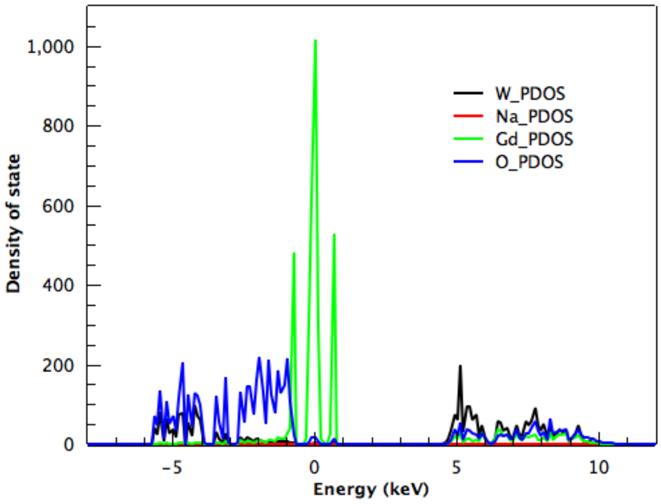

Figure 4.16b: Calculated density of state of each atom species in $NaGd(WO_4)_2$.

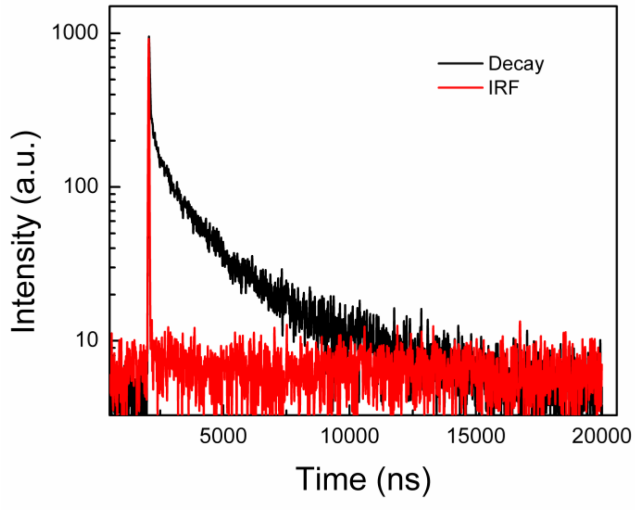

Figure 4.17: Decay profile of $NaGd(WO_4)_2$. (Crystal-I; excitation: 313 nm, emission: 500 nm).

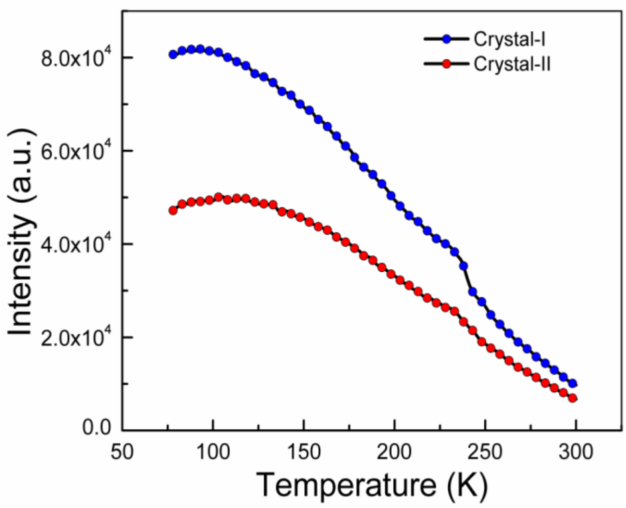

Figure 4.18: Temperature map of luminescence intensity of crystal-I and II.

Despite the differences in the absorption and transmission spectra, the shape of luminescence spectra of the crystal-I, II, and III were found to be more or less the same except for intensity. Crystal-III was least luminescent while the luminescence intensity of crystal-II was 70% of the crystal-I at room temperature. To see the role of oxygen on the thermal quenching temperature dependence of luminescence of crystal-I and II were studied (crystal-III was not considered as it involves stoichiometric variation too). Fig.4.18 shows the luminescence intensity of crystal-I and crystal-II as a function of temperature. Though the quenching temperature was more or less same the slope was different. Interestingly, the gradient of thermal quenching was steeper in the crystal-I despite its being relatively free of defects. This may be due to the fact that large defect density in crystal-II may cause considerable thermal quenching even at low temperature that may effectively decrease the slope gradient. The evolution of excitation and emission spectra of crystal-I is shown in Fig.4.19. Though the intensity of the emission and excitation increases as the temperature decreases, there was a small blue shift in the emission peak shift in the peak unlike the observed blue shift in NBW, an iso-structural material [180].

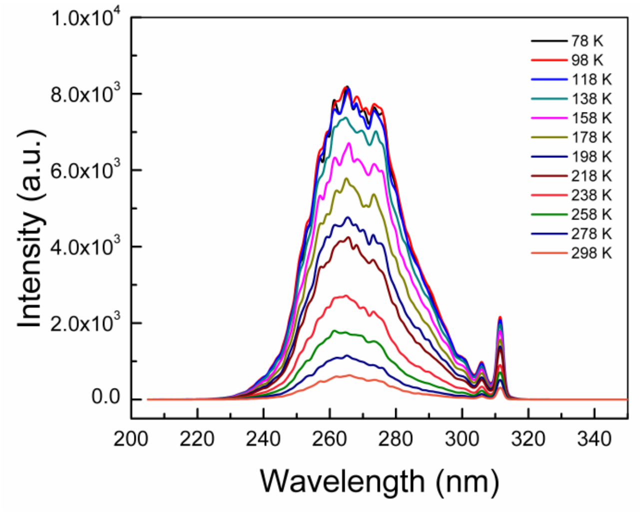

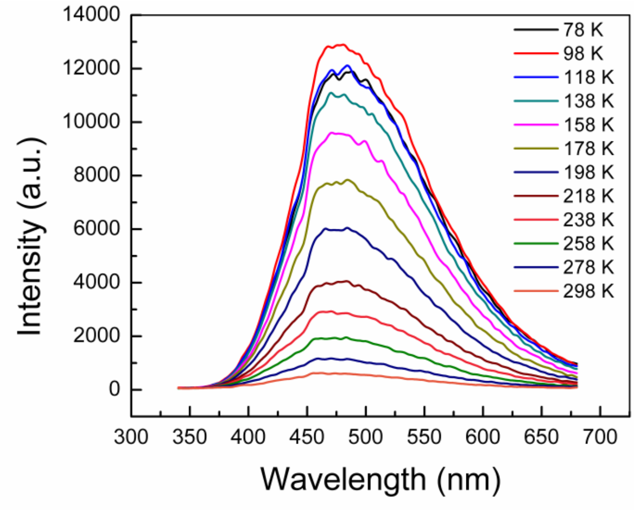

Figure 4.19a: Temperature map of excitation spectra of crystal-I.(with emission at 500 nm).

Figure 4.19b: Temperature map of emission spectra of crystal-I.(with excitation at 270 nm).

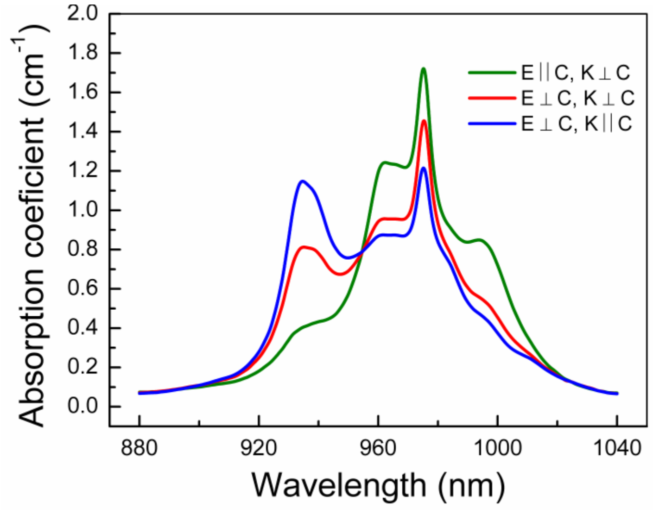

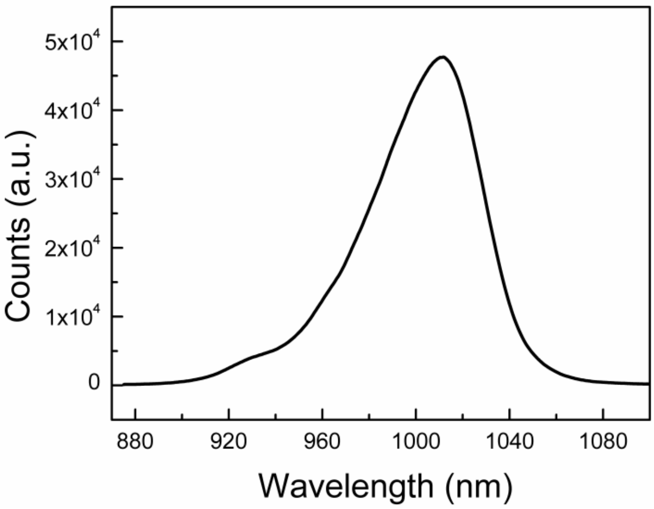

Figure 4.20: Excitation spectra of Yb in NaGd$(WO_4)_2$ matrix.

Figure 4.21: Emission spectrum of Yb in NaGd$(WO_4)_2$ for excitation at 975 nm.

Finally, as the NGW is a multifunctional material, the polarized NIR absorption spectra of the Yb doped NGW crystal (a laser material) was recorded in 850-1100 nm range with different combination of **E**, **k** and **c** **(**Fig.4.20). It is clear that for **E**||**c** and **k**⊥**c** the absorption is maximum for the 975 nm absorption that make it suitable for the pumping with InGaS diode laser. The emission spectrum for excitation in 980-990 nm range is shown in Fig. 4.21. It is in accordance with the reported values [56]. Though it shows a peak at nearly 1011 nm it is composed of several peaks centered at 935, 965, 975, 994, 1010, 1022 nm. The total broadening of the emission peak is around 60 nm that makes it suitable for the tunable femto-second laser source.

4.3 Conclusions

In summary, transparent and crack free single crystals of NBW and NGW were grown by CZ technique. The luminescence characteristics of both the crystals were thoroughly investigated. In case of NBW lower thermal quenching due to the presence of mobile charge carriers and only intrinsic photoconductivity in excitation region make it a more promising Cherenkov radiator compared to PWO crystals that are deployed currently in the high energy physics experiments at CERN. Two excitation bands observed in these crystals can be ascribed to the charge transfer transition from O to W and excitonic transition. Annealing in air or vacuum changes the environment of $(WO_4)^{2-}$ complex ions and consequently changes its luminescence properties. Based on these results One can optimize the growth conditions of NBW crystals to tailor the required properties and improve its Cherenkov characteristics.

In case of NGW it was established that the growth ambient affect the growth behavior as well as optical and luminescence properties of the crystal. The crystal grown in 90% Ar + 10% O_2 (crystal-I) shows the best crystal quality with controlled diameter and colorless appearance. This type of crystal was defect free with no absorption band in the visible range. The luminescence properties of NGW crystal were found to be strongly dependent on the growth ambient. The crystal grown in inert ambient with slight oxygen partial pressure shows best luminescence properties. The role of Gd level in luminescence process was found experimentally and confirmed theoretically by ab-initio band structure calculation.

CHAPTER 5

OPTICALLY TRANSPARENT CERAMIC OF Mn DOPED CaF_2

5.1 Introduction

The CaF_2:Mn is an important phosphor material for use as the thermo-luminescence (TL) dosimeter. The difficulty in growing doped single crystals of this material arises from high vapour pressure and different crystal structure of MnF_2 that prohibit its incorporation in the CaF_2 crystal lattice during the growth under vacuum conditions and leads to variations in the Mn concentration throughout the crystal. The difficulty in doping single crystals with Mn can be surmounted by preparing optically transparent ceramics (OTC) of this compound.

With the realization of Nd:YAG laser based on transparent ceramic in 1995 the interest in this field has increased tremendously [181, 182]. As a result the use of transparent ceramics in the field of lasers is now well established. In recent times transparent ceramics of several materials have been found with superior properties compared to their single crystal counterparts as these can be produced in large sizes and volumes in a cost effective processing, can have uniform and higher level of doping and with enhanced thermo-mechanical properties, etc.

Undoped CaF_2 single crystal is an important optical material with high transmission in a broad wavelength range (190-1600 nm) and used as IR window and other types of optical components like lenses, prisms, etc [71]. On the other hand doped CaF_2 is a multi-functional material that finds applications in lasers production (CaF_2:Yb), as radiation detectors (CaF_2:Eu) and as a thermo-luminescence (TL) dosimeter (CaF_2:Dy, CaF_2:Mn, CaF_2:Tm) [75, 183, 184]. The CaF_2:Mn also known as TL-400, is an important material for the TL dosimetry [185]. It has a single TL peak around 260°C and is linear for a wide range of doses, from 0.5 mGy to few kGy. However, the TL curve depends on the Mn concentration [186]. It has been shown earlier that the maximum glow curve intensity is achieved for a doping of 2.5 at% Mn [187]. It is desirable to use transparent CaF_2:Mn samples to obtain better sensitivity, higher light output and repeatability for dosimetric applications. The difficulty in growing doped single crystal of this material arises from the high vapor pressure of MnF_2 that prohibits its incorporation in the CaF_2 crystal lattice during the growth under vacuum conditions. It also leads to variations in the Mn concentration throughout the crystal. Hence, most of the reports on this material are either on polycrystalline powder samples or pellets [77,78]. The difficulty in the growth of single crystals can be circumvented by using optically transparent ceramics (OTC) of this compound.

Recently, fabrication of CaF_2 transparent ceramic doped with Yb, Eu, Er has been reported [188-192]. Several studies have been reported in the literature on transparent ceramics of pure and doped CaF_2. Except for CaF_2:Yb applications of these transparent ceramics have not been fully explored yet. Lyberis *et al* [191, 192, 193] presented the optical characterization of ytterbium doped CaF_2 transparent ceramics obtained from powders synthesized by a soft chemistry route, for high power laser applications. The Effect of Yb^{3+} concentration on optical properties of CaF_2:Yb transparent ceramics has been studied in order to check if the ceramic processing route affects the Yb^{3+} coordination in the processed ceramics [194]. Applications of transparent ceramics of differently doped CaF_2 have been reported in literature [192]. The CaF_2:Tm and CaF_2:(Tm, Ho) ceramics, prepared using hot pressing, and hot formation technique had been used as an active medium for a diode pumped mid-infrared tunable laser [195]. Similarly, processing of Er and Yb doped CaF_2 transparent ceramic has been reported by various groups [190, 196].

In this thesis the synthesis of CaF_2 transparent ceramics doped with Mn (2.5 at.%) has been carried out. These ceramics were found to exhibit properties comparable to the CaF_2 single crystals. The ceramic samples were characterized using XRD, SEM, SANS, UV-Vis, PL, SIMS and XPS and tested for possible thermo-luminescent dosimetric applications. Further, studies were carried out on samples that were prepared by co-doping Ce (0.5 at.%) with Mn (2.5 at.%) to understand the effect of Ce doping on TL dosimetric properties.

5.2 OTC fabrication and characterization of Mn doped CaF_2

The CaF_2:Mn (2.5 atm.%) transparent ceramics were prepared by hot pressing of nano-powders. The nano-powder was synthesized by a co-precipitation method [187]. Stoichiometric amounts of $CaCl_2$, $MnCl_2$ were dissolved in DI water and added drop wise to asolution containing NH_4F under continuous stirring to form white precipitates. The precipitate was washed by DI water and separated out by centrifugation. Then it was dried by annealing in vacuum at 450°C to remove all organic and moisture residues. For co-doping with Ce, $CeCl_3$ was dissolved in the $CaCl_2$, $MnCl_2$ solution and the same steps were repeated. To prepare the transparent ceramic (OTC), 15 g of nano-powder was taken in a high density graphite die (inner diameter: 40 mm) and hot pressed by applying 20 MPa pressure at1000°C in a vacuum chamber (base pressure $<10^{-5}$ mbar) followed by cooling at a uniform rate of 500°C/h down to room temperatures. The nano powder and prepared OTC were characterized for the phase identification using a diffractometer (Rigaku Model: RINT 2000 Dmax, Cu $K\alpha$ line). The microstructure of nanopowder and fractured OTC was studied using the SEM.

Fig.5.1(a) shows the SEM image of as-prepared nano-powder (with a particle size around 70 nm) of CaF_2:Mn after dehydration at 450°C. Fig.5.1(b) exhibits an SEM image of a polished surface of CaF_2:Mn OTC. To observe grain boundaries under the SEM, the OTC was cut, polished and chemically etched in hot HCl for 30 minutes. The average grain size has been found to increase to around 100 μm and the hot-pressed pellets had no voids or porosity. Secondary phases and cavities were absent at the grain boundaries. Thus vacuum hot pressing of the nano-powder at 1000°C for 2 h does not lead to any phase separation except an increase in the crystallite size. The relative density of the OTC was greater than 99%, as measured using the Archimedes's method. This further confirms the absence of any pores in the OTC.

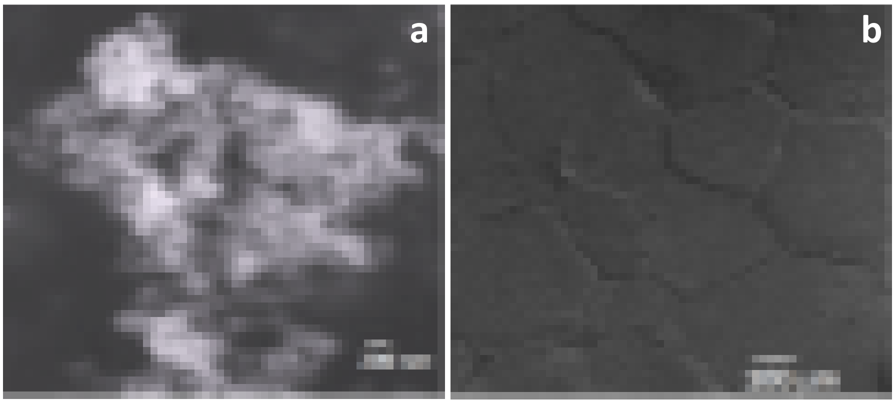

Figure 5.1: SEM image of (a) as-prepared nano particles and (b) optically transparent ceramic.

Small Angle Neutron Scattering (SANS) experiments have been performed on the virgin powders as well as vacuum sintered and hot pressed pellets, using a double crystal based medium resolution small angle neutron scattering instrument (MSANS) at Guide Tube Laboratory of the Dhruva rector at Trombay, India [197]. The instrument consists of a non-dispersive (1, -1) setting of (111) reflections from silicon single crystals with specimen between two crystals. Scattered intensities have been recorded as a function of modulus of wave vector transfer $|q| = 4\pi \sin(\theta)/\lambda$, where 2θ is the scattering angle and λ (=0.312 nm) is incident neutron wavelength] for present experiments. The SANS profiles of specimens, recorded by the instrument, were corrected for smearing effects after transmission and background corrections, using the methods given in literature [198]. For the SANS study three different types of samples of CaF_2 was considered. Sample-1, was as prepared pressed pellet of CaF_2 (cold pressed pellet), Sample-2, was pellet formed by pressing under pressure 20 M Pa at 900 °C for five minutes and sample-3, was hot pressed at temperature 900ºC and pressure 20 M Pa for 2 h. The Sample-1 is opaque, sample-2 translucent and sample-3 is transparent pellet of CaF_2.

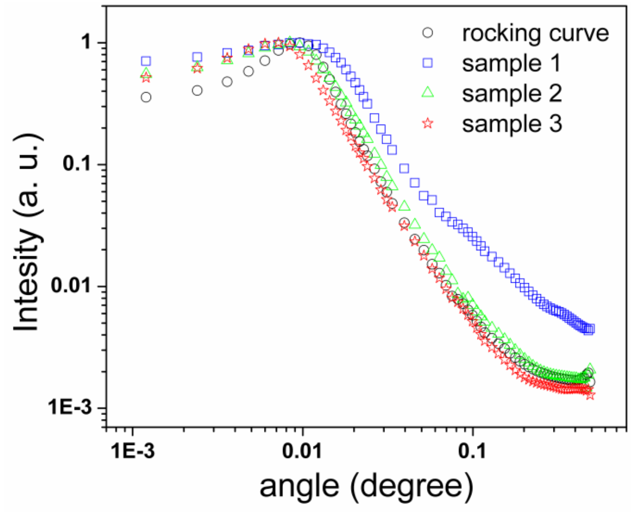

Figure 5.2: Raw data of SANS experiment carried out on CaF_2 samples.

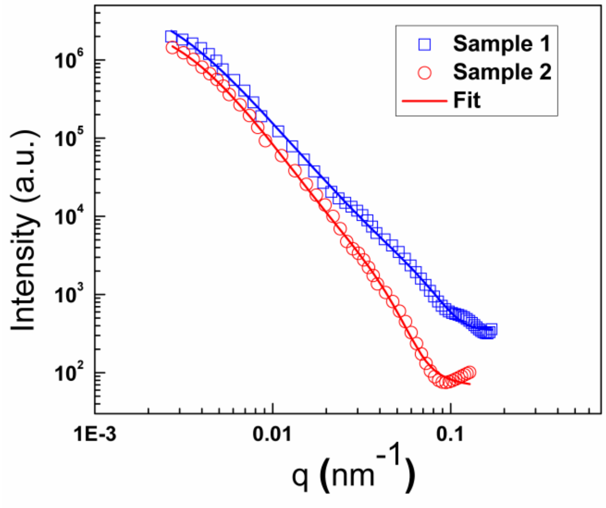

Figure 5.3: Processed SANS data.

In SANS experiment, the deviation of the scattering curves from the rocking curve, as shown in Fig 5.2, signifies that there is scattering signal in the specimens. The Sample-1, which is as prepared sample of CaF_2 (cold pressed pellet), possess the in-homogeneities in the form of voids in CaF_2 matrix. In general, as-formed specimen consists of agglomerates and inter/intra agglomerates pores. The information regarding the porosities may be extracted from the small angle neutron scattering. Since there is no scattering signal in sample-3, further analysis has been carried out only for sample-1 and sample-2. The process followed for the SANS data analysis is similar to that followed in reference [199].

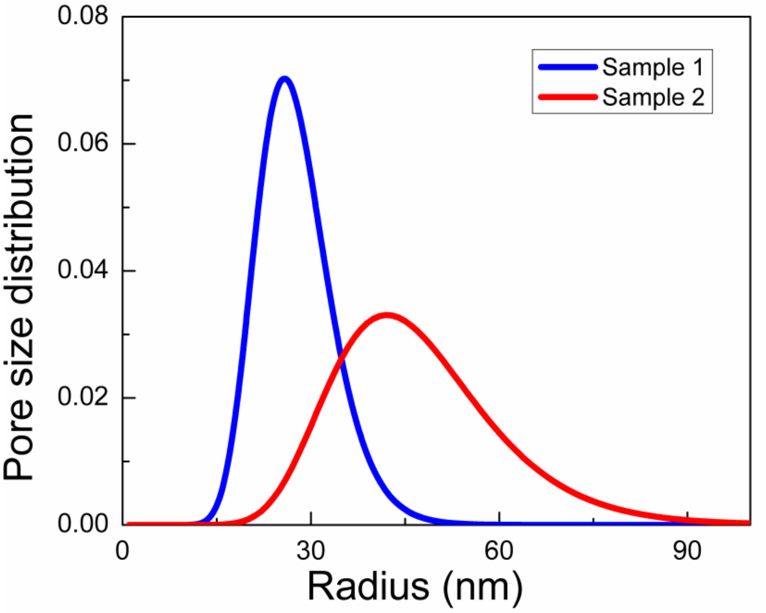

Figure 5.4: Pore size distribution in CaF_2 samples as calculated from SANS data.

It is evident from Fig.5.3 that the scattering signal decreases when pressure is applied. The sample-2, which was pressed under pressure 20 M Pa at 900°C for five minutes, has small scattering signal which shows that the number density of in-homogeneities (pores) decreases with respect to cold pressed sample. However, there are some porosity still exists in the sample which scattered enough light so that the sample appears only translucent (not transparent). The sample-3, which was hot pressed at temperature 900ºC and pressure 20 MPa for 2 h, has no scattering signal in present wave vector transfer range q. Thus, the specimen has no porosity in the preset experimental length scale (1 nm to 1 μm). This behavior is well supported by the transparent nature and high density (> 99 %) of the pellet. Thus it is clear that translucent property is more in the sample that has less porosity. In the present case, sample-3 possesses the highest transparency.

Fig. 5.4 shows that the average pore size in the sample-1 is smaller as compared to that of the sample-2. Though the pour size in the sample-2 is larger than that in the sample-1 but their number density is much smaller. Larger size of pour in sample-2 is because of agglomeration of void through diffusion towards each other and from the two curves it may be inferred that under the prevailing conditions of temperature, pressure and time, on an average two pores merged together apart from annihilation of smaller one. Thus when the sample was kept at 900ºC and 20 MPa pressure voids grow in size and later on annihilated due to grain growth of CaF_2 crystallites.

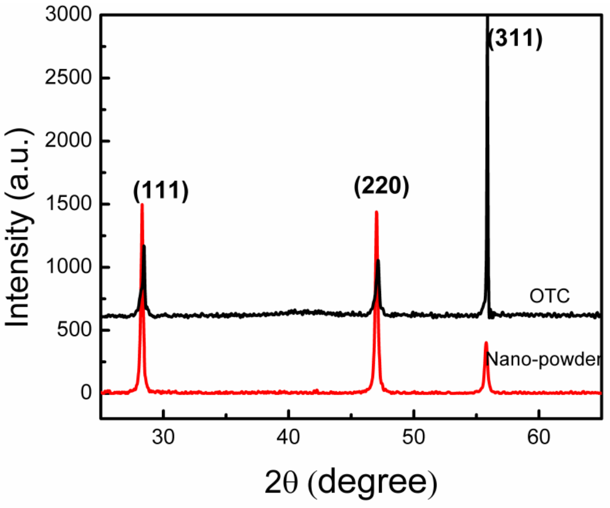

Figure 5.5: XRD spectra of as grown nano particles and OTC of CaF_2:Mn.

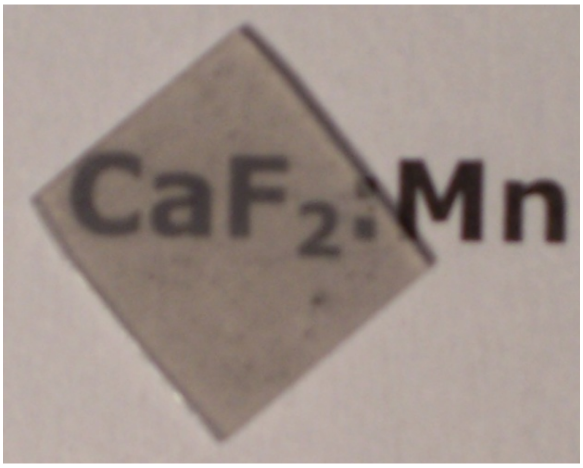

Figure 5.6: Optical image of a 2mm thick sample of Mn doped CaF_2 transparent ceramic.

The change in the crystallite size on vacuum pressing is further supported by XRD spectra shown in Fig.5.5. For both the as-prepared and hot-pressed samples (nano-powder and OTC) all the diffraction peaks could be indexed to the cubic structure of CaF_2 with a lattice constant of a = 5.47Å without any impurity phase [JCPDS 04-0864]. No peak corresponding to MnF_2 was detected. All the peaks are located at almost the same position of CaF_2 (up to 2.5 at.% of Mn) with a small shift that indicates that Mn is incorporated into CaF_2 lattice and does not distort the crystal lattice appreciably. The crystallite size of the nano-powder calculated using the Deby

Scherer's formula was about 40 nm. The XRD pattern of the OTC is similar to that of the nano-powder with the (311) peak having the maximum intensity. An asymmetric broadening in the peaks of OTC was observed that may arise due to defects (dislocation, slip planes, etc.) generated because of the pressure applied at high temperatures and not due to crystallite size as reported by Groma *et al*. [200]. The shift in the position of XRD peaks of the OTC also confirms that Mn is retained in the lattice of CaF_2 even after sintering at 1000°C.

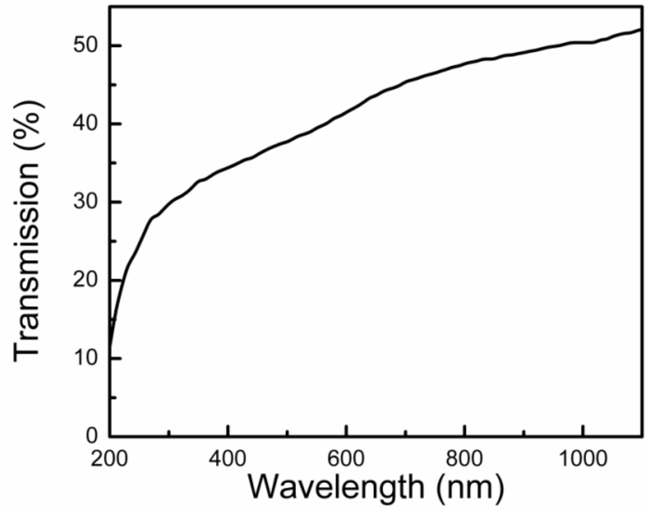

Figure 5.7: Transmission spectrum of a 1 mm thick sample of Mn doped CaF_2 transparent ceramic.

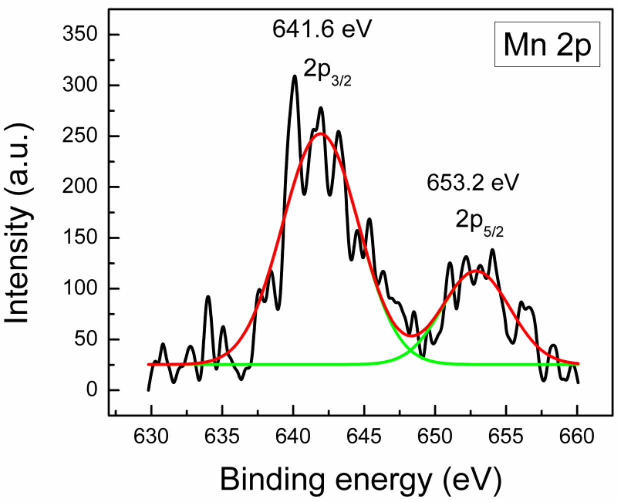

Figure 5.8: XPS spectra of Mn 2*p* peak of CaF_2:Mn OTC.

The 40 mm diameter disc of OTC prepared by hot-pressing is cut and polished for further studies. Fig.5.6 shows the photograph of a polished 2 mm thick 10 mm x 10 mm CaF_2:Mn sample. The transmission in the UV-Vis range (200-1100 nm range) was recorded using a spectrophotometer (Chemito-2500 UV-Vis) and in the IR region by FTIR spectroscopy (BRUKER Model VERTEX 80V). The in-line transmission spectrum recorded for this ceramic in the UV-Vis region is shown in Fig.5.7. The transmission is about 50% above 800 nm that decreases at lower wavelengths with a cutoff around 200 nm [71]. The transmission at 2000 nm recorded using an FTIR was about 64% (figure not shown). This is comparable to the reported transmission for a CaF_2:Yb OTC sample [188]. A mirror-finish polishing of the ceramic can further improve the transmission.

The elemental analysis of the OTC was carried out using the SIMS. The quantitative analysis confirmed the presence of Mn doping in the OTC. Concentration of Mn was found to be in the range of 1-1.5 at.%. This is similar to results obtained for the sintered samples of CaF_2:Mn [187]. It appears that the total amount of Mn added to the solution does not incorporate into the lattice of CaF_2 OTC and evaporates during the high temperature processing. Further the oxidation states of the Mn dopant in the OTC were determined using an X-ray photo-electron spectrometer (XPS). Fig.5.8 shows an XPS spectrum of the 2*p* peak of Mn. The binding energies of the $2p_{3/2}$ and $2p_{5/2}$ peaks ware found to be 641.6 eV and 653.2 eV respectively. These values correspond to the reported binding energies in $MnCl_2$ that confirms the Mn^{2+} state in the CaF_2 OTC [201]. It may be noted that the Mn^{2+} state in the CaF_2 is desirable for the dosimetry applications. A vacuum environment maintained during the sintering of the OTC may be responsible for the absence of Mn^{4+} state in the sample.

5.3 Luminescence characterization and analysis

5.3.1 Thermo-luminescence Characterization

The dosimetric properties were investigated by irradiating the samples with a ^{60}Co gamma source. The thermally stimulated luminescence (TSL) glow curve was recorded using an indigenously developed thermo-luminescent dosimetry setup as described in Chapter-2. It consists of a sample heater controlled by a temperature controller (Eurotherm Model-2614, heating rate of 1K/s) and a PMT read-out. The output current of the PMT was measured using a pico-ammeter (Keithley Model-6487) as a function of temperature using a computer controlled program. The linearity of the exposed dose was determined by exposing the sample to a standard gamma-ray source for different durations.

The OTC was cut into small pieces each weighing about 10 mg and exposed to ^{60}Co to carry out TL dosimetric studies. The glow-curve recorded after a gamma dose of 100 mGy is shown in Fig.5.9. A single glow-peak at 260°C was obtained [202]. The minimum dose that could be measured was about 3 mGy. The wavelength of the emission spectrum recorded during photoluminescence and thermoluminescence measurements was found to be the same (470 nm). This indicates the observed excitation bands in both the cases are due to the internal transitions of Mn^{2+} states as reported earlier and that the exposure to γ radiation does not change the ionic state of Mn^{2+} [203]. This fact indicates a possible formation of hole traps. Inset of Fig.5.9 shows the dose linearity of the OTC, measured by irradiating the OTC to different doses and measuring the area under the glow-peak. The sample is found to be linear up to the highest dose of 100 mGy used in the present work.

To compare the TL response of the OTC with an opaque CaF_2:Mn pellet, the as-prepared nano-powder (with same Mn doping concentration) was cold pressed into a pellet and annealed at 300°C. This opaque pellet was exposed to a ^{60}Co source for different doses along with the OTC to study their TL properties. However, even after exposure to a dose of 10 Gy the glow curve could not be recorded for the opaque pellet. While the OTC samples could produce clear glow curves even for doses in the mGy range (Fig.5.9). Earlier, a minimum dose of 50 Gy has been reported for the opaque pellets of CaF_2:Mn [78]. This suggests that the OTC samples are more sensitive compared to an opaque pellet and can be used to measure low doses.

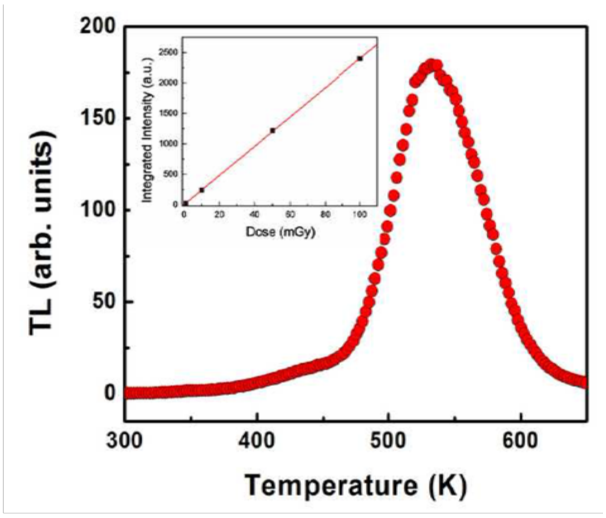

Figure 5.9: Glow curve of CaF_2:Mn OTC after irradiation with a dose of 100 mGy. The inset shows the dose linearity of CaF_2:Mn OTC.

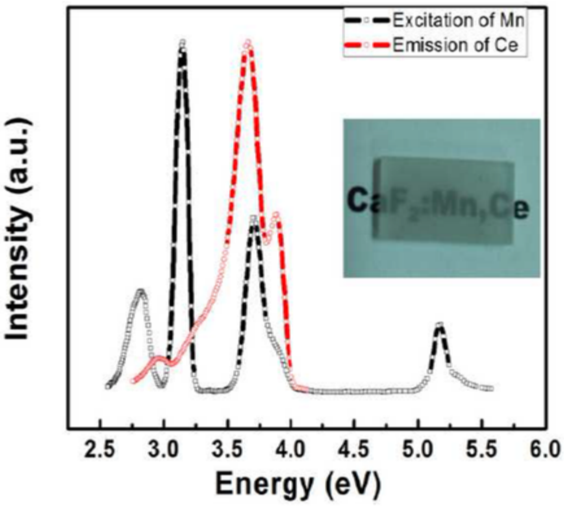

Figure 5.10: Emission spectrum of Ce^{3+} and excitation spectrum of Mn^{2+} in CaF_2:Mn,Ce OTC showing the over-lapping of Ce emission band with Mn absorption. Inset shows the optical photograph of a CaF_2:Mn,Ce OTC.

In an independent experiment, OTC samples of CaF_2 co-doped with 2.5 at.%Mn and 0.5 at.% Ce were prepared using the technique described in the preceding section. The idea was to increase the efficiency of the TL glow curve through an energy transfer mechanism involved between Ce^{3+} to Mn^{2+} ions in the CaF_2 matrix [204-206]. A sample plate of CaF_2:Mn,Ce OTC having a thickness of 2 mm is shown in the inset of Fig.5.10. The energy transfer was confirmed by recording the PL spectra of this sample. In Fig.5.10 the emission peak at 330 nm of Ce^{3+} lies in the excitation energy band of Mn^{2+} at 336 nm indicating a possibility of an energy transfer occurring between Ce^{3+} and Mn^{2+} in the CaF_2 matrix.

Fig.5.11 compares the TL glow curves for the same dose for co-doped OTC sample (CaF_2:Mn,Ce) and CaF_2:Mn OTC. The dose linearity of the co-doped sample is given in the inset. The glow curve of the co-doped OTC shows an extra peak at 125°C with an intensity five times recorded for a CaF_2:Mn sample (for 260°C peak). This curve could be deconvoluted into two peaks at 95°C and 125°C. This OTC sample is found to detect a minimum dose of 0.8 mGy with dose a linearity up to 200 mGy. However, the low temperature peak (125°C) was susceptible to fading with long storage times at room temperatures. Contrary to increase in the intensity of the glow-peak at 260°C due the energy transfer, a slight decrease in the intensity for has been observed. This implies that Ce^{3+} may be creating new trap-centers that may interfere with those from Mn^{2+}.

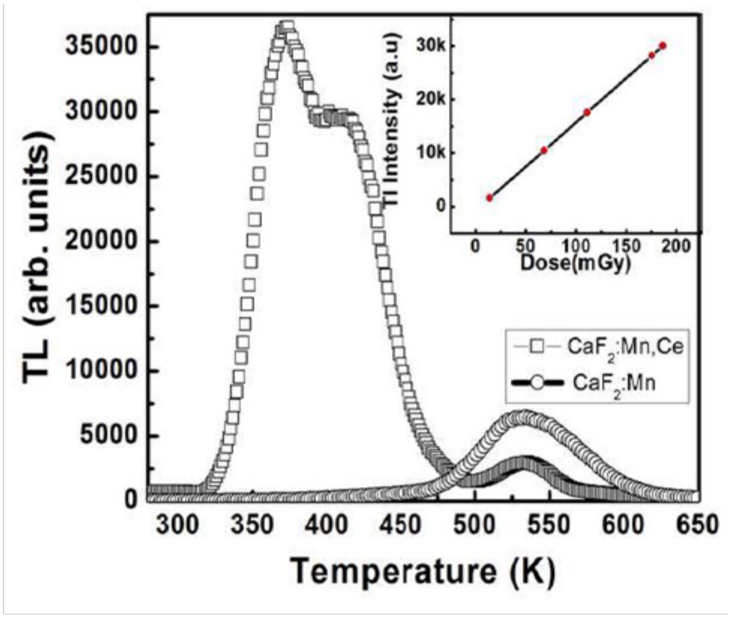

Figure 5.11: Glow curves of CaF_2:Mn and CaF_2:Mn,Ce OTC after irradiation with 0.66 Gy. Inset shows the dose linearity of CaF_2:Mn,Ce OTC.

5.3.2 Low temperature photoluminescence studies

CaF_2:Mn is an important material for applications in radiation dosimetry. The material is commonly known as TLD-400 and it is particularly useful in the environmental radiation dosimetry [207]. In the previous section [208-211] it was shown that optically transparent ceramics of CaF_2:Mn exhibited a better sensitivity to lower doses of gamma as compared to polycrystalline samples. The luminescence properties of CaF_2:Mn have been studied in detail in the past [212]. These studies are performed either on Mn doped CaF_2 single crystals or on the sintered powder [78]. The emission displays a characteristic maximum at 495 nm due to the relaxation of electrons from one of the internal *4G* excited states of Mn^{2+} to the ground-state *6S* level [213]. In the CaF_2 lattice Mn^{2+} is incorporated as a substitution for Ca^{2+}. Its point group symmetry is O_h and it possesses eight-fold coordination with the surrounding F^-ions. However, the spectral location of the emission (in the green) is usually associated with fourfold coordination. Alonso and Alcala [203] however, from a careful analysis of the excitation spectra from CaF_2:Mn, assigned the emission to a transition from the first excited $^4T_{1g}$ *(4G)* level to the ground-state $^6A_{1g}$ *(6S)* level; the $^4T_{1g}$and $^6A_{1g}$ terms arise from the cubic crystal field splitting of the original *4G* and *6S* states for the $3d^5$ electrons of the Mn^{2+} ion. Alonso *et al* calculated the crystal field Dq= 425 cm^{-1} for Mn^{2+} in CaF_2.

Low temperature emission studies were carried out to understand the luminescent process and compared with that in CaF_2:Mn single crystals. Though the room temperature (RT) results found in this study are in agreement with the reported values, there are significant differences in the temperature dependence of the luminescence properties. The observed results have been compared with the reported values and an explanation has been proposed for the obtained results.

The photo-luminescence from CaF2:Mn OTC was recorded in the range 200-800 nm (spectral resolution: 0.1 nm) using a fluorescence spectrometer (Edinburg Model-FLP920) for a temperature range of 77 - 300K. A cryostat (Oxford, Optistat-DN) was used for the low-temperature measurements down to 77K. The emission was recorded in the reflection geometry by positioning the sample at 45° with respect to the excitation beam. A steady state xenon lamp was used as an excitation source and a spectral bandwidth of 1 nm was selected for both excitation and emission arms (for high resolution measurements, a spectral bandwidth of 0.1 nm was used). The recorded luminescence spectra were corrected for the spectral sensitivity function of the instrument. A xenon flash lamp having a pulse width of 10 μs and a repetition frequency of 2 Hz was employed to record the lifetime spectrum. X-ray induced emission spectra were measured using an in-house built set-up. The X-ray source was an X-ray tube with Cu target. The accelerating voltage and tube current were set at 40 kV and 30 mA, respectively. An Avantes make (model: 3648) spectrograph was used to measure the emission spectra.

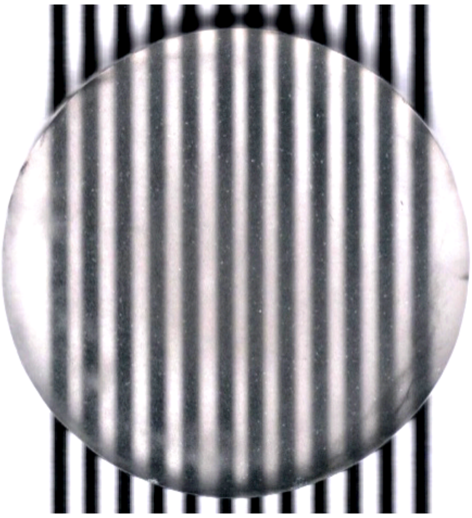

Figure 5.12: Optical photograph of a 25 mm diameter and 3 mm thick transparent ceramic of CaF_2:Mn.

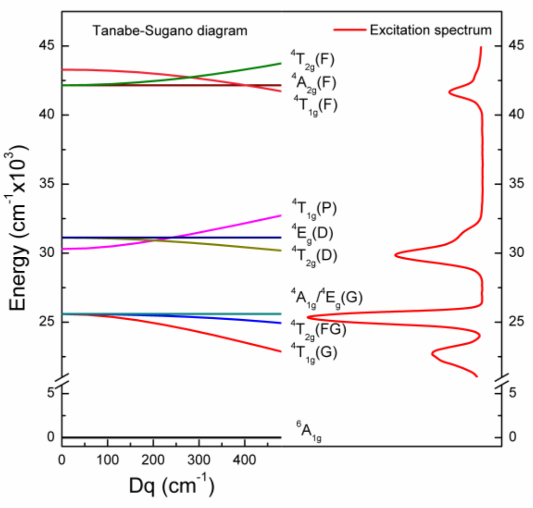

Figure 5.13: Tanabe Sugano diagram for d^5 electronic configuration and recorded excitation spectrum (on the right) of CaF_2:Mn transparent ceramic at room temperature.

Fig.5.12 shows the optical photograph of a CaF_2:Mn transparent ceramic of 25 mm diameter and ~3mm thick. The optical transmission measurements showed a maximum transmission of about 55-60% at 1000 nm for a 3 mm thick disc. The photo-luminescence properties of OTC of CaF_2:Mn have been studied in the wavelength range from 200 nm to 900 nm.

The transition responsible for the Mn^{2+} excitation band has been assigned to different levels as per the Tanabe-Sugano diagram. The calculated levels and observed excitation spectrum are shown together in Fig.5.13. From the figure it is clear that all the four excitation bands are present in the excitation spectrum. The excitation band at 240 nm was very difficult to observe in the CaF_2:Mn mainly because of the oxygen related and other defects that had transition level below 250 nm [214, 215]. The results suggest that the CaF_2:Mn transparent ceramic is free from the oxygen related defects presumably because it is processed from oxygen-free components in a highly reducing carbon ambient under high vacuum conditions. The complete excitation and emission spectra of the CaF_2:Mn transparent ceramic are given in Fig.5.14(a). The emission spectrum shown in Fig.5.14(b) corresponding to the excitation band 395 nm is the same for the other excitations bands, indicating a non-radiative transition from all the higher levels to the lowest excitation level $^4T_{1g}$(G). The emission observed at 550 nm is due to the transition from the $^4T_{1g}\,(G) - {}^6A_{1g}\,(G)$ states [214].

The temperature dependence of the emission corresponding to $^4T_{2g}(FG) - {}^6A_{1g}$ (G) states has been reported in the literature, however, an evolution of excitation spectra with temperature has remained unexplained [214]. Based on the present study, a temperature map of excitation spectra is shown in Fig.5.15. An enlarged view of the most intense excitation peak (3 to 3.2 eV) is shown in Fig.5.16. From the Fig.5.16 it is clear that the broad peak consists of several individual peaks.

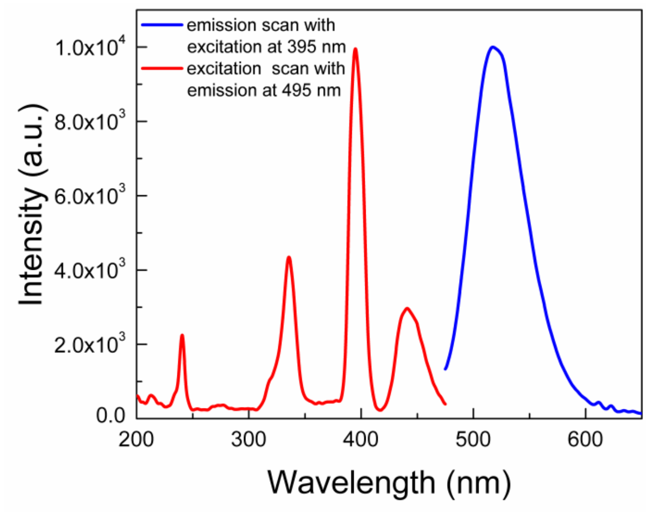

Figure 5.14a: Excitation and emission spectra of CaF_2:Mn transparent ceramic at room temperature.

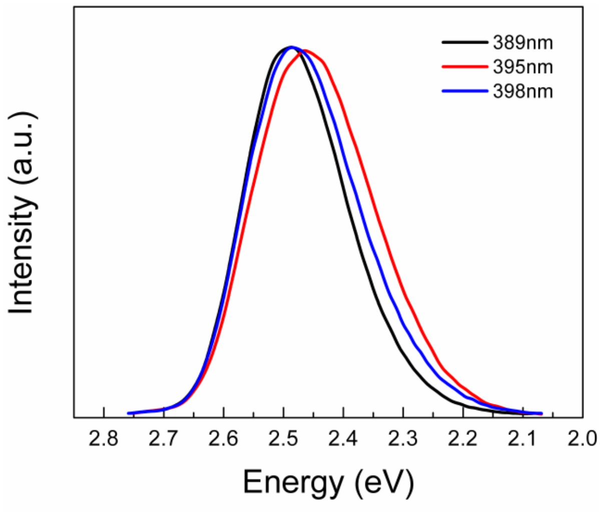

Figure 5.14b: Room temperature emission peak of CaF_2:Mn transparent ceramic corresponding to excitation different at different wave-lengths.

The temperature dependence of the emission intensities corresponding to excitations at 389 nm, 395 nm and 402 nm has been studied and results are shown in Fig.5.17. The emission intensity corresponding to all the excitations at 77 K has been normalized to 10000 for comparison. The temperature behavior of these transitions showed that the emission intensity corresponding to the excitation at 389 nm decreases very slightly above 110 K while that corresponding to excitations at 395 and 402 nm increased considerably at temperatures above 110 K. This finding is contrary to the observed temperature quenching [203, 215]. The intensity of all the three excitations at 395 nm, 335 nm and 445 nm is found to increase with temperature, however, the increase in the intensity of excitation at 395 nm is more than the other two, as shown in Fig.5.17 (b).

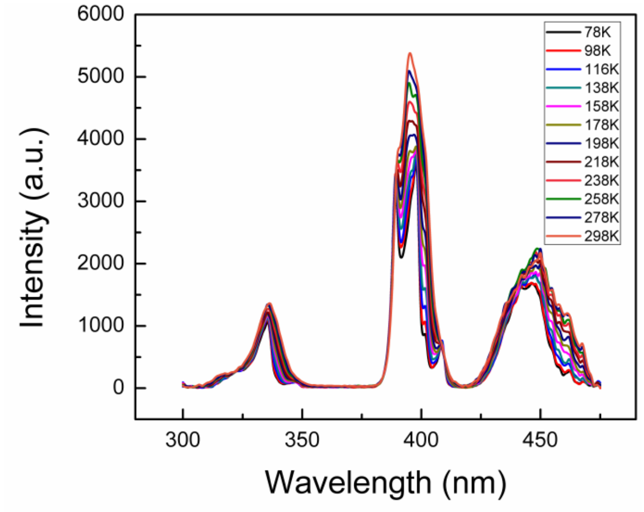

Figure 5.15: Temperature map of the entire excitation spectra in the 300-500 nm range for emission at 500 nm of a CaF_2:Mn transparent ceramic.

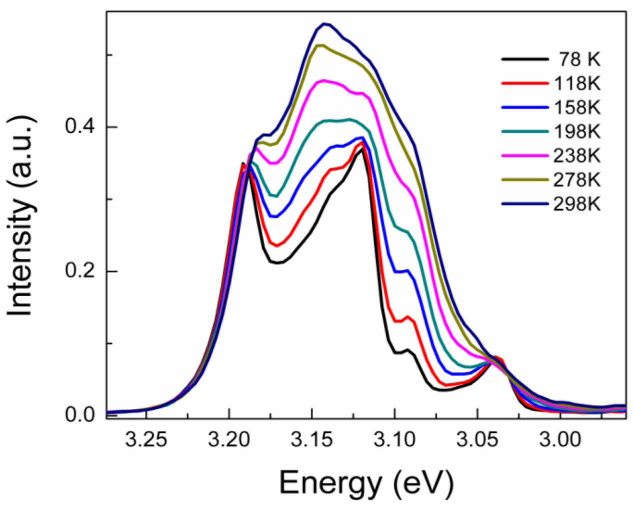

Figure 5.16: Enlarged temperature map of the excitation spectra in the range 3.25-2.75 eV (380-450 nm) for emission at 500 nm of a CaF_2:Mn transparent ceramic.

The decay of all the transition was recorded and it was found that the decay profiles of all the levels are more or less similar because of the fact that the emission occurs due to a transition in the $4T_{1g}\ (G) - 6A_{1g}\ (G)$ states in all the cases. The temperature evolution of the decay profile of $4T_{1g}\ (G) - 6A_{1g}\ (G)$ states is shown in Fig.5.18. Though the Alcala et al reported only one decay component, our data could be fitted in two exponential components indicating two decay times for the above mentioned transition [203]. The temperature behavior of these two components along with the average decay time is plotted in Fig.5.19. The faster decay time (τ_1) is nearly independent of temperature (varies from 30 ms to 37 ms) while the slower one (τ_2) varies from 90 ms to 180 ms. Here the change in decay component begins from 120 K which is similar where the emission intensity starts to change rapidly as shown in Fig.5.17b. Though the temperature behavior is in agreement with that reported by Alcala et al., in the present case it is accompanied by a change in the emission intensity, whereas a constant emission intensity up to 450 K was reported earlier [214, 215].

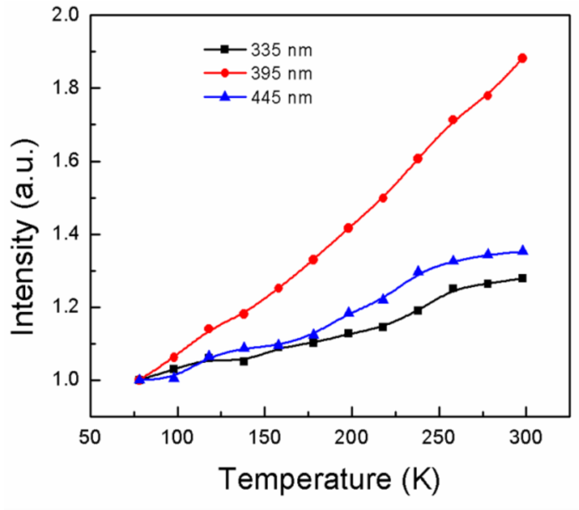

Figure 5.17a: Intensity as a function of temperature for excitation at 335 nm, 395 nm and 445 nm.

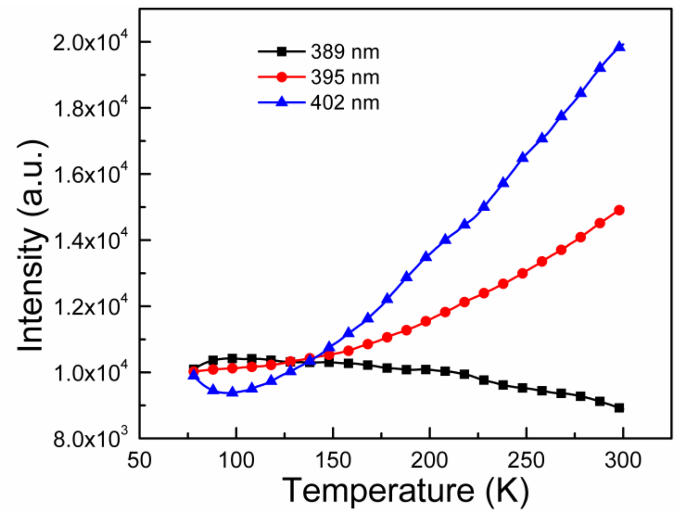

Figure 5.17b: Temperature dependence of constituent peaks of 395 nm excitation band for a transparent ceramic of CaF_2:Mn.

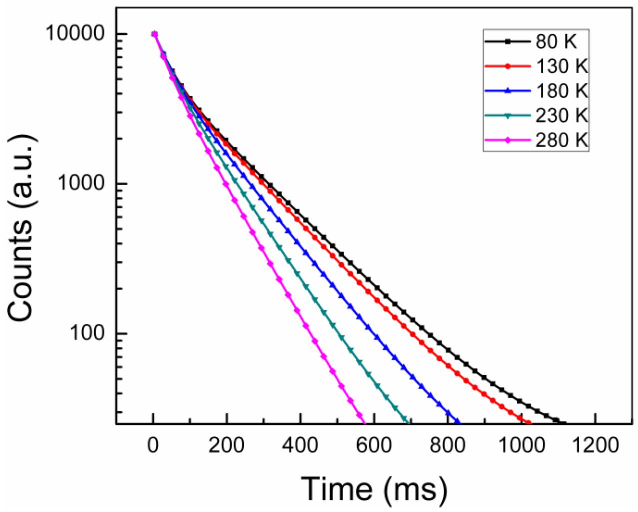

Figure 5.18: Temperature map for the decay profile of CaF_2:Mn transparent ceramic (excitation: 395 nm; emission: 500 nm).

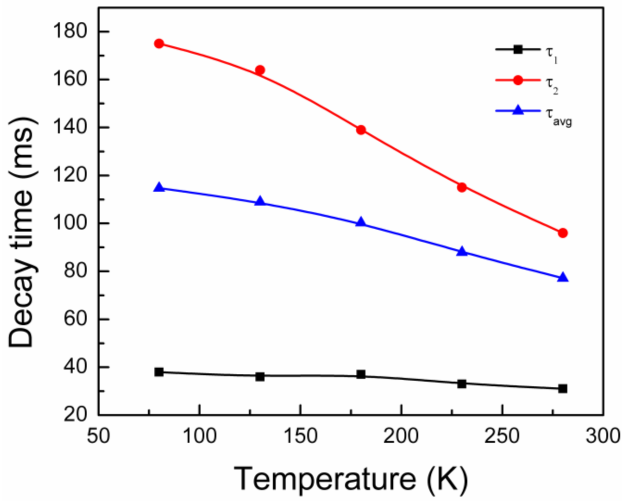

Figure 5.19: Temperature behavior of the two decay constants τ_1 and τ_2 of CaF_2:Mn transparent ceramic. The τ_{avg} is the average time constant of the two decay components.

These observations can be explained by assuming that between the two components τ_1 and τ_2, the faster one (τ_1) is a pure radiative type with a negligible phonon contribution (as inferred from the largely temperature independent behavior) while the slower one (τ_2) is a phonon assisted transition that depends on temperature. Here, the phonon density that increases with increasing temperature facilitates the usually forbidden transition. This increases the rate of transition consequently decreasing the decay time. This is also reflected in an increased fraction of τ_2 in the overall decay and increase in the emission intensity with the temperature. This phonon assisted transition is significantly less in the case of single crystals whereas the fraction of this transition is significant in ceramics leading to a different observation in the present studies than those reported for single crystals in literature [215].

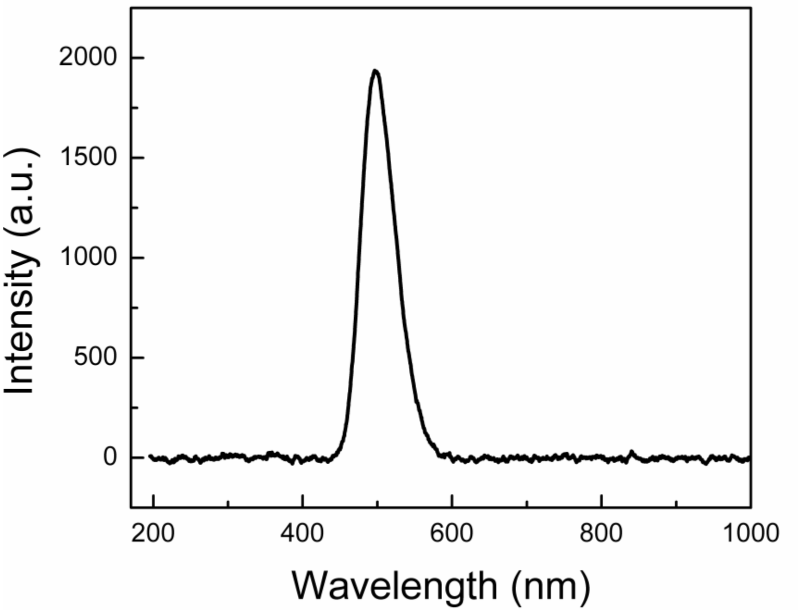

Figure 5.20: X-ray induced radio-luminescence spectrum of a CaF_2:Mn transparent ceramic.

Further, the transparent ceramics of CaF_2:Mn were checked for their scintillation properties. Fig.5.20 shows the room temperature X-ray induced radio-luminescence spectrum of a CaF_2:Mn transparent ceramic in the range from 200 nm to 1000 nm. A sharp peak recorded around 500 nm is similar to the photo-luminescence emission of this material. Absence of any additional peak in the radio-luminescence spectrum suggests that there is no other impurity, secondary phase or other dopant present in the CaF_2:Mn transparent ceramic. This emission coincides with the spectral sensitivity of a charge-coupled device (CCD) arrays, suggesting a possible use of the CaF_2:Mn transparent ceramic in digital X-ray imaging detector based on a CCD imager.

5.4 Conclusions

High quality transparent ceramic of CaF_2:Mn was prepared by a vacuum hot press method. A doping concentration of 1.5 at.%Mn has been successfully achieved in the CaF_2 OTC in spite of sintering at high temperatures under vacuum conditions, as confirmed by XPS and PL measurements. The ceramic was characterized for its photo-luminescence properties at low temperature down to 77K. Measurements suggest that the ceramic is devoid of any secondary phase or impurity or oxygen contamination. Though the luminescence properties at room temperature are similar to those reported for single crystals, the temperature dependence was found quite different than that in the single crystals. While in single crystals the luminescence intensity is reported to be constant up to 450K, in OTCs it was found to increase with temperature (from 77K to 300K). This may be put to advantage in the TL applications where the luminescence takes place at relatively higher temperatures. This study shows that the CaF_2:Mn OTCs have superior luminescence properties over the single crystal and therefore can be considered as a potential substitute for single crystals in certain applications. Thermo-luminescence studies carried on the CaF_2 OTC doped with Mn^{2+} exhibited promising characteristics and can be used as a TL dosimeter for applications in the personal and environmental safety.

CHAPTER 6

SUMMARY AND CONCLUSIONS

In my thesis I have studied the effect of preparation procedure and growth parameters on the properties of three materials (i) CsI and (ii) $NaR(WO_4)_2$; R = Gd, Bi as a prompt scintillator in the form of single crystals and (iii) Mn doped CaF_2(in the form of OTC) as a material for thermally stimulated luminescent dosimeter. The aim of the study was to make single crystal growth procedure easy and simple and second, to develop a better substitute for Mn doped CaF_2 single crystals for applications in radiation dosimetry.

Tl doped CsI single crystal: Single crystals of CsI are conventionally grown using the Bridgman technique. The growth of CsI crystals does not pose major problems. However, sticking of the grown crystal to crucible walls makes their extraction difficult and stresses are generated during the recovery process. These issues are important and need to be addressed to grow device grade crystals. In this Ph.D. work two different approaches were opted to grow detector grade single crystals of Tl doped CsI of 50 mm diameter and 60 mm length; (i) Growth of CsI:Tl single crystals in carbon coated silica crucibles and (ii) Growth of CsI:Tl crystals using a modified Bridgman method.

In the first method, single crystal of Tl doped CsI crystals of 35 mm diameter and 40-50 mm length were grown in carbon coated fused silica crucibles by a gradient freeze technique that exhibited good radiation hardness. Effects of the axial temperature gradient inside the melt, cooling rate and post-growth annealing on the crystal growth and luminescence properties have been studied and optimum conditions were found. Results of a systematic study carried out on the effects of growth process on radiation hardness, day-light coloration and related afterglow of CsI:Tl was studied. A possible process of defect formation for induced coloration is proposed and methodology adopted for their successful removal is discussed.

In a different approach a modified Bridgman technique was developed to grow the CsI single crystal of 50-55 mm diameter and 60-70 mm length. The Bridgeman furnace, employed for crystal growth, consists of four independently controlled resistive heating elements. Top isothermal zone consisting two heating element is separated from bottom isothermal zone using a 50 mm thick baffle (adiabatic zone). A maximum 20^{o}C/cm temperature gradient was achieved in the adiabatic zone. A specially designed silica glass crucible was used for the growth. The main advantage of the process was that the grown crystal was not in the contact of the crucible wall during annealing and cooling. Scintillation performance of the crystals grown by these two methods were tested and found excellent. Other alkali halide crystals like NaI, NaCl, KBr etc have also been grown successfully employing this technique.

In summary a cost effective Bridgman single crystal growth system has been developed which can be used to grow high quality halide single crystals (NaI, CsI, KBr etc.). By employing this technique the thermal and mechanical shocks to the crystal were avoided that minimized the day light coloration and enhanced the radiation hardness of the grown crystals. The developed technology is ready to be transferred to small-scale industry and has been uploaded on the BARC website [216].

Double tungstate: Single crystals of $NaR(WO_4)_2$ R: Bi and Gd having high density and radiation hardness are the promising materials that can be used as radiation detector for both luminosity and calorimetric measurements (CERN like conditions). The role of oxygen vacancies/interstitial in the luminescence properties of tungstate has been discussed. The present study was aimed at analyzing the intrinsic luminescence characteristics and understand the role of oxygen (during crystal growth as well as annealing in various ambient) in Sheelite type double tungstates. For that purpose, this study was performed on $NaLn(WO_4)_2$ compounds with Ln = Gd, Bi.

(i) $NaBi(WO_4)_2$: Un-doped $NaBi(WO_4)_2$ (NBW) crystals were grown using the Czochralski technique in air ambient. Optical transmission, reflection and luminescence measurements were performed on optically polished single crystal disks. To study the effect of oxygen environment around W, one disc was annealed in air at 700°C for 6 h while the other disc was annealed at 700 °C under high vacuum conditions (10^{-6} mbar) for about 1 h.

As-grown crystal shows an excitation band peak at 322 nm with a shoulder at 280 nm for a broad emission band peaking at 495 nm. In the case of annealed crystal two emission bands peaking at 460 and 510 nm could be well separated for photo excitation at different energies. The excitation band at 280 nm was found to be suppressed significantly in the case of crystal annealed in air. Excitation peak at a higher wavelength (322 nm) can be ascribed to excitons and is independent of annealing while the lower wavelength (higher energy) excitation at 280 nm could be inter-band transitions between O p and W d states. The annealing changes the energy structure of regular WO_4 complex due to defects in anion sublattices including interstitial oxygen and oxygen vacancies which subsequently influence the higher energy excitation as observed in the excitation spectra measured for the annealed samples. The temperature dependence of emission has been studied. In the as-grown crystals the PL intensity becomes half at ~145 K and completely quenched after 200 K. The activation energy for thermal quenching for 495 nm emission was calculated to be about ~160 meV in the case of NBW crystals which is smaller than that of $PbWO_4$ (~200 meV). The observed temperature dependence of PL is also found to be consistent with the reported results for other AWO_4 - type crystals. Thermal quenching profile was also found different for vacuum annealed samples and even at room temperature, the PL could be observed for these samples. Present studies suggest a different thermal quenching of PL due to different growth conditions compared to those reported earlier in the literature for this class of materials. Consequently, the crystals having desired properties can be grown in a controlled ambient that could affect its luminescence characteristics in a desired manner.

The role of the excitons and localization of charge carriers was understood by comparing the spectral dependence of excitation, photoconductivity (PC), transmission, reflectivity and band structure calculation of the as-grown NBW crystal. The dependence of measured reflectivity matches well with that inferred from electronic band structure calculation. Only intrinsic photoconductivity could be observed in these crystals. The photoconductivity observed in the excitation region indicates that excitation leads to free charge carriers. These processes correspond to delocalized transitions unlike localized transitions in the case of PWO. Therefore involvement of mobile charge carriers in the luminescence and excitation processes may be one of the reasons for lesser activation energy of thermal quenching of photoluminescence observed in the NBW crystals as compared to that of PWO crystals. The effect of annealing on PC shows a lower threshold value due to the dissociation of excitons at defects created in the anion sublattice. The appearance of PC below absorption edge may be corresponding to the absorption band of O^- centers. Lower thermal quenching due to the presence of mobile charge carriers and intrinsic photoconductivity only in the excitation region make the NBW crystal a more promising Cherenkov radiator compared to the PWO crystals that are deployed currently in the high energy physics experiments at the CERN.

(ii) $NaGd(WO_4)_2$: Un-doped and Yb^{3+} doped $NaGd(WO_4)_2$ [NGW] single crystals were grown by the Cz technique using an automatic diameter control system (Cyberstar oxypuller) under varying conditions. Phase formation was checked by X-ray powder diffraction pattern and crystals orientation were verified by recording Laue pattern employing Huber make Laue back-reflection camera. The UV-VIS-NIR spectroscopy of the crystal revealed that the UV band edge of the crystal grown in argon ambient shifted towards lower wavelengths compare to crystals grown in air ambient. This may be due to oxygen related defects. Furthermore, the crystals grown in air showed a broad absorption band throughout the crystal bulk and resulted in poor quality of the grown crystals.

The intrinsic luminescence spectra show an excitation peak centered at 260 nm and a broad emission peak at 485 nm. The intrinsic emission from the single crystals grown in air and Ar were compared and it was found that the oxygen related defects played an important role in fluorescence properties of the material. The crystal grown in Ar ambient showed best luminescence properties at room temperature. It was also found that Gd energy levels participatied in the luminescence process that made the luminescence behavior of the NGW different than the other double tungstate.

Finally, as the NGW is a multifunctional material, the polarized NIR absorption spectra of the Yb doped NGW crystal (a laser material) was recorded in 850-1100 nm range. The emission spectra for excitation in 980-990 nm range was found in accordance with the reported values. Though it showed a peak at nearly 1011 nm it is composed of several peaks centered at

935, 965, 975, 994, 1010, 1022 nm. The total broadening of the emission peak is around 60 nm that may make it suitable for the tunable femto-second laser source. Thus it was established that by controlling the oxygen content in the growth ambient the optical and luminescence properties of the NGW could be tailored.

Mn doped CaF_2: CaF_2:Mn also known as TL-400, is an important material for the TL dosimetry. It has a single TL peak around 260°C and is linear for a wide range of doses, from 0.5 mGy to few kGy. The maximum glow-curve intensity is achieved for a doping of 2.5 at.%Mn. It is desirable to use transparent CaF_2:Mn samples to obtain better sensitivity, higher light output and repeatability for dosimetric applications. The difficulty in growing doped single crystals of this material arises from the high vapor pressure of MnF_2 that prohibited its incorporation in the CaF_2 crystal lattice during the growth under vacuum conditions. The difficulty in the growth of single crystals has been circumvented by using optically transparent ceramics (OTC) of this compound in place of single crystal. The OTCs have several advantages over the single crystal like homogeneity, ruggedness, low cost, relatively simple manufacturing process etc.

In this thesis the synthesis of CaF_2 transparent ceramics doped with Mn (2.5 at.%) has been described. These ceramics were found to exhibit properties comparable to the CaF_2 single crystal. CaF_2:Mn (2.5 atm.%) transparent ceramics were prepared by hot pressing of nano-powders. The nano-powder was synthesized by a co-precipitation method. The nano powder and prepared OTC were characterized for the phase identification using a X-ray diffractometer. The microstructure of nano powder and fractured OTC was studied using the SEM and SANS. The transmission in the UV–Vis range (200–1100 nm range) was recorded using a spectrophotometer and in the IR region by FTIR spectroscopy while the photo-luminescence was recorded using a fluorescence spectrometer in the range 200–800 nm. Further the oxidation states of the Mn dopant in the OTC were determined using an X-ray photo-electron spectrometer (XPS) and the concentration was determined using a secondary ion mass spectrometer (SIMS). The dosimetric properties were investigated by irradiating the samples with a ^{60}Co gamma source.

The average grain size, after hot pressing of the nano-powder at 1000°C for 2 h, has been found to be around 100 μm and the hot-pressed pellets showed no voids or porosity. The relative density of the OTC was greater than 99%, as measured using the Archimedes's method. The in-line transmission spectrum recorded for this ceramic in the UV-Vis region exhibited about 50% transmission at 800 nm that decreased at lower wavelengths with a cutoff around 200 nm. The quantitative analysis confirmed the presence of Mn doping in the OTC. Concentration of Mn was found to be in the range of 1-1.5 at.%. It appears that the total amount of Mn added to the solution did not incorporate into the lattice of CaF_2 OTC and evaporates during the high temperature processing.

The excitation and emission spectra of the Mn doped CaF_2 OTC showed the presence of excitation levels corresponding to $^6A_{1g}(^6S) – ^4T_{2g}(^4G)$ transitions of Mn^{2+} that was in agreement with the reported values in literature. In TL studies a single glow-curve at ~ 260°C was obtained. The minimum dose that could be measured was about 3 mGy. The wavelength of the emission spectrum recorded during photoluminescence and thermoluminescence was found to be the same (470 nm). This indicated the observed excitation bands in both the cases were due to internal transitions of Mn^{2+}. The dose linearity of the OTC was measured by irradiating the

OTC to different doses and measuring the area under the glow-peak. The sample was found to be linear up to the highest dose of 100 mGy used in the present work.

In conclusion an alternative of CaF_2:Mn single crystal in the form of optically transparent ceramic has been developed employing hot pressing of nano-crystalline CaF_2:Mn synthesized using a wet chemical processing method. The problem of inhomogeneous distribution of the dopant (Mn) in CaF_2 matrix was solved and it was shown that the CaF_2:Mn (OTC) would be a better material than the conventionally used opaque pellets in TL dosimetry applications. A doping concentration of 1.5 at.% Mn has been successfully achieved in the CaF_2 OTC in spite of sintering at high temperatures under vacuum conditions, as confirmed by XPS and PL measurements. The OTC having Mn^{2+} in the CaF_2 matrix exhibited promising characteristics to be used as a TL dosimeter for applications in the personal and environmental safety.

In this thesis three different kinds of approaches covering a broad field of material synthesis and single crystal growth employing different techniques were investigated. The effect of growth process on crystal growth and scintillation properties of Tl doped CsI has been established. Crystals were grown employing two methods, namely gradient freeze technique and the modified Bridgman technique. The grown crystals were subjected to different heat treatments to improve their scintillation properties. The technology to grow high quality, large size (55 mm diameter x 75 mm Length) alkali halide crystals, developed during the course of this work is available for transfer to industry. In oxide materials sodium double tungstate crystals were taken for the study. The single crystals were grown by the Czochralski technique under varying ambient conditions. The post-growth heat treatment under various ambient was successfully used to tailor the fluorescence and optical properties of the grown crystals. It was found that oxygen has a high mobility at elevated temperatures in the double tungstates that makes them sensitive to ambient conditions during the growth. A process to fabricate OTC of CaF_2:Mn was developed during the course of this work . It was demonstrated that the synthesis of CaF_2:Mn OTC at lower temperatures and under a reducing ambient facilitates the incorporation of Mn in relatively higher amounts and minimizes the oxygen contamination, thus improving the TL-properties significantly.

Future scope:

- The crystal growth system developed will be upgraded to grow alkali halide crystals up to 75 mm diameter and 80-85 mm length and to grow new scintillator materials like $LaBr_3$:Ce, SrI_2:Eu, etc.

- Further studies will be carried out to probe and direct observation of the defects related to oxygen for better understanding of these defects employing various experimental techniques viz. Positron annihilation, EXAFS, ESR, ENDOR, etc. The effect of oxygen defects on lasing characteristic of Yb doped NGW will be studied.
- Further studies will be performed on the optimization of doping concentration of Mn in CaF_2 along with other co-dopants to improve the sensitivity and dynamic response range of the material.

REFERENCES

1. Mitsuru Ishii, Masaaki Kobayashi, Prog. Crystal Growth and Charact. **23** (1992) 245.
2. C.W.E. van Eijk, Phys. Med. Biol., **47** (2002) R85.
3. Hans J. Scheel, J. Crystal Growth, **211** (2000) 1.
4. "Modern Aspects of Bulk Crystal and Thin Film Preparation; ISBN 978-953-307-610-2", Edited by Dr. Nikolai Kolesnikov, In Tech.
5. Guojian Wanga, Yongchen Sun , Gang Yang, Wenchang Xiang , Yutong Guan, Dongming Mei , Christina Keller, Yuen-DatChan, J. Crystal Growth, **352** (2012) 27.
6. Martin Nikl, Meas. Sci. Technol., **17** (2006) R37.
7. "Radiation detection and measurement; ISBN:978-81-265-2260-6 ", G. F. Knoll, John Wiely & Sons.
8. http://www.e-radiography.net/history/general.html
9. W. C. Rontgen, Science, **3** (1896) 227.
10. S.C. Curran, W.C. Baker, U.S. Atomic Energy Commission Report MDDC, **1296** (1944).
11. S.C. Curran, W.C. Baker, Rev. Sci. Instr., **19** (1948) 116.
12. Robert Hofstadte, Phys. Rev., **74** (1948) 100.
13. Carel W. E. van Eijk, Phys. Med. Biol., **47** (2002) R85.
14. L.L. Nagornaya, V.D. Ryzhikov, I.A. Tupitsina, M.A. Krisyuk, S.G. Nedelko, IEEE Trans. Nucl. Sci., **42** (1995) 337.
15. C.L. Melcher, J.S. Schweitzer, IEEE Trans. Nucl. Sci., **39** (1992) 502.

16. C.L. Melcher, Nucl. Instr. Meth. A, **537** (2005) 6.
17. A. Pavel Cherenkov, Doklady Akademii Nauk SSSR, **2** (1934) 451 [Reprinted in Selected Papers of Soviet Physicists, Usp. Fiz. Nauk 93 (1967) 385].
18. K. Ackerstaff et al, Nucl. Instr. Meth. A, **417** (1998) 230.
19. G.I. Britivich, I.I. Bushinskaya, M. Kobayashi, and V.A. Kozlov, Nucl. Instr. and Meth. A, **321**(1992) 64.
20. V.A. Nefedov, "Cherenkov detector", USSR Patent No.1817932 (1991).
21. Chiyan Luo, Mihai Ibanescu, Steven G. Johnson, and J. D. Joannopoulos, Science, **299** (2003) 368.
22. S. Iwata, Calorimeters for high energy experiments at accelerators, Nagoya University Report DPNU-3-79, (1979).
23. J. E Geusic, H. M. Marcos, L. G. Van Uitert Appl. Phys. Lett., **4** (1964) 182.
24. S. Chénais, F. Druon, F. Balembois, P. Georges, A. Brenier, G. Boulon, Optical Materials, **22** (2003) 99.
25. O. Guillot-Noel, B. Bellamy, B. Viana, and D. Gour , Phys. Rev. B, **60** (1999) 1668.
26. A. Bensalah, Y. Guyot, M. Ito, A. Brenier, H. Sato, T. Fukuda, G. Boulon, Optical Materials, **26** (2004) 375.
27. L. G. Van Uitert, J. Electrochem. Sot., **114** (1967) 1048.
28. G. E. Peterson, P. M. Bfudenbaijgh, Appl. Phys. Lett., **4** (1964) 173.
29. D. A. Pinnow, R. W. Dixon, Appl. Phys. Letters, **13** (1968) 157.
30. D. A. Pinnow, L. G. Van Uitert, A. W. Warner, and W. A. Bonner, Appl. Phys. Letters, **15** (1968) 83.
31. www.globalopticsuk.com.

32. D. Vivien, M. Mortier, Ann. Chim. Sci. Mat. **28** (2003) 21.
33. T. Taira, C.R. Phys. **8** (2007) 138.
34. S.F. Wang, J. Zhang, D.W. Luo, F. Gu, D.Y. Tang, Z.L. Dong, G.E.B. Tan, W.X. Que, T.S. Zhang, S. Li, L.B. Kong, Progress in Solid State Chemistry, **41** (2013) 20.
35. R. Hofstadter, Nucleonics, **6** (1950) 70.
36. E. Fioretto et al, , Nucl. Instr. Meth. A, **471** (2001) 234.
37. Chris Bebek, , Nucl. Instr. Meth. A, **265** (1988) 258.
38. G. David, A. Hershcovitch, S. Stoll, C. Woody, P. Braun-Munzinger, R. Hutter, J. Stachel, C.-M. Zou, N. Horwitz, Z. Sobolewski, , Nucl. Instr. Meth. A, **348** (1994) 87.
39. Han Soo Kim, Jang Ho Ha, Se Hwan Parka, Seung Yeon Cho, Yong Kyun Kim, Applied Radiation and Isotopes, **67** (2009) 1463.
40. J. Menefee, Y. Cho, C. Swinhart, IEE Trans. Nucl. Sci. **14** (1967) 464.
41. A. Syntfeld-Każuch, P. Sibczyński, M. Moszyński, A.V. Gektin, W. Czarnacki, M. Grodzicka, J. Iwanowska, M. Szawłowski, T. Szczęśniak, Ł. Świderski, Radiation Measurements, **45** (2010) 377.
42. Olive Lee Hsu, Clayton W. Bates Jr., J. Luminescence, **11** (1975) 65.
43. B.G. Zaslavsky, S.I. Vasetsky, A.M. Kudin, V.Yu. Gres, L.N. Shpilinskaya, T.A. Charkina, L.V. Kovaleva, A.I. Mitichkin, A.N. Boyarintsev, S.Yu. Sumaroko, J. Crystal Growth, **222** (2001) 751.
44. L.G. Eidelman, V.I. Goriletsky, V.G. Protsenko, A.V. Radkevich, V.V. Trofime, J. Crystal Growth, **128** (1993) 1059.
45. O.H. Nestor, Proc. Res. Soc. Symp. Proc. Nuclear radiation detector material, **16** (1983) 77.

46. B.C. Grabmaier, IEEE Trans. Nucl. Sci., **NS-31** (1984) 372.

47. S. Sakuragi, N. Sakai, H Katani, T Miyata, ICALEO **44** (1984) 291.

48. Masaaki Kobayashi, Shiro Sakuragi, Nucl. Instr. Meth. A, **254** (1987) 275.

49. L. Trefilova, B. Grinyov, V. Alekseev, I. Golub, V. Yakovlev, A. Meles, Radiation Measurements, **42** (2007) 839.

50. V Babin, A Krasnikov, H Wieczorek, S Zazubovic, , Nucl. Instr. Meth. A, **486** (2002) 486.

51. C. Palache, H. Berman, and C. Frondel, Dana's system of mineralogy, John Wiley and Sons Inc., New York, 7th ed, v. II (1951) 1074.

52. P. Lecoq, , Nucl. Instr. Meth. A, **537** (2005) 15.

53. A.A. Annenkov, M.V. Korzhik, P. Lecoq, , Nucl. Instr. Meth. A, **490** (2002) 30.

54. C.Yu. Amosov et al, Nucl. Instr. Meth. A, **350** (1994) 204.

55. Gagik G. Demirkhanyan, Vahan G. Babajanyan, Edvard P. Kokanyan, Radik B. Kostanyan, John B. Gruber, Dhiraj K. Sardar, Optical Materials, **29** (2007) 1107.

56. C. Cascales, M. D. Serrano, F. Esteban-Betegón, C. Zaldo, R. Peters, K. Petermann, G. Huber, L. Ackermann, D. Rytz, C. Dupré, M. Rico, J. Liu, U. Griebner, and V. Petro,v Phys. Rev. B, **74** (2006) 174114.

57. R.M. Hazen, L.W. Finger, and J.W.E. Mariathasan, J. Phys. Chem. Solids, **46** (1985) 253.

58. C.A. Kodaira, H.F. Brito, M.C.F.C. Felinto, J. Solid State Chem., **171** (2003) 401.

59. Glorieux Benoît, Jubera Véronique, Apheceixborde Arnaud, Garcia Alain, Solid State Sciences, **13** (2011) 460.

60. S. Zerfoss, L. R. Johnson, and O. Imber, Phys. Rev., **75** (1949) 320.

61. A.B. Campos, A.Z. Simoes, E. Longo, J.A. Varela, V.M. Longo, A.T. Figuerido, F.S. De Vicente, A.C. Hernandes, Appl. Phys. Lett., **91** (2007) 051923.
62. Tae Hoon Kim, Shinuk Cho, Kwanghee Lee, Min Su Jang, and Ji Hyun Ro, Appl. Phys. Lett., **81** (2002) 3756.
63. Tingyu Liu, Jianqi Shen, Qiren Zhang, Songlin Zhuang, J. Luminescence, **126** (2007) 239.
64. Wenliang Zhu, Xiqi Feng, Zhonghua Wu, Zhenyong Man, Physica B, **324** (2002) 53.
65. H. Becquerel, C.R. Acd. Sci (Paris), **129** (1899) 912.
66. H. Becquerel, C.R. Acd. Sci (Paris), **144** (1899) 691.
67. E. Iwase, Sci. Paper of the Institute of Phys. & Chem. Res., **22** (461), **23**(486) (1934).
68. J.H. Schulman, F.H. Attix, E.J. West, R.J. Ginther, Rev. Sci. Instr., **31** (1960) 1263.
69. W. Binder, W.S. Disterhoft, J.R. Cameron, Proc. Second. Int. Conf. Luminescence Dosimetry, USAEC Technical Inf. Rep. Conf- 680920 (1968) 43.
70. B. Marczewskaa, P. Bilski, M. Budzanowski, P. Olko, V. Chernov, Radiation Measurements, **33** (2001) 571.
71. Su Liangbi, Yongjun Dong, Weiqiao Yang, Tao Sun, Qingxue Wang, Xu Jun, Guangjun Zhao, Mater. Res. Bull., **40** (2005) 619.
72. S.M. Kaczmarek, G. Leniec, G. Boulon, J. Alloys Compounds, **451** (2008) 116.
73. W. Beck, D. Ricard, C. Flytzanis, Appl. Phys. Lett., **69** (1996) 3197.
74. I. Holl, E. Lorentz, G. Mageras, IEEE Trans. Nucl. Sci., **NS-35** (1988) 105.
75. V. Emir Kafadar, A. Necmeddin Yazici, R. Güler Yildirim, Nucl. Instr. Meth. B, **267** (2009) 3337.
76. C. M. Sunta, Radiation Protection Dosimetry, **8** (1984) 25.

77. M. Danilkin, A. Lust, A. Ratas, V. Seeman, M. Kerikmäe , Radiation Measurements, **43** (2008) 300.
78. A. K. Bakshi, B. Dhabekar, N. S. Rawat, S. G. Singh, V. J. Joshi, V. Kumar, Nucl. Instr. Meth. B, **267** (2009) 548.
79. T.J. Gray, D.P. Detwiller, D.E.Rase, W.G.Lawrence, R.R.West, T.J. Jennings, "The Defect Solid State", Inter Science Publications Inc., New York, (1957).
80. Samuel Blahuta, Aurélie Bessière , Bruno Viana , Vladimir Ouspenski , Eric Mattmann , Julien Lejay and Didier Gourier, Materials, **4** (2011), 1224.
81. Akira Suzuki, Shunsuke Kurosawa, Jan Pejchal, Vladimir Babin3, Yutaka Fujimoto, Akihiro Yamaji, Mafuyu Seki,Yoshisuke Futami, Yuui Yokota, Phys. Status Solidi C, **9** (2012) 2251.
82. P. Dorenbos, M.V. Korshik, A. P. Kudryatseva, S.V. Lyubetskii, B. I. Minkov, V. B. Pavlenka, A. A. Fyodrov, J. Applied Spectroscopy, **59** (1993) 633.
83. Sangeeta, D. G. Desai, A. K. Singh, M. Tyagi, S. C. Sabharwal, J. Crystal Growth, **296** (2006) 81.
84. S. Toschev, "Crystal Growth: An Introduction", ed. P. Hartman, North Holland, Amsterdam, (1973).
85. J.W. Gibbs, Trans Connect Acad Sci, **3** (1876) 108-248.
86. J.W. Gibbs, Trans Connect Acad Sci, **16** (1878) 343-524.
87. J.C. Brice, "Crystal Growth Processes", Blackie, Glasgow and London (1986).
88. K. Nassau, J. Crystal Growth, **5** (1969) 338.
89. K. Nassau, J. Nassau, J. Lapidary, J. Crystal Growth **24** (1971) 1284.
90. J. Czochralski, Z. Phys. Chem., **92** (1918) 219.

91. F.R. Charvet, “Growth of Crystals”, Vol. 12, ed. A.A. Chernov, (1984) 210.
92. V.L. Indenbom, I.S. Zhitomirskii, T.S. Chebanova, “Growth of Crystals”, Ed. N.N. Sheftel, Consultant Bureau, New York (1969) 249.
93. P.W. Bridgman, Proc. Amer. Acad. Arts Sci., **60** (1925) 303.
94. K. Hamano, S. Kanzaki, J. Ceramic Society Japan, **85** (1977) 225.
95. T.C. Lu, X.H. Chang, J.Q. Qi, X.J. Luo, Q.M. Wei, S. Zhu, Low-temperature, Appl. Phys. Lett., **88** (2006) 213120.
96. Y.T. Zou, D.W. He, X.K. Wei, R.C. Yu, T.C. Lu, X.H. Chang et al. Materials Chemistry and Physics, **123** (2010) 529.
97. S.R. Podowitz, R. Gaume, R.S. Feigelson, J. American Ceramic Society, **93** (2010) 82.
98. W.H. Bragg, Nature, **77** (1908) 270.
99. H.P. Clug, L.E. Alexander, “X-ray Diffraction Procedures for Polycrystalline and Amorphous Materials” John-Willey, London, (1954).
100. C. Marin, E. Dieguez “Orientation of Single Crystals by Back Reflection Laue Pattern Simulation” World Scientific Publishing Company, Singapore, (1999).
101. J.J.D. Winefordner, S.G. Schulman, T.C. O'haver, "Luminescence Spectrometry in Analytical Chemistry", Wiley-Interscience, New York, (1972).
102. http://www.edinst.com/fl920p.htm.
103. Faiz M. Khan, "The Physics of Radiation Therapy", Lippincott Williams &Wilkins, (2003).
104. M. Nikl, V. V. Laguta, and A. Vedda, Phys. Stat. Sol. B, **245** (2008) 1701.
105. H. M. Rietveld, Acta Cryst., **22** (1967) 151.
106. H. M. Rietveld, J. Appl. Cryst., **2** (1969) 65.

107. G. Caglioti, A. Paoletti, F. P. Ricci, Nucl. Instrum., **3** (1958) 22.

108. A.C. Larson and R.B. Von Dreele, "General Structure Analysis System (GSAS)", Los Alamos National Laboratory Report LAUR, **86** (1994) 748.

109. B. H. Toby, J. Appl. Cryst., **34** (2001) 210.

110. R.M. Dreizler and E.K.U. Gross. Density Functional Theory. Springer, Berlin, 1990.

111. Eschrig, The Fundamentals of Density Functional Theory. Teubner, Stuttgart, 1996.

112. R.G. Parr and W. Yang. Density-Functional Theory of Atoms and Molecules. Oxford University Press, New York, 1989.

113. P. Hohenberg, W. Kohn., Phys. Rev., **136** (1964) B864.

114. W. Kohn, L.S. Sham, Phys. Rev. A, **140** (1965) 1133.

115. R.O. Jones and O. Gunnarson., Rev. Mod. Phys., **61** (1989) 689.

116. John P. Perdew, J. A. Chevary, S. H. Vosko, K. A. Jackson, M. R. Pederson, D. J. Singh, C. Fiolhais, Phys. Rev. B, **46** (1992) 6671.

117. John P. Perdew, K. Burke, M. Ernzerhof, Phys. Rev. Lett., **78** (1997) 1396.

118. D. J. Singh, “Plane Waves, Peudopotential and the LAPW Method”, Kluwer Academic Publisher, Boston, Dortrecht, London, (1994).

119. P. Blaha, K. Schwarz, P.Sorantin, S.B. Trickey, Comput. Phys. Commun., **59** (1990) 399.

120. D. D. Koelling, B. N. Harmon, J. Phys. C, **10** (1977) 3107.

121. A.H. MacDonald, W.E. Picket, D.D. Koelling, J. Phys. C, **13** (1980) 2675.

122. P. Novak (1997), WIENROOT/SRC/novak_lecture_on_spinorbit.ps.

123. J. P. Desclaux, Comput. Phys. Commun., **1** (1970) 216.

124. J.C. Slater, Phys. Rev., **51** (1937) 151.

125. K. Schwarz , P. Blaha, G.K.H. Madsen, Comput. Phys. Commun., **147** (2002) 71.

126. P. Blaha, K. Schwarz, WIEN2k, Vienna University of Technology, Austria, (2002).

127. Andris Gulans et al, J. Phys.: Condes matter, **26** (2014) 363202.

128. W. Van Sciver, R. Hofstadter, Phys. Rev. **84** (1951) 1062.

129. S. Suryanarayanana, A. Karellasa, S. Vedantham, Nucl. Instrum. Meth. A, **533** (2004) 560-570.

130. E. Fioretto, F. Innocenti, G. Viesti, M. Cinausero, L. Zuin, D. Fabris, M. Lunardon, G. Nebbia, G. Prete, Nucl. Inst. Meth. A, **442** (2000) 412.

131. J. Chavanelle, M. Parmentier, Nucl. Inst. Meth. A **504**, (2003) 321.

132. A. Wagner et al, Nucl. Inst. Meth. A, **456** (2001) 290.

133. Weerapong Chewpraditkul, Lukasz Swiderski, Marek Moszynski, NUKLEONIKA, 53 (2008) 51.

134. Maria da Conceição Costa Pereira, Tufic Madi Filho, Materials Sciences and Applications, **5** (2014) 368.

135. Yuntao Wu, Guohao Ren, Martin Nikl, Xiaofeng Chen, Dongzhou Ding, Huanyin Li, Shangke Pana, Fan Yangc, CrystEngComm, **16** (2014) 3312.

136. C. Brecher, A. Lempicki, S.R. Miller, J. Glodo, E.E. Ovechkina, V. Gaysinskiy, V.V. Nagarkar, R.H. Bartram, Nucl. Inst. Meth. A, **558** (2006) 450.

137. R.H. Bartram, L.A. Kappers, D. S. Hamilton, A. Lempicki, C. Brecher, J. Glodo, V. Gaysinskiy, E.E. Ovechkina, Nucl. Inst. Meth. A, **558** (2006) 458.

138. H. Grassmann, E. Lorenz, H.-G. Moser, Nucl. Inst. Meth. A, **228** (1985) 323.

139. E. Blucher, B. Gettelman, B.K. Kowalewski, J. Kandaswamy, Y. Kubota, N. Mistry, S. Stone, A. Bean, , Nucl. Inst. Meth. A, **249** (1986) 201.

140. B.G. Zaslavsky, J. Crystal Growth, **200** (1999) 476.

141. V.I. Goriletsky, L.G. Eidelman, V.A. Nemenov, V.G. Protsenko, A.V. Radkevich, J. Crystal Growth, **52** (1981) 509.

142. C.L. Woody, J.A. Kierstead, P.W. Levy, S. Stoll, IEEE Trans. Nucl. Sci., **39** (1992) 524.

143. V.V. Avdeichikov, L. Bergholt, M. Guttormsen, J.E. Taylor, L. Westerberg, B. Jakobsson, W. Klamra, Yu.A. Murin, Nucl. Inst. Meth. A, **349** (1994) 216.

144. A.K. Sinha, Archna Sagdeo, Pooja Gupta, Ashok Kumar, M. N. Singh, R. K. Gupta, S. R. Kane, S. K. Deb, Proceedings of The 55^{Th} DAE Solid State Physics Symposium 2010 AIP Proceedings, **CP1349** (2011) 503.

145. N. Balamurugan, A. Arulchakkaravarthib, S. Selvakumarc, M. Lenina, Rakesh Kumard, S. Muralithard, K. Sivajic, P. Ramasamya, J. crystal growth, **286** (2006) 294.

146. M.A.H. Chowdhury, D.C. Imrie, Nucl. Inst. Meth. A, **432** (1999) 138.

147. V. Yakovlev, A. Meleshko, L. Trefilova, J. Luminescence, **128** (2008) 1447.

148. S.G. Singh, M. Tyagi, D.G. Desai, A.K. Chauhan, S.C. Gadkari, International Conference on Emerging Functional Material (PEFM) AIP Proceedings., **CP1313** (2010) 337.

149. Agnieszka Syntfeld-Ka˙zuch, ŁukaszS´ widerski, Wiesław Czarnacki, Michał Gierlik, Włodzimierz Klamra, Marek Moszyn´ski, Paul Schotanus, IEEE Trans. Nucl. Sci., **54** (2007) 1836.

150. D.V. Dementyev et al, Nucl. Instr. Meth. A, **440** (2000) 151.

151. Shinzou Kubota, Shirou Sakuragi, Satoshi Hashimoto, Jian-zhi Ruan, Nucl. Instr. Meth. A, **268** (1988) 275.

152. http://www.crystals.saint-gobain.com /uploadedFiles /SGCrystals /Documents /CsI Pure Data Sheet.pdf

153. C. Celiktas, E. E. Ermis, M. Bayburt, J Radioanal Nucl Chem, **293** (2012) 377.

154. F.De. Notaristefani, P. Lecoq, M.Schneegans, Heavy Scintillators for Scientific and Industrial Applications, Edition Frontiers, France, **361** (1993).

155. B.I. Zadneprovski, V.A. Nefedov, E.V. Polyansky, E.G. Devitsin, V.A. Kozlov S.Y. Potashov, A.R. Terkulov, Nucl. Instr. and Meth. A, **486** (2002) 355.

156. P.V. Klevtsov, V.A. Vinokurov, R.F. Klevtsova, Kristallografiya, **18** (1973) 1192.

157. M. Kobayashi, S.Sugimoto, Y.Usuki, Nucl. Instr. Meth. A, **524** (2004) 385.

158. P. Lecoq, I. Dafinei, E. Auffray, M. Schneegans, M.V. Korzhik, O.V. Missevitch, V.B. Pavlenko, A.A. Fedorov, A.N. Annenkov, V.L. Kostylev, V.D. Ligun, Nucl. Instr. Meth. A, **365** (1995) 291.

159. Qiren Zhang, Tingyu Liu, Jun Chen, Xiqi Feng, Phys. Rev. B, **68** (2003) 064101.

160. V. Volkov, M. Rico, A. Mendez-Blas, C. Zaldo, J. Phys. Chem. Sol., **63** (2002) 95.

161. K. Nitsch, M. Nikl, C. Barta, D. Schultze, A. Trisk, R. Uecker, Phys. Stat. Sol. A, **118** (1990) K133.

162. S.G. Singh, M. Tyagi, A.K. Singh, Sangeeta, Cryst. Res. Technol., **45** (2010)18.

163. Masami Fujita, Minoru Itoh, Hiroyuki Mitani, Sangeeta, Mohit Tyagi, Phys. Stat. Sol. B, **247** (2010) 405.

164. Chihiro Itoh, Satohiro Kigoshi, Phys. Stat. Sol. A, **203** (2006) 3774.

165. M. Anicete-Santos, F.C. Picon, M.T. Escote, E.R. Leite, P.S. Pizani, J.A. Varela, E. Longo, Appl. Phys. Lett., **88** (2006) 211913.

166. Mohit Tyagi, S.G. Singh, Sangeeta, R. Prasad, S. Auluck, D.J. Singh, Physica B, **405** (2010) 3267.

167. S.G. Singh, Mohit Tyagi, A.K. Singh, S.C. Gadkari, Nucl. Instr. Meth. A, **621** (2010) 111.

168. S. Peretsa, M. Tseitlinb, R.Z. Shnecka, D. Mogilyanskic, G. Kimmelc, Z. Burshteina, J. Crystal Growth, **305** (2007) 257.

169. M. Nikl, K. Nitsch, J. Hybler, J. Chval, and P. Reiche, Phys. Status Solidi B, **196** (1996) K7.

170. M. Nikl et al., J. Appl. Phys., **82** (1997) 5758.

171. M. V. Korzhik, V. B. Pavlenko, T. N. Timoschenko, V. A. Katchanov, A. V. Singovskii, A. N. Annenkov, V. A. Ligun, I. M. Solskii, J. P. Peigneux, Phys. Status Solidi A, **154** (1996) 779.

172. Yu.A. Hizhnyi, S.G. Nedilko, J. Luminescence, **102–103** (2003) 688.

173. Y. Zhang, N.A.W. Holzwarth, R.T. Williams, Phys. Rev. **B**, 57 (1998) 12738.

174. R.T. Williams, Y.C. Zhang, Y. Abraham, N.A.W. Holzwarth, Proceedings of the International Conference, SCINT'99, Moscow, Russia, 1999, 118.

175. Y.B. Abraham, N.A.W. Holzwarth, R.T. Williams, G. Eric Matthews, Alan R. Tackett, Phys. Rev. B, **64** (2001) 245109.

176. AK Singh, M Tyagi, SG Singh, DG Desai, S Sen, SC Gadkari, J. Luminescence, **137** (2013) 208.

177. W. van Loo, Phys. Status Solidi A **27** (1979) 565.

178. W. van Loo, Phys. Status Solidi A **28** (1979) 227.

179. G. Tamulaitis, S. Burachas, V.P. Martinov, V.D. Ryzhikov, H.H. Gutbrod, V.I. Manko, and M. Terekhin, Phys. Status Solidi A, **161** (1997) 533.

180. M Tyagi, S.G. Singh, S.Sen, A.K. Singh, S.C.Gadkari, J. Luminescence, **132** (2012) 41.

181. Ikesue, I. Furusato, K. Kamata, J. Am. Ceram. Soc.,**78** (1995) 225.

182. Ikesue, I. Furusato, K. Kamata, K. Yoshida, J. Am. Ceram. Soc.,**78** (1995) 1033.

183. A. Lucca, M. Jacquemet, F. Druon, F. Balembois, P. Georges, Opt. Lett., **29** (2004), 1879.

184. M. Prokic, L. Botter-Jensen, Radiat. Prot. Dosimetry, **47** (1993) 195.

185. R. Kalchgruber, H.Y. Goksu, E. Hochhauser, G.A. Wagner, Radiation Measurements, **35** (2002) 585.

186. Mikhail Danilkin, Aime Lust, Mihkel Kerikmae, Viktor Seeman, Hugo Mandar, Mare Must, Radiation Measurements, **41** (2006) 677.

187. S.G. Singh, A.K. Singh, Shashwati Sen, S.C. Gadkari, AIP Conf. Proc., **1313** (2010) 340.

188. P. Aubry, A. Bensalan, P. Gredin, G. Partriarche, D. Viven, M. Mortier, Optical Materails, **31** (2009) 750.

189. P. Samuel, H. Ishizawa, Y. Ezura, K I Ueda, A Moorthy babu, Optical Materials, **33** (2011) 735.

190. X. Qin, H Yang, G Zhou, D Luo, Y Yang, J Zhang, S Wang, J ma, D Tang, Optical Materials, **34** (2012) 973.

191. Andréas Lyberis, Adam J. Stevenson, Akiko Suganuma, Sandrine Ricaud, FrédéricDruon,FrédéricHerbst, Daniel Vivien, Patrick Gredin, Michel Mortier, Optical Materials, **34** (2012) 965.

192. Andréas Lyberis, Gilles Patriarche, Patrick Gredin, Daniel Vivien, Michel Mortier, J. European Ceramic Society, **31** (2011) 1619.

193. Tarak Kallel, Mohamed Amine Hassairi, Mohamed Dammak, Andreas Lyberis, Patrick Gredin, Michel Mortier, J. Alloys Compounds, **584 (**2014) 261.

194. Liu Zuodong, Meia Bingchu, Song Jinghong, Lia Weiwei, J. European Ceramic Society, **34** (2014) 4389.

195. Jan Šulc, Michal Němec, Helena Jelinková, Maxim E. Doroshenko, Pavel P. Fedorov,Vyacheslav V. Osiko, Proc. SPIE 8959, Solid State Lasers XXIII: Technology and Devices, 895925 (February 28, 2014); doi:10.1117/12.2040763.

196. Gang Lu, Bingchu Mei, Jinghong Song, Weiwei Li, Ruzhen Xing, Materials Letters, **115** (2014) 162.

197. S. Mazumder, D. Sen, T. Sarvanan, P.R. Vijayraghavan, J. Neutron Research, **9** (2001) 39.

198. J.A. Lake, J. Appl. Cryst., **23** (1967) 191.

199. J. Bahadur, D. Sen, S. Mazumder, R. Shukla, A.K. Tyagi, J. Phys.: Condens. Matter, **20** (2008) 345201.

200. I. Groma, G. Monnet, J. Appl. Crys.t, **35** (2002) 589.

201. "Handbook of x-ray photoelectron spectroscopy" by C. D. Wagner, W. M. riggs, L. E. Davis, J. F. Moulder, G. E. Muilenberg, Perkin-Elmer Publication 1979.

202. Hsiang-en Wang, Shan-Wen Lin, Pao-Shan Weng, Pin-Chieh Hsu, Appl. Radiat. Isot., **46** (1995) 869.

203. P.J. Alanso, R. Alcala J. Luminescence, **22** (1981) 321.

204. A.R. Lakshmanan, U. Madhusoodanan, D. Sundar, B.S.K. Nair, Radiation Physics and Chemistry, **51** (1998) 399.

205. J.L. Patel, B.C. Cavenett, J.J. Davies, and W.E. Hagston, Phys. Rev. Lett., **33** (1974) 1300.

206. B. Jassemnejad, R. J. Abbundi, M. D. Brown, S. W. S. McKeever,Phys. Status Solidi A, **108** (1988) 753.

207. D.L. Fehl, D.I. Muron, B.R. Suijka, D.W. Vehar, L.I. Lorence, R.L. Westfall, S.C. Jones, I.A. Sweet, Rev. Sci. Instrum., **65** (1994) 3243.

208. S.G. Singh, Sen Shashwati, G.D. Patra, S. Bhattacharya, A.K. Singh, S. Shinde, S.C. Gadkari, Nucl. Instr. Meth. B, **287 (**2012) 51.

209. Shashwati Sen, S.G. Singh, G.D. Patra, S. Shinde, S. Bhattacharya, S.C. Gadkari, AIP Conf. Proc.,**1447** (2012) 279.

210. Shashwati Sen, Garima Mittal, S.K. Deshpande, S.C. Gadkari, AIP Conf. Proc., **1512 (**2013) 936.

211. ManoranjanGhosh, ShashwatiSen, S.S. Pitale, U.K. Goutam, S. Shinde, G.D. Patra, S.C. Gadkari, AIP Conf Proc., **1591** (2014) 592.

212. K. Chakrabarti, V.K. Mathur, R.J. Abbundia, N. Kristianpollerh, W.F. Hornyak, J. Luminescence, **48** (1991) 828.

213. S.W.S. McKeever, B. Jassemenejad, J.F. Landreth, J. Appl. Phys., **60** (1986) 1124.

214. K. Chakrabarti, K. Sharma, V.K. Mathur, J.H. Barkyoumb, Phys. Rev. B, **51** (1995) 16541.

215. R. Alcala, P.J. Alonso, Journal of Luminescence**, 20** (1979) 1.

216. http://barc.gov.in/technologies/csiti/csiti.html